ENTHAPLY EFFECTS ON HYPERVELOCITY BOUNDARY LAYERS

Thesis by

Philippe H. Adam

In Partial Fulfillment of the Requirements

for the Degree of

Doctor of Philosophy

California Institute of Technology

Pasadena, California

1997

(Submitted May 23, 1997)

Acknowledgements

I would like to express my deepest gratitude to my advisor, Prof. Hans G. Hornung, for allowing me to work on this project under his guidance.

Any experiment in T5 is a team effort and none of the work presented here would have been possible without the help of the many people I was fortunate to meet and work with during my stay at GALCIT. I am especially grateful to Eric Cummings, Jean-Paul Davis, Patrick Germain, Patrick Lemieux and Bernard Rousset. Special thanks also go to Bahram Valiferdowsi for all of his help in and out of the lab.

I would like to acknowledge my committee chairman Prof. Brad Sturtevant as well as Profs. Tim Colonius, Andy Ingersoll and Joe Shepherd for taking the time to read through this thesis.

I would also like to acknowledge the support I received from the Richard D. and Ann Delauer Fellowship and Russell R. Vought Fellowship during my first year of graduate studies at the Institute.

This work was supported by the AFOSR URI grant F49620-93-1-0338 (Dr. J. Tishkoff).

Abstract

More than 50 shots with air and 35 shots with carbon dioxide were carried out in the T5 shock tunnel at GALCIT to study enthalpy effects on hypervelocity boundary layers. The model tested was a 5° half-angle cone measuring approximately 1 meter in length. It was instrumented with 51 chromel-constantan coaxial thermocouples and the surface heat transfer rate was computed to deduce the state of the boundary layer and, when applicable, the transition location.

Transitional boundary layers obtained confirm the stabilizing effect of enthalpy. As the reservoir enthalpy is increased, the transition Reynolds number evaluated at the reference conditions increases as well. The stabilizing effect is more rapid in gases with lower dissociation energy and it seems to level off when no further dissociation can be achieved. These effects do not appear when the transition location is normalized with the edge conditions. Further normalizing the reservoir enthalpy with the edge enthalpy appears to collapse the data for all gases onto a single curve. A similar collapse is obtained when normalizing both the transition location and the reservoir enthalpy with maximum temperature conditions obtained with BLIMPK, a nonequilibrium boundary layer code.

The observation that the reference conditions seem more appropriate to normalize high enthalpy transition data was taken a step further by comparing the tunnel data with results from a reentry experiment. When the edge conditions are used, the tunnel data are around an order of magnitude below the flight data. This is commonly attributed to the fact that disturbance levels in tunnels are high, causing the boundary layer to transition prematurely. However, when the conditions at the reference temperature are used instead, the data come within striking distance of one another although the trend with enthalpy seems to be a destabilizing one for the flight data. This difference could be due to the cone bending and blunting observed during the reentry.

Experimental laminar heat transfer levels were compared to numerical results obtained with BLIMPK. Results for air indicate that the reactions are probably in nonequilibrium and that the wall is catalytic. The catalycity is seen to yield higher surface heat transfer rates than the noncatalytic and frozen chemistry models. The results for carbon dioxide, however, are inconclusive. This is, perhaps, because of inadequate modeling of the actual reactions. Experimentally, an anomalous yet repeatable, rise in the laminar heat transfer level can be seen at medium enthalpies in carbon dioxide boundary layers.

Contents

List of Figures

Chapter 1 Introduction

No better way comes to mind to introduce the subject of hypervelocity flows and boundary layer transition than to borrow the following quote from the opening of a recent Smithsonian Air & Space article (Heppenheimer [1989]):

> *"The difficulties the Air Force has encountered over the past three years in identifying an Aerospaceplane program have sprung from the facts that the requirement for a fully recoverable space launcher is at present only vaguely established, that today's state of the art is inadequate to support any real hardware development, and the cost of any such undertaking will be extremely large."*

The year was 1963 and the Air Force Scientific Advisory Board had just put the brakes on the entire American hypersonics program spearheaded by Antonio Ferri at GASL/Marquardt, Alexander Kartveli at Republic Aviation, and many others. The problem was quite simple: while there were no shortages of design ideas, the Aerospaceplane being but one example, the lack of money as well as technological barriers had hindered the development of suitable ground testing facilities to verify these concepts (Ferri [1964]).

The next 20 years would be difficult ones for hypersonics but nevertheless, advancements prevailed, facilities capable of simulating sub-orbital to orbital flows were developed, and computers evolved to the point where simulations could be routinely included into the design process. Persistence by the "old guard" of scramjets and by some newer recruits such as Tony duPont led to a revived effort and the $3.3 billion National Aerospace Plane program in 1985. However, the NASP program was equally short lived. This time, in 1992 and despite the significant progress that had been needed in ground testing, the Defense Science Board (DSB [1992], Kandebo[1993]) concluded that

> *"... insufficient technological progress had been made by the X-30 program to warrant a demonstrator's construction. Specifically, the board found that boundary layer transition on a NASP vehicle could not be determined with sufficient accuracy."*

Indeed, if one cannot predict where in a vehicle flight trajectory the heat flux will transition from its low laminar levels to its much more severe turbulent level, how can an effective thermal protection system be designed or drag be predicted?

A few words are therefore in order to describe exactly where hypervelocity flows occur and how they are simulated in ground testing facilities. Also in order is a quick look at where we stand in terms of understanding boundary layers under these conditions. In particular, one would like to know what has been learned and what can still be learned in terms of stability and transition.

1.1 Hypervelocity flow simulation

Typical trajectories for cruise, ascent, reentry and aeroassisted orbital transfer vehicles are illustrated in Figure 1.1 below.

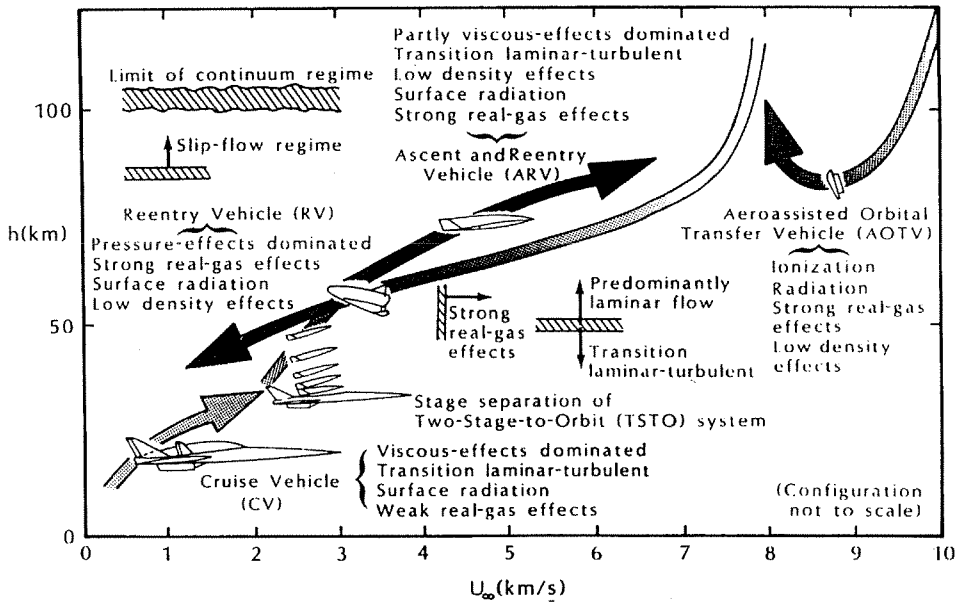

Figure 1.1: Hypersonic vehicles and aerothermodynamic effects (Bertin [1994])

Up to about 2 km/s, perfect gas assumptions are valid, i.e., the stagnation temperature on the points of the vehicle where the flow is brought to rest is not high enough to cause any significant amount of gas to dissociate. It is therefore possible to express any dimensionless quantity Q pertaining to the flow in the following form (Hornung [1988,1996]):

$$Q = Q(M, Re, Pr, \gamma, \frac{T_w}{T_0}, \alpha, \beta, Bg, Fq) \tag{1.1}$$

where the non-dimensional parameters within the parentheses are defined in the next few paragraphs. Reproducing all of these parameters, when testing a model in a wind tunnel, ensures that Q is the same as in free flight. It is reasonable to assume that one can accurately position the model so that its angle of attack α, and its angle of yaw β, do not present a problem. Scaling down the flight

model body geometry Bg, to a reasonable size for wind tunnel testing, is also feasible without much difficulty. Finally, using the same test gas in the tunnel as in flight, i.e., duplicating the ratio of specific heats γ and the Prandtl number Pr, then reduces Equation (1.1) to

$$Q = Q(M, Re, \frac{T_w}{T_0}, Fq) \tag{1.2}$$

and the simulation problem to an exercise in reproducing four parameters: the Mach number M, the Reynolds number Re, the wall to stagnation temperature ratio T_w/T_0 and the flow quality Fq. Setting aside the issue of flow quality, it is interesting to note that velocity does not appear directly. Furthermore, it is not the stagnation temperature that matters but the ratio with wall temperature. One could therefore freely lower the temperature, thereby lowering the sound speed and increasing the Mach number. In reality, however, high Mach numbers stem from high speeds rather than from low temperatures. This is unfortunate since, in practice, it is simpler to generate a "cold" hypersonic flow than a "hot" one.

Speed must be duplicated to bring out not only the appropriate physical phenomena in the flow but also the appropriate chemical ones. This brings us to the issue of real-gas effects which occur when the speed exceeds a few km/s as illustrated again in Figure 1.1. These flows are referred to as hypervelocity flows as opposed to simply hypersonic. The associated temperatures, immediately behind a shock wave or at a stagnation point for example, can be so high as to cause dissociation and recombination reactions to occur. Indeed, if the kinetic energy of the gas, $U^2/2$, is comparable to the characteristic dissociation energy of the species making up the gas, $\mathcal{D}$, the composition of the gas and the properties of the flow will change. Further accounting for the fact that reactions take a finite time, and hence a finite length $l_{\mathcal{D}}$, the same nondimensional Q described by Equation (1.2) for the perfect gas case now becomes

$$Q = Q(\frac{U^2}{2\mathcal{D}}, \frac{l_{\mathcal{D}}}{L}, \frac{T_w}{T_0}, \alpha_\infty, Fq) \tag{1.3}$$

where L is a characteristic length and α_∞ refers to the level of freestream dissociation. It is assumed again that accurately reproducing the body geometry is possible and that the model can be properly oriented in the wind tunnel.

Duplicating $l_{\mathcal{D}}/L$ is achieved by duplicating the product ρL which in turn guarantees that the Reynolds number is automatically the same. Hence, Re is omitted from the list of parameters between the parentheses in Equation (1.3). It is also interesting to note that for hypervelocity flows, the Mach number (if sufficiently large) is not important but rather the enthalpy which is related to the speed and appears as the ratio $U^2/2\mathcal{D}$. The more difficult of the parameters to reproduce are

the freestream dissociation level and the flow quality. These difficulties result directly from the way these flows are produced in the laboratory.

Generating "cold" hypersonic flows in a wind tunnel is relatively simple to do. The only temperature limit of concern is the condensation limit of the fluid itself since it cools down as it is accelerated from its reservoir chamber through a nozzle to the desired Mach number over the test model. However, to obtain a flow of several km/s, one must start with a very high temperature and pressure reservoir to overcome the effects of the nozzle expansion and end up with the proper conditions in the freestream. While the Mach number at the exit may still be moderately high, it is a consequence of the high velocity, the temperature being actually quite high as well. In fact, to obtain a typical flow around 5 km/s requires a reservoir on the order of 10,000 K and 60 MPa. It is obvious that no materials would be able to sustain these conditions for an extended period of time. Hypervelocity facilities are therefore short duration facilities and test times typically run from a few hundred microseconds to a few milliseconds.

The second issue that comes to mind is then the freestream dissociation level and composition. Because of the conditions in the reservoir, the gas starts out in chemical equilibrium: highly, if not fully, dissociated and perhaps even partially ionized. Typically for air, molecular oxygen first breaks down to atomic oxygen (enthalpy of reaction $\approx$ 15.6 MJ/kg for $O_2 \rightarrow 2\ O$) and if the reservoir enthalpy is sufficiently high, molecular nitrogen may dissociate as well (enthalpy of reaction $\approx$ 33.7 MJ/kg for $N_2 \rightarrow 2\ N$). This leads to further reactions producing nitrogen dioxide and nitrogen monoxide. Some of the major chemical reactions in air are illustrated in Figure 1.2 below. As the gas is accelerated and expanded through the nozzle, recombination occurs and some of the original molecules are recovered from their atomic elements. Ideally, complete recombination is desired to reproduce the composition of the gas in the freestream of the real flight environment. Unfortunately, the gas composition freezes too early in the nozzle and freestreams produced by hypervelocity ground testing facilities are for the most part still partially dissociated. Moderate gains may be achieved by relying on an unsteady expansion where the gas is already in motion and possesses some kinetic energy as opposed to a steady expansion from a stagnant reservoir where the gas is initially at rest (Hornung and Bélanger [1990]).

Flow quality problems such as freestream noise, test time limitations and particulate contamination also arise in hypervelocity facilities and severely constrain the types of experiments that can be run at these conditions. This is mostly due to the short duration nature of the tests and to the techniques used to obtain the high-temperature, high-pressure reservoir desired for subsequent expansion. Indeed, the most common and probably the most efficient way of impulsively

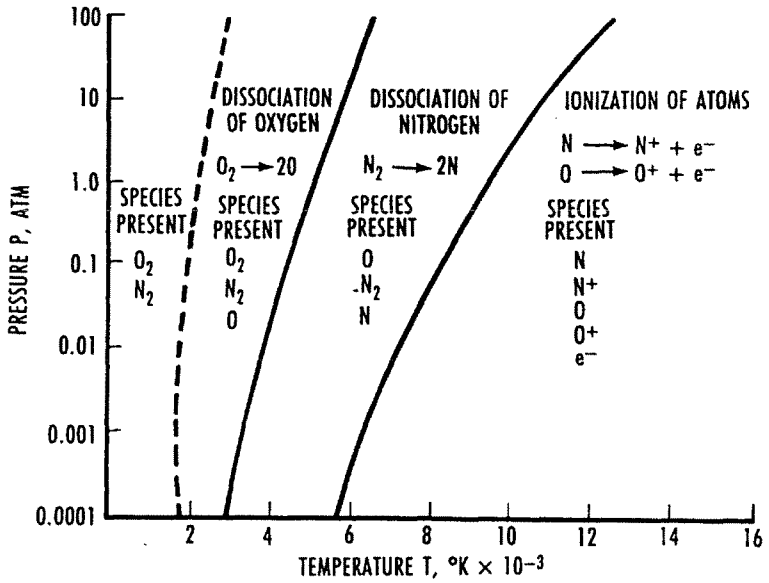

Figure 1.2: Major chemical reactions in air (Smith [1993])

heating and compressing a gas is to do so using successively an incident and then reflected shock wave. This is the idea behind the shock tunnel and, to obtain a reservoir temperature of around 10,000 K, a shock speed of over 5 km/s would be required. Furthermore, as the shock strength required increases, the test time available decreases due to contamination of the reservoir by the gas, usually a mixture of Helium and Argon, driving the shock wave into the test gas. While this may be a problem for every kind of experiment, some are also particularly susceptible to freestream noise. In true flight conditions, the flow is usually deemed to be "quiet," i.e., free of external disturbances. This cannot be duplicated in the lab because of problems ranging from model vibration inside the test section to, more seriously, acoustic radiation from the nozzle walls into the freestream.

A recent and quite complete discussion of current hypervelocity testing capabilities and their limitations can be found in Boudreau and Smith [1993]. Major classes of facilities are summarized in Figure 1.3 below.

1.2 The high enthalpy boundary layer

Because of all the difficulties associated with hypervelocity testing, one would not expect boundary layers to be very amenable to experiments in any of the existing facilities. Boundary layers are very sensitive to flow conditions and in particular to external disturbances. Measurements, if not careful, can be misleading and conclusions, erroneous. However, it is nevertheless a problem of great

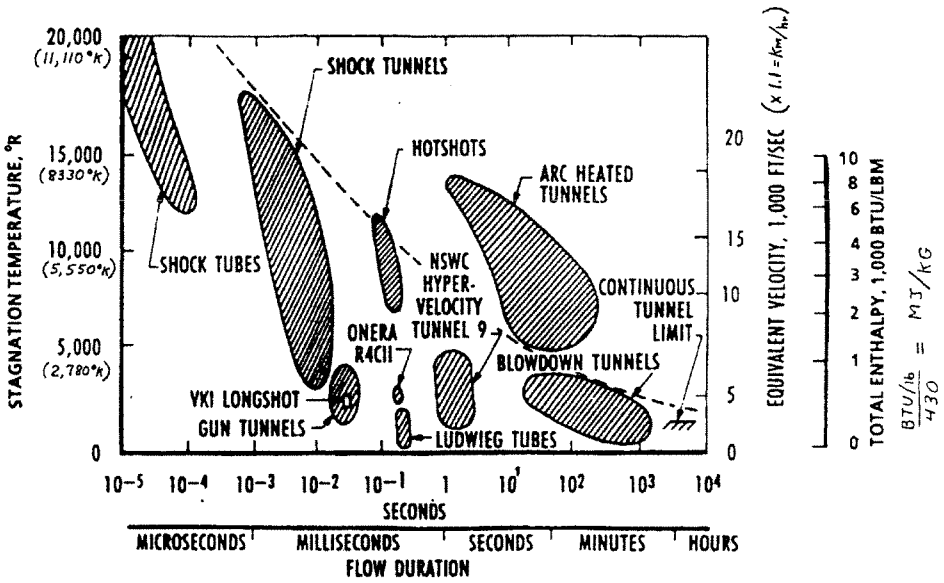

Figure 1.3: High temperature tunnel capabilities (Crawford [1993])

interest as pointed out by the quotes in the opening paragraphs. Vehicle and propulsion system design rely heavily on knowing the state of the boundary layer. After all, it is at the boundary layer level that most of the heat is transferred to the vehicle body and therefore predicting and modeling its behavior is critical to the design of thermal protection systems and thrust requirements. This is particularly true when one thinks about the large difference in heat transfer rate between a laminar and a turbulent flow.

The concept of a boundary layer, the narrow region in a wall-bounded shear flow where viscous effects must be accounted for, was first introduced at the turn of the century by Ludwig Prandtl. Since then, boundary layers of all kinds have been the subjects of enormous curiosity not only as a fundamental fluid mechanics problem but also because of the basic engineering need to be able to predict their behavior. Incompressible laminar boundary layers, at very low Mach numbers, are well understood and discussed at length in the many textbooks as well as treatises (e.g. Lagerstrom [1964], Rosenhead [1963], Schlichting [1979], White [1991]). Solutions can be derived for many simple geometries and cases - flat plates or sharp cones, for example. Expressions can then be obtained for most quantities of interest such as velocity profiles, skin friction, and heat transfer distribution. Much research has also gone into describing the laminar boundary layer's turbulent counterpart. Several theories have been put forward to model it and most of them are reasonably accurate to the point where they can be used as reliable engineering tools in common design situations.

An added degree of complexity characterizes compressible boundary layers, not only because the density is variable but also because the viscosity and thermal conductivity may depend on temperature. Much work has gone into solving laminar boundary layers of this type - subsonic, supersonic, and hypersonic - and discussions of the relevant equations as well as common problems can be found in many references ranging from Stewartson [1964] and Dorrance [1962] to more recently White [1991] and Anderson [1989,1990]. Furthermore, because much of the work on compressible boundary layers preceded the development of the computer, many cases resort to approximations and transformations thereby rendering the nonlinear partial differential equations describing the flow more amenable to solutions. Finite difference computations are, in general, now the norm. Models of compressible turbulent boundary layers are far less accurate than the incompressible ones and still the subject of many investigations and discussions (Dussauge *et al.* [1995]).

As the flow speed increases to several kilometers per second, as in the hypervelocity flows discussed in the previous section, the gas begins to dissociate and possibly even ionize. Additional equations must then be provided to complete the solution and account for the chemical reactions - frozen, equilibrium or nonequilibrium. One example of early work on the numerical solution of boundary layers in chemical nonequilibrium was carried out by Blottner [1964], with and without ionization, on a flat plate, cone and hemispherical cylinder. It should also be noted that many such calculations relied on a separate inviscid calculation of the external flowfield then used as an edge boundary condition for the viscous boundary layer solution. Fully viscous codes with thermochemical nonequilibrium are now used for the entire flowfield around the body of interest from the attached, or detached, shock wave to the boundary layer (Candler [1988]).

Correctly modeling the chemistry remains, however, one of the greater challenges. Reactions and their corresponding rates are poorly understood. Surface catalycity is also a subject of great interest, finite rate chemistry occuring not only in the gas phase of boundary layers but at the wall as well. One recent study was performed by Miller *et al.* [1995] with examples of possible species profiles shown in Figure 1.4 below. The chemical composition of the boundary layer is therefore heavily dependent not only on the chemistry within the layer but also on the catalycity which in turn affects the other fluid properties and, most importantly, the heat transfer at the wall. A discussion of gas-surface interactions can be found in Park [1990].

The greater challenge in the understanding of hypervelocity boundary layers stems from the lack of experimental data needed to validate the recent computations and, perhaps more importantly, to point to phenomena and interpretations that might otherwise be overlooked. High enthalpy hypervelocity facilities are expensive to operate and flight data are even more difficult to come by. Flow

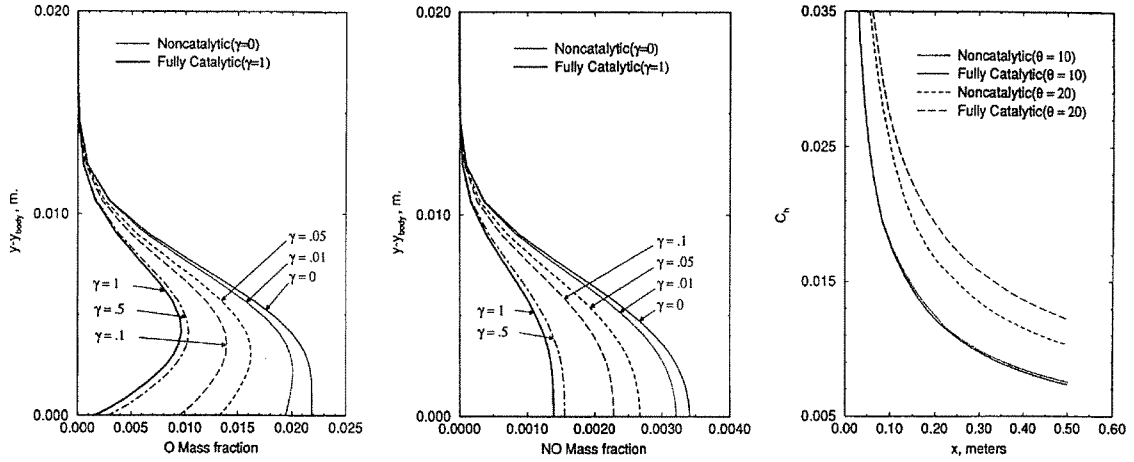

Figure 1.4: Species profiles in a nonequilibrium laminar air boundary layer on a 10° cone with finite catalytic walls. Also shown is the heat transfer distribution for 10° and 20° half-angle cones. (Miller *et al.* [1995])

visualization and surface heat transfer measurements may be enough to quantify the chemistry and degree of nonequilibrium in blunt body flows where much can be learned from the shock shape or stand-off distance (Wen and Hornung [1995]). A standard technique such as holographic interferometry (Sanderson [1995]) can yield quite accurate local flowfield information from a single snapshot of fringe shifts, i.e., of the density changes throughout the flow.

Acquiring similar information about the degree of nonequilibrium in a hypervelocity boundary layer is equally difficult not only because of the flow conditions but also because of the scale at which the phenomena of interest occur. Most studies are therefore forced to rely on surface heat transfer measurements to then infer the chemistry at the edge of and within the boundary layer, as well as surface reactions. One such example is the flat plate experiment by Vidal and Golian [1967] where the edge atom concentrations were calculated for catalytic and noncatalytic walls in dissociated oxygen flows. East *et al.* [1980] also inferred possible gas-phase and surface reactions from their heat transfer measurements on a flat plate in high enthalpy air flows. A more recent experiment is the one by Gai and Joe [1992] on blunt cones where some differences between the theoretical laminar heat transfer results and the data are again attributed to possible, but not definite, nonequilibrium reactions.

Essentially, one would like to sample the inside of the boundary layer itself. Any probe would most probably affect the flow, and hence the chemistry, making nonintrusive techniques a must. Furthermore, any instrument inserted within the boundary layer would have to be designed to sur-

vive the extreme environment reaching temperatures of several thousands of degrees. Mallinson *et al.* [1996] obtained digital interferograms of the boundary layer over a wide range of enthalpies and subsequently analyzed the fringe shifts to obtain the corresponding density profiles. However, the two examples shown in Figure 1.5 below clearly illustrate that much remains to be done as far as improving this measurement technique and perhaps improving the theoretical predictions are concerned. Laser based diagnostics are perhaps the most promising, to date allowing mostly quantitative single-species point measurements (Cummings [1995]) or more qualitative planar information (McMillin *et al.* [1993]). Time-of-flight mass spectroscopy has been shown to work well in shock tunnels and gives time dependent multiple-species information (Skinner [1994]). Intrusiveness of the instrument, however, remains a problem.

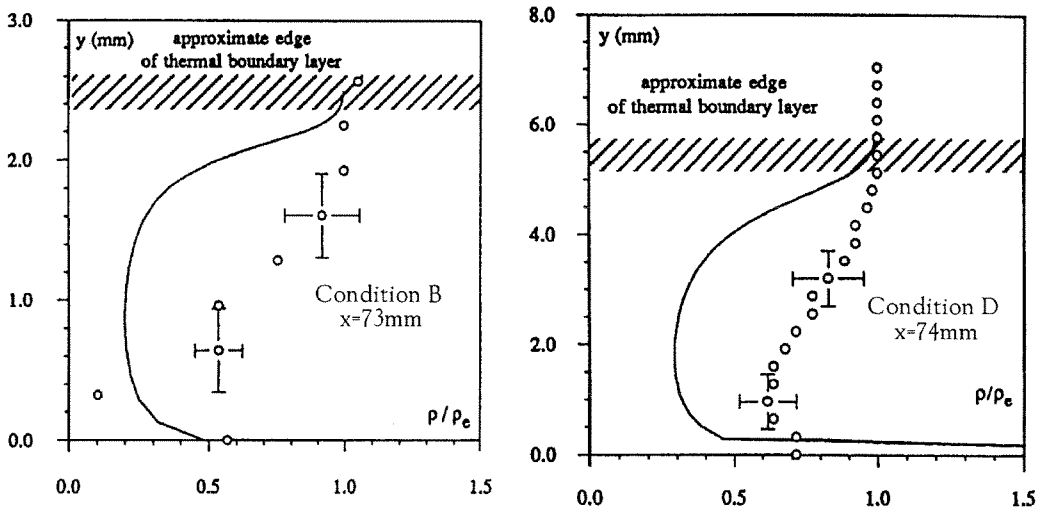

Figure 1.5: Density profiles computed from experimental Mach-Zender interferograms (Mallinson *et al.* [1996]). The symbols correspond to the experiment whereas the solid line corresponds to the theoretical prediction. For condition B, $h_0 = 19.0\,\mathrm{MJ/kg}$ and $P_0 = 22.2\,\mathrm{MPa}$; for condition C, $h_0 = 13.7\,\mathrm{MJ/kg}$ and $P_0 = 22.2\,\mathrm{MPa}$. $M_\infty = 7.5$ in both cases.

1.3 Stability and transition issues

Early boundary layer stability theory can be traced back to work by Tollmien and Schlichting, an account of which can be found in Schlichting [1979]. Incompressible laminar boundary layers are destabilized by viscosity and transition to a turbulent state. Instability waves were measured in a flat plate boundary layer flow for the first time by Schubauer and Skramstad [1948]. Boundary layer stability theory and experiments grew thereafter to include studies of effects such as freestream turbulence, geometry, wall cooling and heating, blowing and suction, pressure gradients, etc. The

instability waves responsible for incompressible boundary layer transition are often referred to as the Tollmien-Schlichting waves. A schematic from White [1991], shown below in Figure 1.6, depicts the transition process on a flat plate, from the amplification of the instability waves to the onset of turbulence. A recent and detailed review of the actual mechanisms behind the transition processes in incompressible flows can be found in Kachanov [1994].

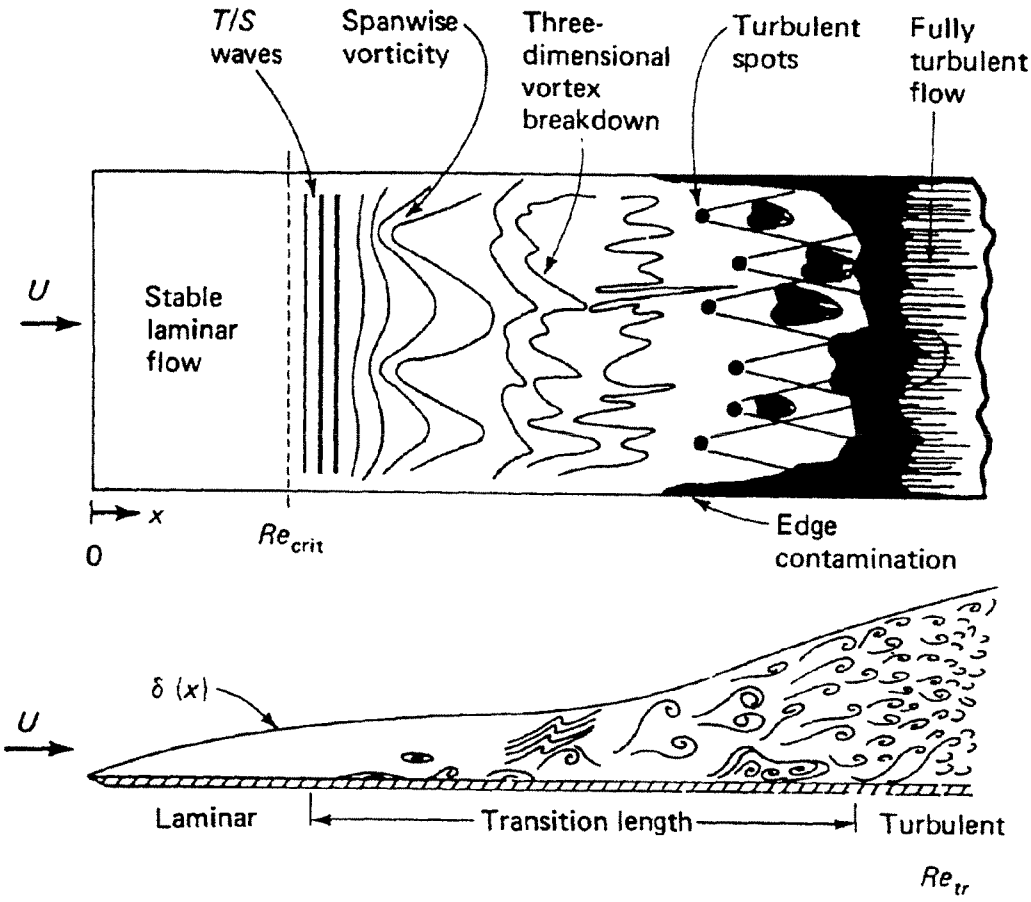

Figure 1.6: Illustration of the transition process on a flat plate (White [1991])

Cooling the wall was found to have a stabilizing effect on these Tollmien-Schlichting waves thereby delaying the transition to turbulence.* However, this theoretical result did not seem to be consistent with the experiments performed in high Mach number compressible boundary layers which actually appeared to be destabilized by the cooling (Stetson and Rushton [1967]). Further refining of the Tollmien-Schlichting based theory still failed to reveal the true reason for this "transition reversal" that appeared as the Mach number was increased (Reshotko [1963]).

*As a side note, while cooling stabilizes air boundary layers, it is heating that actually stabilizes water boundary layers because of the opposite behavior of the viscosity with temperature (Liepmann and Nosenchuck [1982])

It took the theoretical and analytical boundary layer stability work of Mack [1969,1984] to elucidate this seemingly paradoxical behavior: at higher Mach numbers further instability modes appear. This was missed in all of the earlier asymptotic analyses which, because of the simplifications involved, neglected certain terms indeed unimportant at low supersonic Mach numbers but nevertheless crucial at higher ones. These instability modes, commonly referred to as the Mack modes, are acoustic in nature and appear at higher frequencies, the corresponding wavelengths scaling to roughly twice the boundary layer thickness. A recent review of linear stability theory for both subsonic and supersonic boundary layers has been written by Reed and Saric [1996].

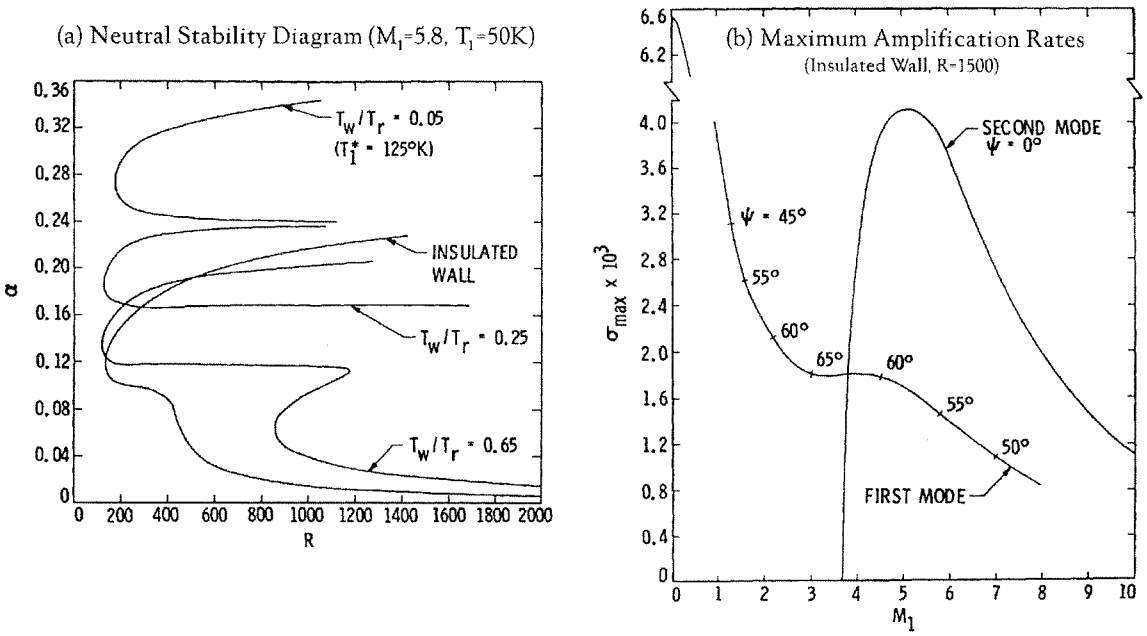

Figure 1.7: Typical (a) neutral stability and (b) amplification rate curves (Mack [1984]).

Figures 1.7(a) and (b) above depict typical neutral stability and amplification rate curves. In Figure 1.7(a), the different curves trace the neutral limits: to the right of the curves the waves are unstable, to the left they are stable. The insulated wall and higher T_w/T_r curves show that at this fixed Mach number, there can be both a Tollmien-Schlichting type instability - the lower peak - and a Mack type instability - the upper peak. At the lower values of T_w/T_r only the Mack mode appears, the other instability being unconditionally stable. In these compressible flows, the Tollmien-Schlichting instability is often referred as the "first mode"† and the higher frequency Mack instability as the "second mode." Figure 1.7(b) illustrates how the second mode overtakes the first

†One reason for the different terminology is that the incompressible Tollmien-Schlichting instability is viscous in nature, i.e., all wave numbers are damped at sufficiently high Reynolds numbers. Conversely, compressible instabilities are inviscid.

one as the most unstable mode beyond a certain Mach number. It should be noted that while first mode waves have the largest amplification rates when they are at an angle with respect to the cross flow, the second mode waves are most unstable when parallel.

Along with the development of the theory, several boundary layer transition and stability experiments were performed, notably the supersonic work by Laufer and Vrebalovich [1960] and the hypersonic work by Demetriades [1960]. However, these experiments were conducted without any knowledge of Mack's second mode instabilities. The discovery of the second mode's existence led to more focused experiments with controlled disturbances used to study both "natural" and "forced" transition. Kendall [1967], for example, used surface mounted electrodes on a flat plate to artificially introduce oblique and parallel disturbances into the boundary layer thereby confirming the results from linear stability theory. Similar hypersonic transition and stability work, with and without controlled disturbances, has been carried out extensively since then by many other research groups. A somewhat recent review summarizing work done at Mach numbers of 6 and 8 is given in Stetson and Kimmel [1992]. Equally extensive work looking at not only the influence of typical factors such as Mach number and temperature ratios but also of dissociation and ionization - albeit over very limited ranges - is reviewed in Lysenko [1993].

Recently, the push has been to better duplicate flight-like conditions in the tunnel: high enthalpy flows to match the exact flight speeds rather than Mach number and "quiet" flow to match the disturbance level in the atmosphere surrounding the vehicle. Transition measurements are very sensitive to the facility in which they are obtained (Pate [1971], Owen *et al.* [1975]) most probably because of differences in the noise spectrum which can undesirably amplify instabilities that would otherwise remain stable. In free flight, the noise level is low and transition proceeds "naturally" via the most unstable modes. Quiet tunnels are designed for natural transition, their performance being measured by how small the freestream fluctuations are kept. Most of the noise comes from the side wall boundary layers, not only in the test section where the model lies, but more importantly in the nozzle which expands the flow from the reservoir to the desired freestream conditions. The longer these boundary layers are kept laminar, the less the noise radiated into the flowfield and the more "quiet" the flow. It is easy to see that shock tunnel generated flows can be notorious sources of noise in addition to the particulates that may enter the freestream. It is also quite obvious that one must compromise, at least as far as current capabilities go, between a quiet flow and a high enthalpy one.

A few boundary layer transition experiments have been performed in quiet facilities. Measured transition Reynolds numbers, for the most part, compare well with free flight results as shown below in Figure 1.8 taken from Chen *et al.* [1989]. What is particularly noticeable is the fact that the

measured transition Reynolds numbers for both free flight and quiet tunnels all lie over an order of magnitude above the corresponding shock tunnel measurements. This is commonly attributed to bypass mechanisms or simply the fact the transition mechanism is most probably of a different mode in the different cases. More recent quiet tunnel work can be found in Lachowicz *et al.* [1996], Schneider *et al.* [1994] as well as in Schneider and Haven [1995].

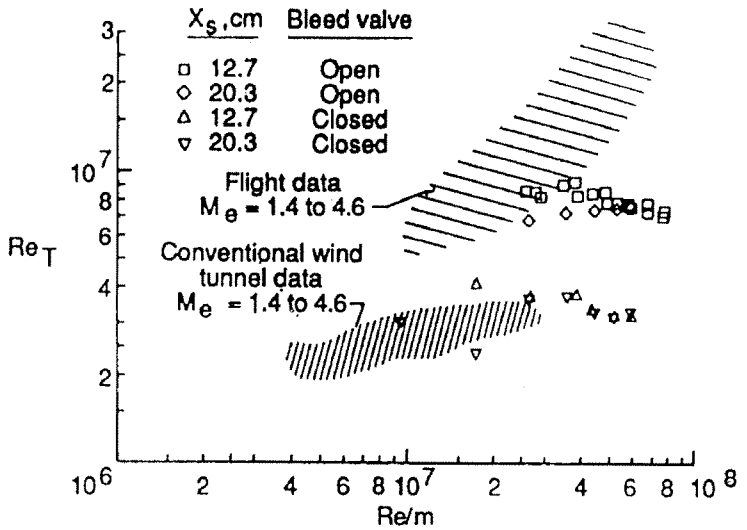

Figure 1.8: Comparison of wind tunnel and free flight transition Reynolds numbers (Chen *et al.* [1989])

Many linear stability calculations have been performed for reentry flows but with limited, if any, chemistry modeling. Results based on the e^N criterion for transition (Smith and Gamberoni [1956]) agree quite well with free flight measurements as shown in Figure 1.9 below. In this model, the boundary layer is assumed to transition once the amplification factor of one of the many unstable waves reaches e^N, with N usually set around 10. This is defined as the most unstable frequency and, for sufficiently high Mach number hypersonic flows, it is the second mode as discussed earlier. Germain and Hornung [1997], however, observed in their experiments that transition might nevertheless occur via the lower first mode instabilities. This suggests the possibility that the mechanisms are different in hypervelocity tunnels causing the boundary layer to transition earlier than it would in quiet tunnels and consequently in free flight.

There is, however, an important caveat. Correctly simulating reentry flows requires more than just matching the Reynolds numbers; the speed and hence the enthalpy must also be matched since it is the resulting high temperatures that properly duplicate the true physical and chemical behavior

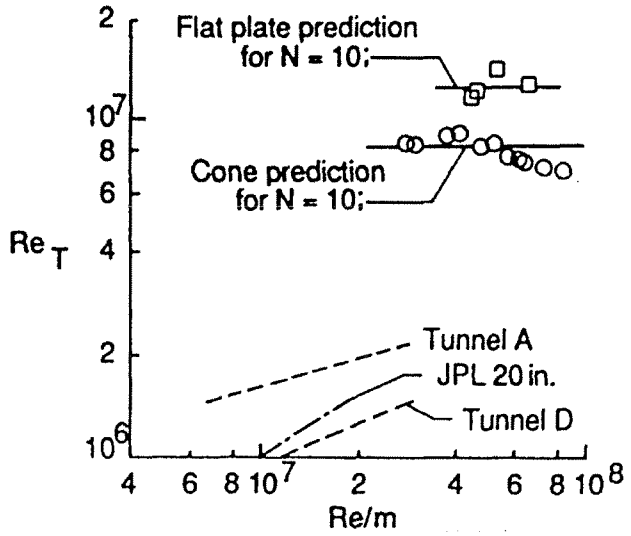

Figure 1.9: Comparison of experimental transition Reynolds numbers and e^N results (Chen *et al.* [1989])

of the flow in free flight. No quiet tunnel is capable of producing such a high enthalpy flow and none of the stability calculations performed to date, although seemingly predicting quite well the observed transition Reynolds numbers, account for the complete thermochemical nonequilibrium phenomena. Furthermore, since no high enthalpy flight stability data exist, there is no way of being certain the instabilities responsible for transition in flight are the same as those predicted by the simplified theories and measured in the tunnels.

Some theoretical and computational work has been done on the stability of reacting boundary layers, notably by Malik and Anderson [1991] as well as by Stuckert and Reed [1994]. For the most part, however, only equilibrium chemistry has been considered with few nonequilibrium results. The general consensus from these studies is that the second mode is the most unstable and its frequency shifts to lower values as real-gas effects are accounted for. More work, however, is necessary to properly appreciate what happens at higher temperatures when dissociation and possibly ionization occurs. More recent numerical investigations by Hudson *et al.* [1996] and Seipp [1997] address this issue and show that real-gas effects within the boundary layer also stabilize the second mode. In order to complement, and perhaps guide, these computations one therefore needs experimental transition data over a large enthalpy range as well as stability data. To date, very few such experiments have been performed. Some stability results for a high enthalpy flat plate boundary layer have been obtained by He and Morgan [1994] in the T4 shock tunnel at the University of Queensland and some transition results on a sharp cone by Germain [1994] in the T5 shock tunnel at Caltech.

1.4 Previous work in T5 and scope of this study

The purpose of this study is to build on previous hypervelocity boundary layer studies, in particular those conducted in the T5 free-piston shock tunnel at GALCIT, and to further our understanding of the enthalpy related effects on these flows. Germain [1994] performed an exploratory study on a sharp cone in T5 and, in his experiments, observed laminar, transitional and turbulent boundary layers over a variety of enthalpies and pressures within the tunnel's performance envelope. The range of conditions was chosen to highlight differences between perfect gas and thermochemical nonequilibrium flows. Most of these tests were performed in air and nitrogen although a few were performed in helium, a nonreactive flow case, and in carbon dioxide, an easily excitable and dissociable gas. In parallel with the heat transfer measurements on the cone to determine the state of the flow, Germain obtained resonantly enhanced interferograms and shadowgraphs of the boundary layer offering some insight into the transition mechanism and the turbulence structure. Although actual stability calculations have yet to be performed, what appear to be Tollmien-Schlichting waves can be seen in some of the photographs which seems to contradict theoretical predictions that the second mode instabilities should be dominant. Germain also observed that normalizing the transition location by the reference temperature condition might be more appropriate to illustrate enthalpy effects.

The present thesis opens, after a brief introduction, with a review of the experimental approach in Chapter 2. The facility and model are described as well as the instrumentation and the limitations of the experiments. Chapter 3 describes the numerical approach taken to complement the tunnel data. A brief description of the code is given and the chemistry models used are discussed . Laminar and turbulent heat flux models, as applied to the flows to be studied are reviewed in Chapter 4. Chapter 5 discusses observations of enthalpy effects on boundary layer transition. In particular, the issue of how to normalize the transition location and the reservoir enthalpy to best represent the flow is addressed. Chapter 6 compares the T5 transition results with some obtained on a free flight experiment. Experimental and numerical results for enthalpy effects on laminar boundary layer heat transfer are then presented in Chapter 7. The test gases investigated include air, nitrogen, and carbon dioxide. Finally, some conclusions and recommendations for future work are proposed. The issue of hypervelocity boundary layer stability has yet to be addressed but it is hoped that much insight into the phenomena will be gained from the present work.

Chapter 2 Experimental Approach

2.1 The T5 free-piston shock tunnel

All experiments were carried out in GALCIT's hypervelocity flow facility: the T5 free-piston shock tunnel. The facility consists of four major sections as shown below in Figure 2.1: the secondary air reservoir (2R), compression tube (CT), shock tube (ST) and a test section (not shown). At the beginning of a typical run, the free piston is loaded at the 2R-CT junction and is accelerated down the CT with high pressure air from the 2R. The piston compresses rapidly, and thus adiabatically, the mixture of mostly helium and some argon against a stainless steel pre-scored diaphragm that separates the CT from the ST. The thickness and scoring depth of the diaphragm depend on the run conditions desired: e.g., a 0.25 inch diaphragm with a 0.04 inch groove will burst at roughly 90 MPa. As the bursting takes place, the high-pressure high-temperature gas originally

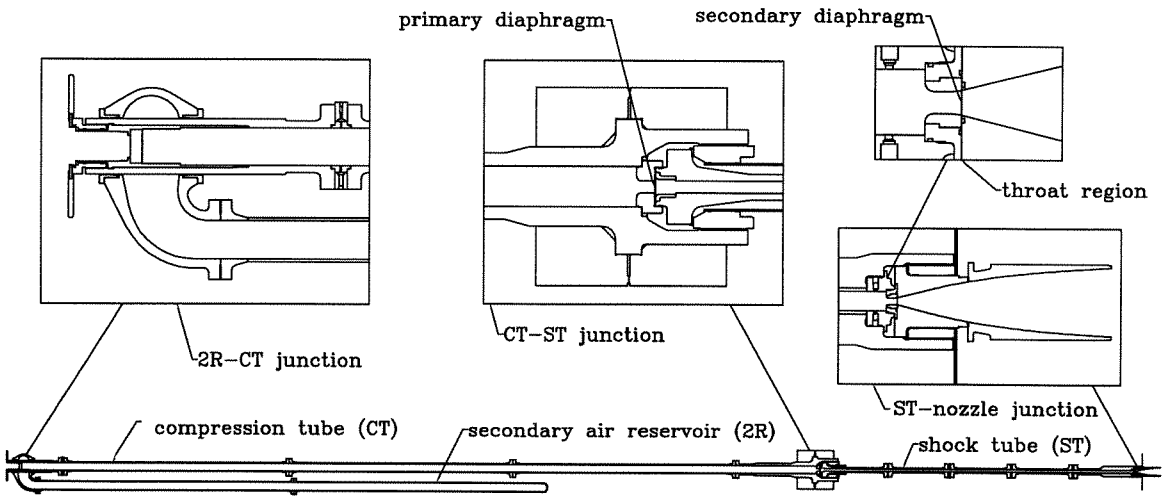

Figure 2.1: T5 hypervelocity shock tunnel

in the CT is exposed to the lower pressure test gas in the ST and "drives" a shock wave, formed because of the pressure discontinuity, towards the end of the ST, heating and compressing the then "driven" test gas. At the end of the ST, the shock wave reflects, further compressing and heating the test gas but also bringing it to rest, thereby creating a stagnation reservoir. Upon reflection, a thin Mylar diaphragm at the ST end wall ruptures and the test gas in the reservoir is accelerated through a nozzle into the test section over the instrumented experimental model to be tested. The end of the test section connects into a dump tank which is vented to the outside once the run is over.

Typical pressures in the secondary air reservoir vary from a few hundred to over 1500 psi, depending of the diaphragm thickness. Standard diaphragms are designed to burst from 32 MPa to 120 MPa, corresponding to stagnation pressures, P_0 from 15 MPa to over 100 MPa. The compression tube is usually filled with a mixture of helium (80% to 100%) and argon at pressures between 40 and 140 kPa. A high-temperature, high-pressure monatomic gas in the driver section increases the shock Mach number that can be obtained when the diaphragm bursts (Hornung and Bélanger [1990]). The shock tube is filled with the desired test gas at pressures around or below atmospheric. Common test gases include air, nitrogen and carbon dioxide although hydrogen and helium have also been used. Typical shock speeds range from 2 km/s to 5 km/s and corresponding enthalpies from 4 MJ/kg to 27 MJ/kg in air and nitrogen. Two Mach 5 nozzles (32 cm exit diameter, 31 mm throat) are currently in use; one has a contoured supersonic section and one is conical. The throat section can be swapped for a different one depending on the desired conditions. Tests usually last a few milliseconds, the time the reservoir remains at a constant pressure level after the shock first reflects off the end wall. Useful time for measurements, however, is much shorter due to the contamination of the test gas by the driver gas despite seemingly constant reservoir conditions (Sudani and Hornung [1997]). A typical reservoir pressure trace is shown below in Figure 2.2; measurements would only be taken between around 1.0 ms $\pm$ 0.1 ms in the constant pressure region.

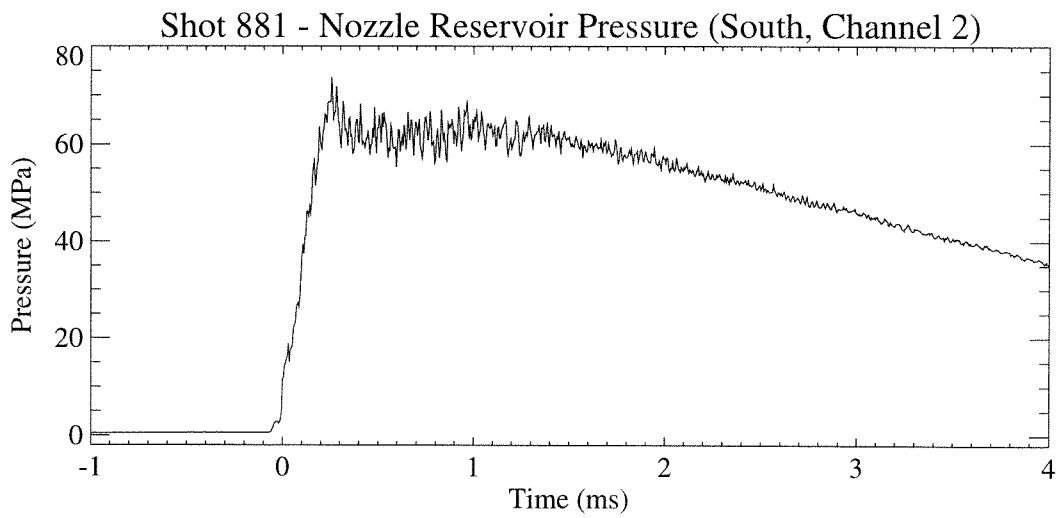

Figure 2.2: Typical nozzle reservoir pressure trace

The data acquisition system consists of several digitizers, amplifiers, power supplies, memory modules, an interval counter and a trigger generator all controlled through a Sun Sparcstation. Typical tunnel parameters recorded during a run are the compression tube and secondary reservoir

recoils, the diaphragm burst pressure P_4, the stagnation pressure P_0 and the shock tube pressure at four points in the tube to pick up the shock's passage and hence its speed. Typical instrumentation on experimental models include coaxial thermocouples for heat transfer rate measurements and pressure transducers. A total of 48 channels of data can be recorded for any given experiment in addition to the standard tunnel parameters. All 48 channels can be sampled at a maximum of 200 kHz although two independent channels can be freed up by only using two pressure transducers in the shock tube and sampled as fast as 1 MHz.

The test section is equipped with two side windows, and an optional downward looking one, for flow visualization. Several techniques have been developed for T5. Typically, resonantly enhanced shadowgraphs or interferograms are taken using a dye laser tuned to the sodium D line and pumped by a pulsed Nd:YAG laser. The resonant enhancement is obtained by seeding the flow with sodium from a solution deposited upstream of the nozzle or directly on the model. A description of the technique can be found in Blenstrup *et al.* [1979] and a detailed explanation of the setup in T5 in Germain [1994]. A rough schematic of the setup, with respect to the test section and the model to be described in the following section, is shown in Figure 2.3. Another technique developed for T5 but not used in the present experiments is holographic interferometry. A description of the optical arrangement and its design is described in Sanderson [1995].

2.2 The model and instrumentation

The model chosen for these boundary layer studies is a 1 meter long, 5° half-angle cone. The cone was designed by Germain [1994] for his earlier exploratory studies in T5 and has not been modified, apart from instrumentation changes to be described below, for the present set of experiments. The choice of a cone is a natural one since boundary layer measurements on axisymmetric configurations are not contaminated by end effects no matter how long the model is. Long models are also desired for boundary layer studies to be able to observe the entire transition process at a given condition along the full model. The only limitation on the length is the tunnel size and in particular interference from the nozzle and side walls. Furthermore, laminar and turbulent flat plate theories can be extended via coordinate transformations to cones (White [1991]). Transition and stability measurements have been found to correlate as well (Pate [1971]). 5° half-angle cones have also been the subject of other studies - experimental, numerical and in-flight - thereby allowing the data to be compared and the range of previous measurements to be extended.

A drawing of the model as mounted inside the test section on its sting and support is shown in Figure 2.4. The model is made of three sections: a sharp tip screws into a mid-section which screws

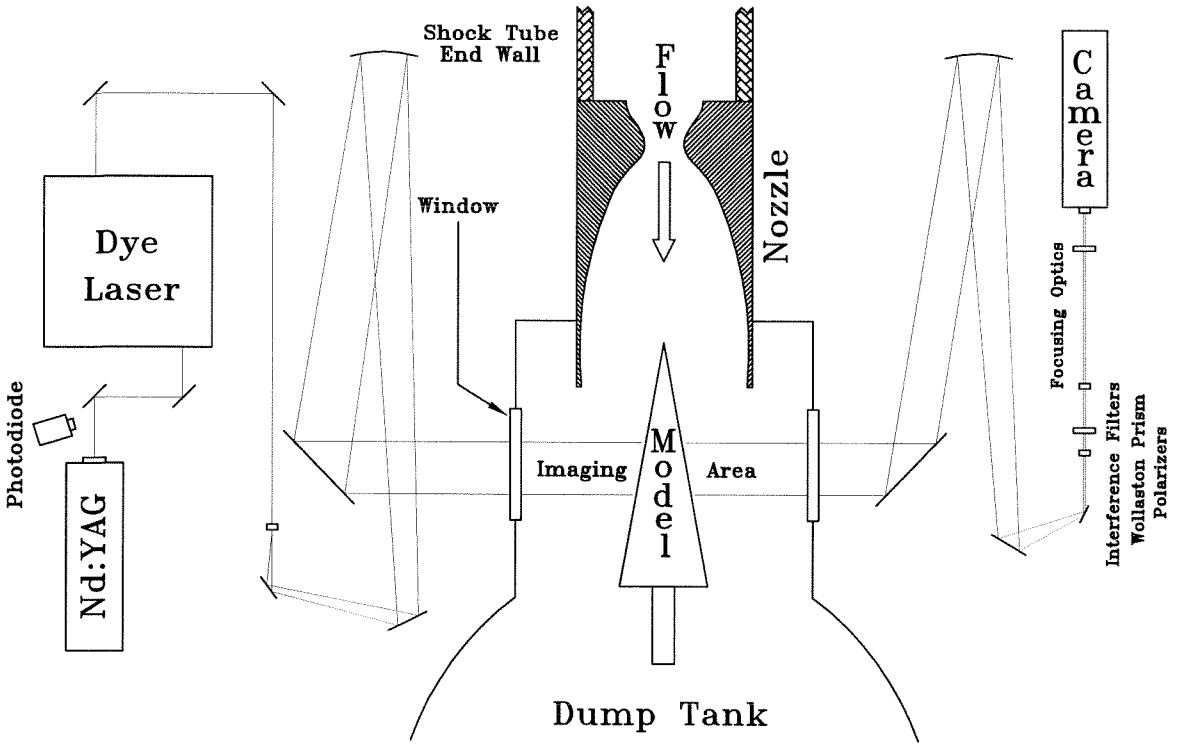

Figure 2.3: Optics layout for shadowgraphs and interferograms

into the main body. The main body is made of aluminum and consists of two dove-tailed halves which slide and lock into each other thereby eliminating the need for external fasteners. The mid-section is also made of aluminum; however, the tip is made of molybdenum. This is the same material as the nozzle's throat and was chosen because of its resistance to the high heat load encountered at the stagnation point. The tip, nevertheless, does eventually wear out and can be replaced. Bluntness varies from a radius of curvature of 0.00025" for a new tip to 0.004", the value at which it stabilizes after several shots. Previous studies indicate that this does not affect the measurements (Germain [1994]). The cone is aligned at angles of attack and yaw of no more than 0.02°. It protrudes by about 33 cm into the nozzle and lies approximately 6.5 cm above the centerline.

One way of deducing the state of the boundary layer - laminar, transitional or turbulent - is by measuring the heat transfer rate along the cone. For this purpose, the main body of the model is instrumented with type E coaxial cylindrical thermocouples (chromel-constantan) mounted flush with the model surface. The gage distributions (axial position, roll angle and resistance across junction) for the three series of experiments carried out in T5 for the present study are tabulated in Appendices A.1 through A.3. Thermocouples manufactured by Medtherm Corp. were used for the first series. These were the same gages that had been previously installed by Germain [1994]. For

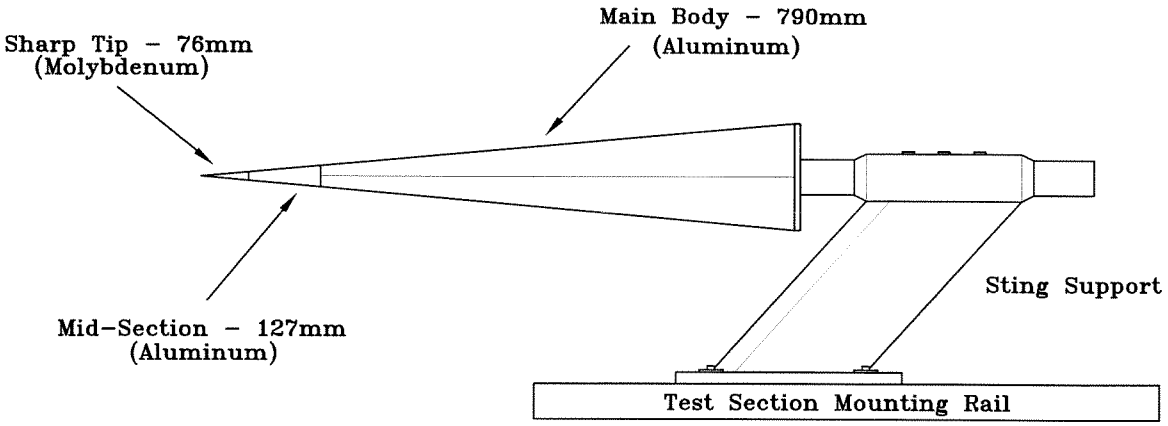

Figure 2.4: Model sections and mounting arrangement

the second series, however, new thermocouples were installed alongside the older gages. These were built in-house according to a low-noise design by Sanderson [1995] but using the same materials as the Medtherms. The Medtherm gages measure 1.6 mm in diameter whereas the Sanderson gages measure 2.4 mm. The number of thermocouples mounted on the model, 14 and 19 for the first and second series of tests respectively, was limited by the number of recording channels available on the data acquisition system at the time. An upgrade of this system allowed over 50 gages to be installed for the third and last series (Figure A.1). Although only 48 temperature traces could be recorded at a time, the extra thermocouples were located to provide additional resolution if desired. All traces were sampled at 200 kHz after having been amplified by a factor of 500.

2.3 Heat transfer calculation and flow parameters

From the measured time history of the temperature along the model surface, one can compute the heat transfer rate. Since the test time is very short compared to the heat penetration time, a one dimensional semi-infinite solid theory is adequate to model the problem. Two approaches are possible and are outlined in Schultz and Jones [1973]. The direct method consists in integrating directly the time rate of change of the digitized temperature traces:

$$\dot{q}(t) = \sqrt{\frac{\rho c k}{\pi}} \int_0^t \frac{dT(\tau)}{d\tau} \frac{d\tau}{\sqrt{t-\tau}}. \tag{2.1}$$

In the indirect method, however, the time history of the integrated heat is first obtained from the following integral:

$$Q(t) = \sqrt{\frac{\rho c k}{\pi}} \int_0^t \frac{T(\tau)}{\sqrt{t-\tau}}\, d\tau \tag{2.2}$$

or, since the data are actually discrete, in finite difference form:

$$Q(t) = \sqrt{\frac{\rho c k}{\pi}} \sum_{i=1}^{n} \frac{T(t_i) - T(t_{i-1})}{\sqrt{t_n - t_i} + \sqrt{t_n - t_{i-1}}} (t_n - t_{n-1}). \tag{2.3}$$

Differentiating then yields the heat transfer rate

$$\dot{q}(t_n) = \frac{dQ(t_n)}{dt} = \frac{1}{40(t_n - t_{n-1})}(-2Q_{n-8} - Q_{n-4} + Q_{n+4} + 2Q_{n+8}). \tag{2.4}$$

The advantage of the indirect method is not only that it is easier to implement numerically, given the discrete data, but also that integrating before differentiating effectively smoothes the computed heat transfer rate. It should be noted, from Equation (2.3) that the absolute temperature need not be known but rather changes in temperature. The figure of merit for this type of thermocouple is the value of $\sqrt{\rho c k}$ taken as 8919 $\mathrm{Ws^{\frac{1}{2}}/m^2K}$, using the average of the values of the two gage materials: constantan and chromel. The overall error in heat transfer rate varies from $\pm 10\%$ to $\pm 25\%$ depending on the enthalpy. At low enthalpies most of the error comes from the averaging of the material properties and the variability over the useful test time. At higher enthalpies, one must also account for electrical noise and perhaps driver gas contamination which yield higher error bars (Germain [1994], Sudani and Hornung [1997]). Typical temperature change, integrated heat and heat transfer traces for a given thermocouple are shown in Figure 2.5.

In addition to calculating the heat transfer rate, it is necessary to know the flow properties at the boundary layer edge, in the freestream and in the reservoir. Flow properties such as the edge density, viscosity and velocity as well as the stagnation enthalpy and pressure are needed to normalize the data into proper nondimensional form and to characterize the boundary layer.

Conditions in the reservoir end of the shock tube are obtained by performing an equilibrium calculation given the reservoir pressure P_0, the initial pressure in the shock tube P_1, the shock speed v_s and the gas composition. P_0 and P_1 are measured directly whereas the shock speed is inferred by picking up the shock's position as it travels down the tube towards the end wall using pressure transducers or ionization gages. The actual equilibrium calculation is performed using one of two programs. The first is ESTC (**E**quilibrium **S**hock **T**ube **C**alculation) and was written by McIntosh [1970]; the second is STANJAN written by Reynolds [1986]. Thermodynamic properties in ESTC are based on harmonic oscillator approximations below 5000 K and curve fits above. In STANJAN, JANAF curve fits are used to represent the thermodynamic properties of each species. The programs output all the stagnation properties, in addition to the measured pressure, such as the temperature T_0 and the enthalpy h_0 as well as the gas composition. At the higher enthalpies and depending on

the gas, the reservoir can be highly dissociated and even ionized.

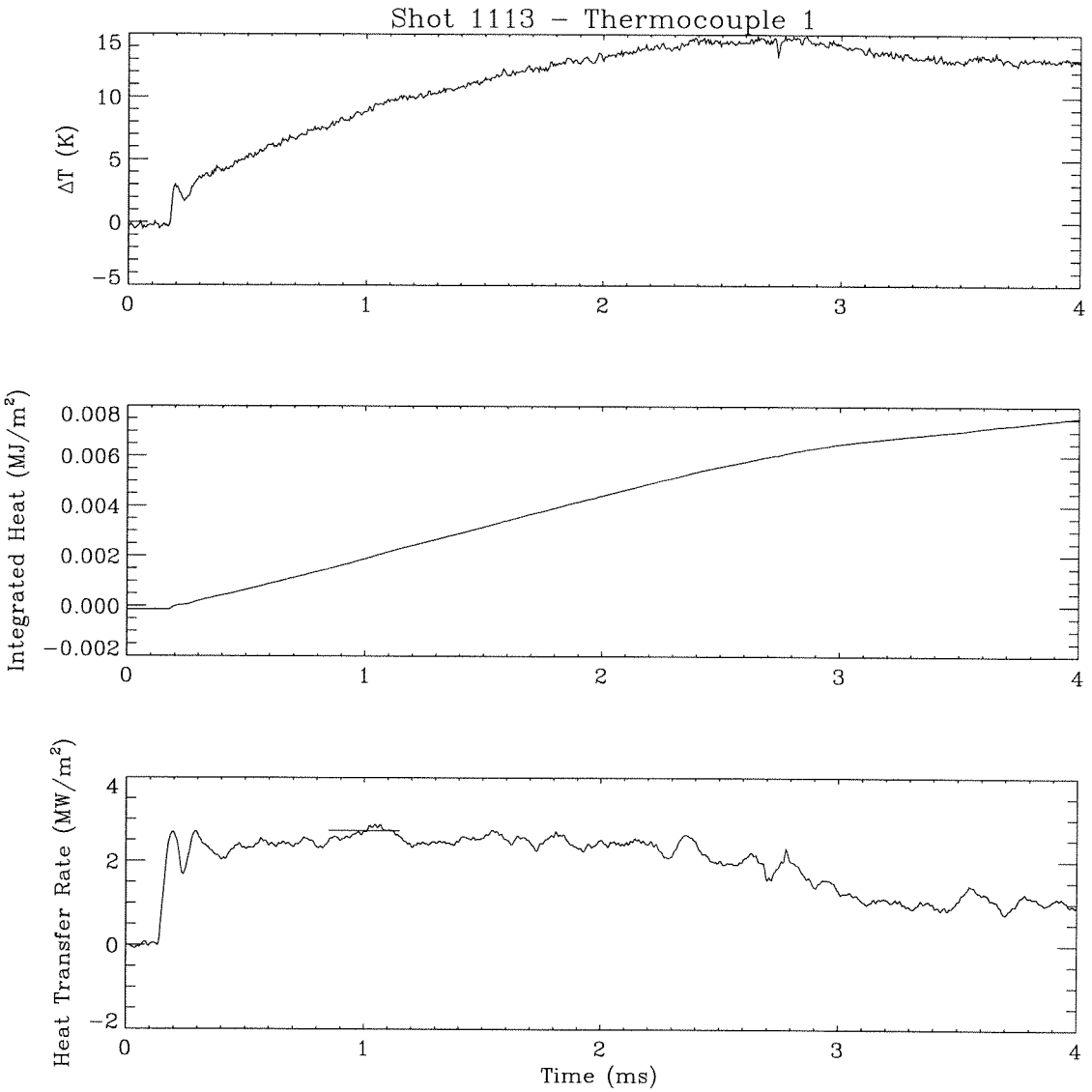

Figure 2.5: Typical temperature and heat transfer traces

Using these stagnation conditions as an input, the nozzle flow is then computed using a nonequilibrium one-dimensional inviscid nozzle flow code NENZF written by Lordi *et al.* [1966]. If a more accurate nozzle exit profile is desired, a two-dimensional code called SURF, developed at Caltech by Rein [1989] is also used. The output consists of all the freestream properties such as pressure P_∞, temperature T_∞, density ρ_∞, velocity u_∞ and gas composition, i.e., species mole fractions. Many of the dissociation reactions in the reservoir are reversed as the flow is expanded through

the nozzle and recombination takes place. However, the species concentrations usually freeze before reaching the exit and the amount of recombination is rarely enough to recover the equilibrium test gas composition at the test section.

Finally, it is necessary to find the boundary layer edge conditions. Assuming the gas composition is frozen - from the freestream, across the weak conical shock and to the edge - one can calculate an effective ratio of specific heats γ_f and use this to solve the classic equations of Taylor and Maccoll [1933] for supersonic flow over a cone. Denoting the compressibility factor as $Z = R_f/R_0$, where R_f is the frozen gas constant and R_0 is the ordinary gas constant at an undissociated state, γ_f is given by the following expression:

$$\gamma_f = \frac{4+3Z}{4+Z} \tag{2.5}$$

if the vibrational energy is also taken to be frozen and by the following expression:

$$\gamma_f = \frac{8+Z}{8-Z} \tag{2.6}$$

if the vibrational energy is at its fully excited equilibrium value (Vincenti and Kruger [1965]). The differential equations for conical flow can be solved accurately and rapidly with a simple fourth order Runge-Kutta scheme, iterating around the shock and body positions until the matching cone angle is found (Anderson [1990]).

2.4 Limitations of the experiment

While thermocouple measurements are indeed sufficient to deduce whether the boundary layer is laminar or turbulent, there are several limitations to the overall experiment that constrain the type and the amount of information that can be extracted from the data.

One would, for example, like to perform a frequency analysis on the heat transfer data. However, the thermocouple traces are sampled at 200 kHz thereby obscuring any signs of possible instabilities above 100 kHz. Furthermore, the power amplifiers used to amplify the voltage across the thermocouple junctions before going to the digitizer have cut-off frequencies of 100 kHz. Theory suggests that there exist two predominant instabilities in boundary layers at conditions similar to the ones in T5. The lower frequency instability is of the Tollmien-Schlichting type and is around 100 kHz. The higher frequency one, on the order of 1 MHz, is the most unstable one and is referred to as the Mack mode. It should be pointed out that neither one has ever been observed using temperature traces, even at conditions where the instabilities are at much lower frequencies. In T5, however, one would need to sample the data at a minimum of 5 MHz to confirm this. This has actually been

attempted, bypassing the regular amplifiers in favor of a selective high frequency amplifier and using a high frequency Tektronix TDS digitizing oscilloscope. Unfortunately, memory limitations do not allow for a long enough data sample to be meaningful at 5 MHz. Perhaps, the best way to look for the presence of instabilities in the flow is to try to excite them by deliberately disturbing the flow at the suspected frequencies.

Using resonantly enhanced shadowgraphs, Germain [1994] found that the dominant instability in transitional T5 boundary layers might be of the Tollmien-Schlichting type. Photographs of laminar and turbulent boundary layers were obtained as well. However, the present setup only allows for spatially integrated photography as illustrated earlier in Figure 2.3, i.e., the image captured on the film is really the sum of all the structures the laser column traverses from one side of the test section, over the model, to the other side. Visualization of a thin slice of the flow would be more informative. A laser sheet should be used for this purpose and actually already has, an intensified CCD camera being used instead of regular film. The available intensification, however, has proven to be insufficient, the camera being far from the sheet and the laser, perhaps, not powerful enough.

Finally, a more serious limitation is that although the boundary layer state can be quite well inferred from the heat transfer level, simple thermocouple measurements do not reveal any information about the inside structure of the boundary layer. One would like to know, for example, what the velocity, temperature and density profiles look like. More importantly, though, one would like to know what the exact species profiles are inside the boundary layer. This would shed some light on the chemical reactions taking place not only in the gas-phase but also at the surface. Understanding the exact chemistry and how it changes with enthalpy is essential to understanding the behavior of the laminar boundary layer and in particular, the behavior of disturbances that eventually lead it to transition.

Chapter 3 Numerical Approach

As was pointed out at the end of the previous chapter, in Section 2.4, heat transfer measurements along the cone's surface tell but one part of the story. They are essential for determining the state of the boundary layer - laminar, transitional, or turbulent - but do not reveal much about the inner structure of the boundary layer. In particular, one would like to know velocity, temperature, density and species profiles to understand the dynamics and the chemistry of the flow. This would in turn shed some light on the heat transfer process, i.e., the wall's catalycity and species diffusion, and on the transition mechanisms, i.e., how disturbances are affected by the chemical reactions. Ideally, time-resolved nonintrusive measurements of the quantities of interest would be needed. However, neither the data recording capability nor the actual instruments to perform the necessary tasks are available at this time in T5. Furthermore, one should keep in mind the extremely short test time available to take all the desired measurements.

Simulating the experiment by numerically solving the relevant physical and chemical equations is one solution that could enable us to probe the structure of the boundary layer, granted the model must be truly representative of what happens within the tunnel. A good test for any numerical model would be to see if it can reproduce the surface heat transfer levels measured in the laminar boundary layers from the experiments. However, given the edge conditions, the only part of the flow that actually needs to be solved is the boundary layer itself, i.e., from the edge to the wall.

It is also much more efficient to perform parametric studies using a code than by running experiments, especially in a tunnel such as T5 where tests are quite expensive and turnaround times quite long. Once confidence is established that the correct chemical reactions have been identified, one can easily vary enthalpy and pressure levels to study surface heat flux behavior and the actual boundary layer development. The chemistry itself can be varied to see how sensitive results are to the specified gas-phase reactions, the associated reaction rates and the possible surface reactions. One should, however, point out that while it is quite straightforward to write down the equations for a reacting laminar boundary layer, significant uncertainty still exists as far as the chemistry models are concerned. Nonequilibrium chemistry and catalycity are areas where a lot still needs to be learned. Modeling the turbulent part of the boundary layer is also of great interest but as far as the transition process goes, understanding the laminar portion should be the primary goal.

3.1 The BLIMPK code

The need for a fast but flexible boundary layer code is nothing new. In fact, during the design of the space shuttle, for example, in order to the select the best Thermal Protection System (TPS) possible, studies had to be carried out to look at reaction rate and surface catalycity effects on the heat transfer rate. Furthermore, this had to be done quickly for several possible vehicle configurations. This led to the development of BLIMP, a Boundary Layer Integral Matrix Procedure satisfying these requirements. At the time, fast meant that a solution had to be obtained with a minimal number of grid points. Flexible meant it had to be easy to try different chemical models, i.e., different species compositions, ablation models and boundary layer reactions.

Continuously updated since then, the latest version of BLIMP was renamed BLIMPK because of the addition of kinetics as an option. The code is therefore capable of simulating multicomponent boundary layers with frozen, equilibrium or nonequilibrium chemistry and is well suited to simulate the type of boundary layers encountered in T5. Unequal concentration and thermal diffusion are other options and laminar flows as well as turbulent flows (with built-in eddy viscosity models) can be computed. Gas phase reactions and surface reactions are parameters and a maximum of 15 transverse nodal points is all that is needed to capture the profile of the boundary layer. The number of possible streamwise nodes is unlimited.

A detailed description of the main program and the numerical scheme is available in Bartlett and Kendall [1967] for the first version of BLIMP including solely equilibrium chemistry. The nonequilibrium chemistry extension including surface reactions is discussed in Tong *et al.* [1973] and the various turbulence models are compared in Evans [1975]. A brief input guide for the latest version of BLIMPK, called BLIMP88, can be found in Murray [1988] and some suggestions for simulating T5 type boundary layers are pointed out in Adam [1996].

3.1.1 Conservation equations

The equations of mass, momentum, energy and species conservation for a multicomponent chemically reacting boundary layer are derived and discussed in Dorrance [1962] and Anderson [1989]. The coordinate system used is depicted below in Figure 3.1. s is defined as the coordinate along the body from the stagnation point, y as the coordinate normal to the body and r as the local radius in the boundary layer in the meridional plane.

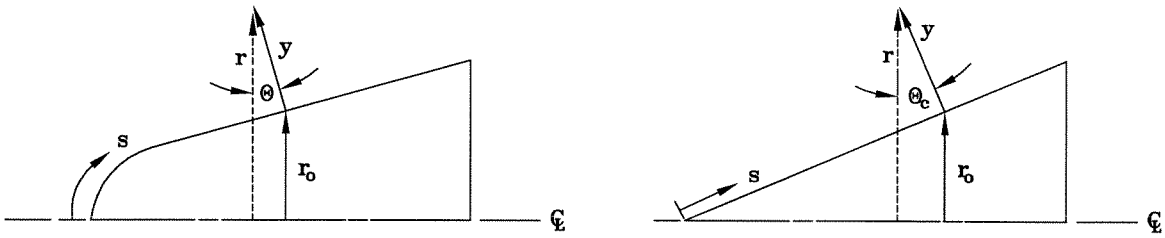

Figure 3.1: Coordinate system for blunt and sharp cones

Mass conservation is given by:

$$\frac{\partial}{\partial s}(\rho u r^{\kappa}) + \frac{\partial}{\partial y}(\rho v r^{\kappa}) = 0 \tag{3.1}$$

where κ equals 1 for axisymmetric flows and 0 for two-dimensional flows. The velocity components parallel and normal to the body are u and v respectively. ρ is the density.

Momentum conservation is given by:

$$\rho u \frac{\partial u}{\partial s} + \rho v \frac{\partial u}{\partial y} = \frac{1}{r^{\kappa}} \frac{\partial}{\partial y} \left[\rho r^{\kappa} (\nu + \varepsilon_M) \frac{\partial u}{\partial y} \right] - \frac{\partial p}{\partial s} \tag{3.2}$$

where ν is the kinematic viscosity, ε_M the turbulent eddy viscosity, and p the pressure. It should be noted that the empirical turbulent terms are carried along throughout this section for the sake of completeness. It is only the application of these equations to laminar flows that is really of interest, laminar flows being modeled more reasonably than their turbulent counterparts, especially when compressibility and reactions come into play.

Energy conservation is given by:

$$\begin{aligned} \rho u \frac{\partial H_T}{\partial s} + \rho v \frac{\partial H_T}{\partial y} = & \frac{1}{r^{\kappa}} \frac{\partial}{\partial y} \left[\rho r^{\kappa} (\nu + \varepsilon_M) \frac{\partial (u^2/2)}{\partial y} + r^{\kappa} (\lambda + \rho \varepsilon_H \overline{C}_p) \frac{\partial T}{\partial y} \right. \\ & + r^{\kappa} \sum_i \left(\rho \varepsilon_D \frac{\partial K_i}{\partial y} - j_i \right) h_i \\ & \left. - \frac{r^{\kappa} R T}{\rho} \sum_i \sum_j \frac{x_j D_i^T}{\mathcal{M}_i \mathcal{D}_{ij}} \left(\frac{j_i}{K_i} - \frac{j_j}{K_j} \right) + r^{\kappa} q_r \right] \end{aligned} \tag{3.3}$$

where, by definition, the total enthalpy $H_T = h + \frac{u^2}{2}$ with $h = \sum_i K_i h_i$ and $h_i = \int_{T^0}^{T} C_{p_i} dT + h_i^0$. λ is the thermal conductivity, ε_H the turbulent eddy conductivity and ε_D the turbulent eddy diffusivity. The mass fraction and mole fraction of the i^{th} species are denoted by K_i and x_i respectively and the diffusional mass flux of that species by j_i. D_i^T is the corresponding multicomponent thermal

diffusion coefficient and $\mathcal{D}_{ij}$ the multicomponent binary diffusion coefficient. The one-dimensional net radiant heat flux to the surface due to absorption and emission is q_r.

Finally, species conservation is given by:

$$\rho u \frac{\partial K_i}{\partial s} + \rho v \frac{\partial K_i}{\partial y} = \frac{1}{r^\kappa} \frac{\partial}{\partial y} \left[r^\kappa \left(\rho \varepsilon_{D_i} \frac{\partial K_i}{\partial y} - j_i \right) \right] + \psi_i \tag{3.4}$$

where ψ_i denotes the rate of mass generation of species i due to chemical reactions.

The diffusional mass flux j_i can be obtained explicitly by approximating the binary diffusion coefficient $\mathcal{D}_{ij}$ by the function $\mathcal{D}_{ij} \approx \frac{\overline{D}(T,P)}{F_i F_j}$, where $\overline{D}$ is a reference diffusion coefficient and F_i is a diffusion factor for species i, and thereafter solving the Stefan-Maxwell equation

$$\frac{\partial x_i}{\partial y} = \sum_j \frac{x_i x_j}{\rho \mathcal{D}_{ij}} \left[\frac{j_j + D_j^T \frac{\partial \ln T}{\partial y}}{K_j} - \frac{j_i + D_i^T \frac{\partial \ln T}{\partial y}}{K_i} \right]. \tag{3.5}$$

The resulting expression for j_i is given by

$$j_i = -\frac{\rho \overline{D} \mu_2}{\mu_1 \mathcal{M}} \left[\frac{\partial Z_i}{\partial y} + (Z_i - K_i) \frac{\partial \mu_4}{\partial y} \right], \tag{3.6}$$

defining

$$\begin{gathered} Z_i \equiv \tfrac{\mathcal{M}_i x_i}{F_i \mu_2}, \\ \mu_1 \equiv \sum_j x_j F_j, \qquad \mu_2 \equiv \sum_j \tfrac{\mathcal{M}_j x_j}{F_j}, \qquad \mu_3 \equiv \sum_i \tfrac{Z_i}{\mathcal{M}_i}, \qquad \mu_4 \equiv \ln\left(\mu_2 T^{c_t}\right), \\ c_t \approx -0.5, \\ \tilde{C}_p \equiv \sum_i Z_i C_{p_i}, \\ \tilde{h} \equiv \sum_i Z_i h_i, \end{gathered} \tag{3.7}$$

Details on the above approximation for $\mathcal{D}_{ij}$ and the derivation of the coefficients listed in (3.7) can be found in Tong *et al.* [1973].

The diffusional heat flux away from the surface can be expressed with the help of (3.7) as

$$\begin{aligned} q_a = -\Bigg\{ & \rho(\varepsilon_M + \nu) \frac{\partial \left(\frac{u^2}{2}\right)}{\partial y} + (\lambda + \rho \varepsilon_H \overline{C}_p) \frac{\partial T}{\partial y} + \rho \varepsilon_D \left(\frac{\partial h}{\partial y} - \overline{C}_p \frac{\partial T}{\partial y} \right) \\ & + \frac{\rho \overline{D} \mu_2}{\mu_1 \mathcal{M}} \left[\frac{\partial \tilde{h}}{\partial y} - \left(\tilde{C}_p + \frac{c_t^2 R}{\mu_1 \mu_2} \right) \frac{\partial T}{\partial y} + c_t R T \frac{\partial \mu_3}{\partial y} + (\tilde{h} - h + c_t R T \mu_3) \frac{\partial \mu_4}{\partial y} \right] \Bigg\}. \end{aligned} \tag{3.8}$$

For computational reasons outlined in Bartlett and Kendall [1967], it is often preferable to rewrite the conservation equations by introducing "elemental" mass fractions rather than "species" mass fractions. In the case of equilibrium chemistry, for example, this effectively reduces the size of the matrix to be inverted in the solution procedure for the system of differential equations describing the problem. Therefore, defining the elemental mass fraction for an element k as

$$\tilde{K}_k = \sum_i \alpha_{ki} K_i, \tag{3.9}$$

and

$$\begin{aligned} \tilde{Z}_k &\equiv \sum_i \alpha_{ki} Z_i, \\ \phi_k &\equiv \sum_i \alpha_{ki} \psi_i, \end{aligned} \tag{3.10}$$

allows the diffusional mass flux to be rewritten as

$$j_k = -\frac{\rho \overline{D} \mu_2}{\mu_1 \mathcal{M}} \left[\frac{\partial \tilde{Z}_k}{\partial y} + \left(\tilde{Z}_k - \tilde{K}_k \right) \frac{\partial \mu_4}{\partial y} \right]. \tag{3.11}$$

The new equations of conservation of mass, momentum, energy and "elemental" species then become

$$\frac{\partial}{\partial s}(\rho u r^\kappa) + \frac{\partial}{\partial y}(\rho v r^\kappa) = 0, \tag{3.12}$$

$$\rho u \frac{\partial u}{\partial s} + \rho v \frac{\partial u}{\partial y} = \frac{1}{r^\kappa} \frac{\partial}{\partial y} \left[\rho r^\kappa (\nu + \varepsilon_M) \frac{\partial u}{\partial y} \right] - \frac{\partial p}{\partial s}, \tag{3.13}$$

$$\rho u \frac{\partial H_T}{\partial s} + \rho v \frac{\partial H_T}{\partial y} = \frac{1}{r^\kappa} \frac{\partial}{\partial y} \left[r^\kappa (-q_a + q_r) \right], \tag{3.14}$$

$$\rho u \frac{\partial \tilde{K}_k}{\partial s} + \rho v \frac{\partial \tilde{K}_k}{\partial y} = \frac{1}{r^\kappa} \frac{\partial}{\partial y} \left[r^\kappa \left(\rho \varepsilon_{D_k} \frac{\partial \tilde{K}_k}{\partial y} - j_k \right) \right] + \phi_k, \tag{3.15}$$

where, by definition, $\phi_k \equiv \sum_i \alpha_{ki} \psi_i$. In the case of equilibrium chemistry $\phi_k = 0$ since there is no production whereas for nonequilibrium chemistry

$$\begin{aligned} \alpha_{ki} &= 0\,, \quad k \neq i \\ \alpha_{ki} &= 1\,, \quad k = i \end{aligned} \tag{3.16}$$

Finally, to complete the formulation of the problem, expressions for the equation of state and the transport properties must be provided. This is taken care of within BLIMPK with standard mixture formulas for viscosity (Buddenberg-Wilke) and thermal conductivity (Mason-Saxena), taking into account the exact composition of the gas at the points of interest. Also needed are the equilib-

rium or nonequilibrium relations. Tables D.1 and D.2 in Appendix D summarize the more important reactions for flows involving air and carbon dioxide respectively (Chen *et al.* [1993], Park *et al.* [1994]).

As far as closure of the turbulence parameters is concerned, BLIMPK relies on different mixing length correlations, the boundary layer being generally split into a wall region and a wake region. Details can be found in Evans [1975] where the more successful of the three models included in BLIMPK seems to be the one derived by Cebeci and Smith which accounts for a variable turbulent Prandtl number. The other two models are attributed to Kendall and to Bushnell. The user must specify the station along the body where the code is to switch from fully laminar to fully turbulent. This can also be accomplished by specifying a momentum thickness beyond which the switch is to take place. BLIMPK accounts for a buffer-transition zone between the last laminar station and the first turbulent one. This manifests itself by a slight overshoot in the initial turbulent heat transfer.

3.1.2 Transformation

Once all equations needed to close the problem have been identified - conservation of mass, momentum, energy and species or elements, state, viscosity, conductivity, chemistry and mixing length - one can go on to solve the problem by appropriately discretizing them. It is however quite often in the interest of speed, accuracy and simplicity to transform these equations from the original (s,y) coordinate system to a different system. In the case of the compressible boundary layer equations under arbitrary boundary conditions, one usually resorts to one form or another of the Levy-Lees transformation (Lees [1956]).

The Levy-Lees transformation from the (s,y) coordinate system to (ξ,η) is given by the following pair of equations

$$\begin{aligned} \xi &= \int_o^s \rho_1 u_1 \mu_1 r_o^{2\kappa} ds, \\ \eta &= \frac{r_o^\kappa u_1}{\sqrt{2\xi}} \int_o^y \rho dy. \end{aligned} \tag{3.17}$$

An implicitly determined stretching parameter $\alpha_H(\xi)$ is added within the BLIMPK formulation to keep the thickness of the boundary layer constant in the $\overline{\eta}$ direction as the solution marches in the ξ direction. The new set of coordinates $(\overline{\xi},\overline{\eta})$ is therefore given by

$$\begin{aligned} \overline{\xi} &= \xi, \\ \overline{\eta} &= \frac{\eta}{\alpha_H}. \end{aligned} \tag{3.18}$$

The additional equation now required by the introduction of the new parameter α_H is obtained by

fixing the u component of velocity to c at a given $\overline{\eta}_c$ node, i.e.,

$$f'\Big|_{\overline{\eta}_c} = cf'\Big|_{\overline{\eta}_{edge}}, \tag{3.19}$$

where f is the dimensionless stream function given by

$$f - f_w = \int_0^{\eta} \frac{u}{u_1} d\eta = \alpha_H \int_0^{\overline{\eta}} \frac{u}{u_1} d\overline{\eta}, \tag{3.20}$$

and, by definition,

$$f' = \frac{\partial f}{\partial \overline{\eta}} = \alpha_H \frac{u}{u_1}. \tag{3.21}$$

Finally, if one takes r to be a function of y, as would be the case for thin axisymmetric bodies where the boundary layer thickness δ is comparable to the body radius r_o, the $(\overline{\xi}, \overline{\eta})$ system can be transformed to a $(\hat{\xi},\hat{\eta})$ system such that

$$\begin{aligned} \hat{\xi} &= \int_0^s \rho_1 u_1 \mu_1 r_o^{2\kappa} ds, \\ \hat{\eta} &= \frac{u_1}{\alpha_H \sqrt{2\hat{\xi}}} \int_0^y \rho r^{\kappa} dy, \end{aligned} \tag{3.22}$$

with now, dropping the hats,

$$\begin{aligned} f - f_w &= \alpha_H \int_0^{\eta} \frac{u}{u_1} d\eta, \\ f_w &= -\frac{1}{\sqrt{2\xi}} \int_0^{\xi} \frac{\rho_w v_w}{\rho_1 u_1 \mu_1 r_o^{\kappa}} d\xi. \end{aligned} \tag{3.23}$$

Since the (s,y) derivatives can now be rewritten in terms of (ξ,η) derivatives using

$$\begin{aligned} \frac{\partial}{\partial s}\Big|_y &= \frac{\partial}{\partial \xi}\Big|_\eta \frac{\partial \xi}{\partial s}\Big|_y + \frac{\partial}{\partial \eta}\Big|_\xi \frac{\partial \eta}{\partial s}\Big|_y, \\ \frac{\partial}{\partial y}\Big|_s &= \frac{\partial}{\partial \xi}\Big|_\eta \frac{\partial \xi}{\partial y}\Big|_s + \frac{\partial}{\partial \eta}\Big|_\xi \frac{\partial \eta}{\partial y}\Big|_s, \end{aligned} \tag{3.24}$$

the transformed equations for conservation of momentum, energy and elements become

$$ff'' + \left[\frac{C\left(1 + \frac{\varepsilon_M}{\nu}\right)}{\alpha_H} f''\right]' + \beta\left(\alpha_H^2 \frac{\rho_1}{\rho} - f'^2\right) = 2\left(f' \frac{\partial f'}{\partial \ln \xi} - f'^2 \frac{\partial \ln \alpha_H}{\partial \ln \xi} - f'' \frac{\partial f}{\partial \ln \xi}\right), \tag{3.25}$$

$$fH_T' + \left(-q_a^* + q_r^*\right)' = 2\left(f' \frac{\partial H_T}{\partial \ln \xi} - H_T' \frac{\partial f}{\partial \ln \xi}\right), \tag{3.26}$$

$$f\tilde{K}_k' + \left(\frac{\tilde{\varepsilon}_M}{\alpha_H Sc_t} \tilde{K}_k' - j_k^*\right)' + \left(\frac{\phi_k}{\rho}\right)\left(\frac{\rho_e \mu_e \alpha_H}{\alpha^{*2}}\right) = 2\left(f' \frac{\partial \tilde{K}_k'}{\partial \ln \xi} - \tilde{K}_k' \frac{\partial f}{\partial \ln \xi}\right), \tag{3.27}$$

assuming $p = p(\xi)$ only and where the $(\,)^*$ refers to quantities that have been appropriately nondimensionalized. The streamwise pressure gradient parameter β and the Chapman-Rubesin parameter C are respectively defined as

$$\beta \equiv 2\frac{\partial \ln u_1}{\partial \ln \xi}, \tag{3.28}$$

$$C \equiv \frac{\rho\mu}{\rho_1\mu_1}. \tag{3.29}$$

It should be noted that after the coordinate transformation, the equation of mass conservation is identically satisfied. Furthermore, an interesting consequence of similarity is that along with vanishing β, the right hand sides of all the equations listed above vanish as well. The system is therefore reduced to a system of ordinary differential equations.

3.1.3 Discretization

The first step in implementing the integral matrix procedure is determining the size of the grid to be used, in particular the number of nodal points to be considered across the boundary layer (η - direction) and along the body (ξ - direction). The number of ξ points and the spacing in between depends on the geometry and the edge properties, since a converged solution is output for each one of these streamwise stations once the equations have been solved across the boundary layer strip.

The number of η points is the controlling factor for speed and accuracy of a solution. The main idea behind the integral matrix procedure is to minimize the number of transverse nodes needed to obtain an accurate solution. This is achieved by spline fitting the primary dependent variables - f, H_T and $\tilde{K}_k$ - and their derivatives with respect to η in between these nodes with Taylor series. Examples with as few as seven points across the boundary are shown in Bartlett and Kendall [1967] to be accurate to several significant figures and ones with eleven points across the boundary layer to be almost indistinguishable from the exact solution. The maximum number of η points allowed by BLIMPK is accordingly 15 and the code allows the user to redistribute the nodes at different ξ stations to account for varying streamwise conditions such as transition to turbulence, blowing, suction, etc. which might strongly affect the overall shape of the boundary layer.

Assuming the boundary layer is resolved by N points at distances η_i and that $p(\eta)$ is one of the primary variables - f, H_T, $\tilde{K}_k$ - continuous along with its derivatives around $\eta = \eta_i$, one can write its Taylor series expansion as

$$p_{i+1} = p_i + p_i'\delta\eta + p_i''\frac{\delta\eta^2}{2!} + p_i'''\frac{\delta\eta^3}{3!} + p_i^{iv}\frac{\delta\eta^4}{4!} + \ldots \tag{3.30}$$

where

$$\delta\eta \;=\; \eta_{i+1} \;-\; \eta_i. \tag{3.31}$$

A quick glance at Equations (3.25)-(3.27) reveals that the highest derivatives to appear are f_i''', H_{T_i}'' and $\tilde{K}_{k_i}''$ so that one could truncate the series at the next highest derivative and assume it remains constant between η_i and η_{i+1}. The resulting set of linear equations for the primary dependent variables and their derivatives is therefore

$$-f_{i+1} \;+\; f_i \;+\; f_i'\delta\eta \;+\; f_i''\frac{\delta\eta^2}{2} \;+\; f_i'''\frac{\delta\eta^3}{8} \;+\; f_{i+1}'''\frac{\delta\eta^3}{24} \;=\; 0, \tag{3.32}$$

$$-p_{i+1} \;+\; p_i \;+\; p_i'\delta\eta \;+\; p_i''\frac{\delta\eta^2}{3} \;+\; p_{i+1}''\frac{\delta\eta^2}{6} \;=\; 0, \tag{3.33}$$

$$-p_{i+1}' \;+\; p_i' \;+\; p_i''\frac{\delta\eta}{2} \;+\; p_{i+1}''\frac{\delta\eta}{2} \;=\; 0, \tag{3.34}$$

where f_i', H_{T_i} and $\tilde{K}_{k_i}$ for all k elements are substituted for p_i. It should be noted that $f_i' \;=\; \alpha_H\frac{u}{u_1}$ is used instead of f since it is the actual velocity profile and not the stream function that is of interest. The total number of equations , when written for each set of nodes is (N-1)[5+2(k-1)] and the number of unknowns - f_n, f_n', f_n'', f_n''', α_H, H_{T_n}, H_{T_n}', H_{T_n}'', $\tilde{K}_{k_n}$, $\tilde{K}_{k_n}'$, $\tilde{K}_{k_n}''$ - comes up to N(4+3k)+1. The remaining equations come from the actual physical differential equations as well as the specific boundary conditions and, the variables being only functions of $\delta\eta$, the system needs to be solved only once per strip, i.e., the matrix of coefficients need be inverted but once.

In the ξ direction standard finite difference expressions are used to discretize the derivatives that appear on the right hand side of Equations (3.25)-(3.27). It should be noted again that if the solutions were self-similar, this step would not be necessary since the right hand side would vanish. Two- and three-point difference formulas are found to be sufficient (Bartlett and Kendall [1967]). This gives

$$2\left[\frac{d()}{d(\ln\xi)}\right]_\ell \;=\; d_o()_\ell \;+\; d_1()_{\ell-1} \;+\; d_2()_{\ell-2}, \tag{3.35}$$

where the subscript ℓ refers to the ℓ^{th} streamwise position and where, for a two-point difference formulation,

$$d_o \;=\; \frac{2}{\ell\Delta_{\ell-1}}, \quad d_1 \;=\; -\frac{2}{\ell\Delta_{\ell-1}}, \quad d_2 \;=\; 0 \tag{3.36}$$

and for a three-point difference formulation,

$$d_o \;=\; 2\,\frac{\ell\Delta_{\ell-1} \;+\; \ell\Delta_{\ell-2}}{\ell\Delta_{\ell-1}\;\ell\Delta_{\ell-2}}, \quad d_1 \;=\; -2\,\frac{\ell\Delta_{\ell-2}}{\ell\Delta_{\ell-1}\;\ell_{-1}\Delta_{\ell-2}}, \quad d_2 \;=\; 2\,\frac{\ell\Delta_{\ell-1}}{\ell\Delta_{\ell-2}\;\ell_{-1}\Delta_{\ell-2}} \tag{3.37}$$

with

$$_{\ell}\Delta_{\ell-1} \;=\; \ln\xi_{\ell} \;-\; \ln\xi_{\ell-1} \;=\; \ln\left(\frac{\xi_{\ell}}{\xi_{\ell-1}}\right). \tag{3.38}$$

Choosing either formulation is left up to the BLIMPK user as an option in the input file since it may depend on the particular problem being solved. However, it should be noted that for most problems, streamwise changes are very smooth and a the two-point expression is usually sufficient.

3.1.4 Integral matrix procedure

At this point, one could solve the linear Taylor series listed above along with the boundary layer equations, boundary conditions and, finally, the equation defining α_H to close the problem. However, this is not very practical since the boundary layer equations are not linear. In particular, the terms involving derivatives in η in the energy and element equations need to be simplified. The problem reduces to one of linearizing all of the equations so that the system describing the entire problem is linear. To achieve this, the boundary layer equations must be integrated across the transverse η strips. This is equivalent to applying a square wave weighting function on top of the boundary layer taking on the value of unity between η_i and η_{i+1} and vanishing everywhere else.

The momentum equation (3.25) would therefore give, as an example,

$$\begin{aligned}
\int_{i-1}^{i} ff''d\eta \;+\; &\left[\frac{(C \,+\, \tilde{\varepsilon}_M)}{\alpha_H} f''\right]_{i-1}^{i} \;+\; \beta\alpha_H^2 \int_{i-1}^{i} \frac{\rho_1}{\rho} d\eta \;-\; \beta \int_{i-1}^{i} f'^2 d\eta \\
&= \int_{i-1}^{i} f'(d_o f' \;+\; d_1 f'_{\ell-1} \;+\; d_2 f'_{\ell-2}) d\eta \;-\; \int_{i-1}^{i} f'^2 \left[d_o \ln\alpha_H \right. \\
&+\; \left. d_1(\ln\alpha_H)_{\ell-1} \;+\; d_2(\ln\alpha_H)_{\ell-2}\right] d\eta \;-\; \int_{i-1}^{i} f''(d_o f \\
&+\; d_1 f_{\ell-1} \;+\; d_2 f_{\ell-2}) d\eta,
\end{aligned} \tag{3.39}$$

where the Taylor series described above can then be substituted into the integrals. The end result, after substantial algebra and manipulation, is the desired linear system of equations which can then be solved by standard matrix techniques. The complete sets of linearized equations can be found in Tong *et al.* [1973] and the derivation of each one of these in Bartlett and Kendall [1967].

The technique used by BLIMPK to solve the system of equations is a simple Newton-Raphson technique, adapted to account for the fact that the matrix of coefficients is somewhat sparse in certain areas. This procedure is an iterative one which consists in solving for corrections to an approximate set of solutions and progressively letting the error approach some limit depending on the accuracy required. Once a solution is found within acceptable error bounds, the calculations proceed to the next downstream ξ station after the solution is dumped to an output file.

3.2 BLIMPK simulations of cone experiments

The geometry input for the simulations of the T5 experiments consists of a sharp 5° half-angle cone. No calculations were performed including bluntness. The streamwise nodal spacing corresponds roughly to the locations of the thermocouples. The nodal distribution across the boundary layer is chosen to provide sufficient resolution close to the wall where surface chemistry and maximum temperature effects might be important. If the turbulent switch is turned on, the nodes are redistributed accordingly. The flow conditions are input in the form of stagnation enthalpy, stagnation pressure (behind the shock), and boundary layer edge pressure and composition. Profiles of all physical and chemical properties of the flow are output at each streamwise station: velocity, temperature, viscosity, species mole fractions, etc.

Three types of chemistry models were computed for each run. First, the chemistry was assumed to be frozen and then in nonequilibrium. For the latter case, both catalytic and noncatalytic walls were investigated. Gas phase and surface reactions considered are listed in Appendix D along with the appropriate references. Of course, the numerical and experimental data must be reduced into a suitable nondimensional form to allow for direct comparisons.

Chapter 4 Laminar and Turbulent Heat Flux

In order to be able to compare the experimentally and numerically obtained heat transfer distributions, it is necessary to reduce the data to a suitable nondimensional form. The heat transfer rate is typically normalized into a Stanton number and the distance along the cone's surface into a Reynolds number. By definition, the Reynolds number is given by the following expression:

$$Re = \frac{\rho_e u_e x}{\mu_e} \tag{4.1}$$

where x is the distance from the cone tip along the centerline. ρ_e, u_e and μ_e are fluid properties usually evaluated at the edge of the boundary layer. However, as will be discussed in later sections, it may be better to evaluate these quantities at points more representative of the boundary layer's internal state than the edge. The Stanton number is given by the following expression:

$$St = \frac{\dot{q}(x)}{\rho_e u_e [h_0 - \frac{1}{2}u_e^2(1-r) - C_p T_w]} \tag{4.2}$$

where $\dot{q}$ is the heat transfer rate, h_0 the stagnation enthalpy, r the recovery factor, and T_w the wall temperature. For laminar flows, $r_{lam} = \sqrt{Pr}$ and for turbulent flows $r_{turb} \approx \sqrt[3]{Pr}$ where Pr is the Prandtl number (Figure 4.1). Pr is assumed to be constant, a fair approximation for most conditions of interest. Expressions for the Stanton number - Reynolds number relationship can be obtained for both laminar and turbulent boundary layers and are discussed below.

4.1 Laminar theory

For similar boundary layers at sufficiently high speeds, regardless of whether the flow is laminar or turbulent, the Reynolds analogy postulates relating the Stanton number St to the skin friction coefficient C_f with the following expression (White [1991]):

$$St \approx \frac{1}{2} C_f Pr^{-2/3}. \tag{4.3}$$

Relating the skin friction coefficient to the Reynolds number would therefore give the desired expression for the St - Re relationship.

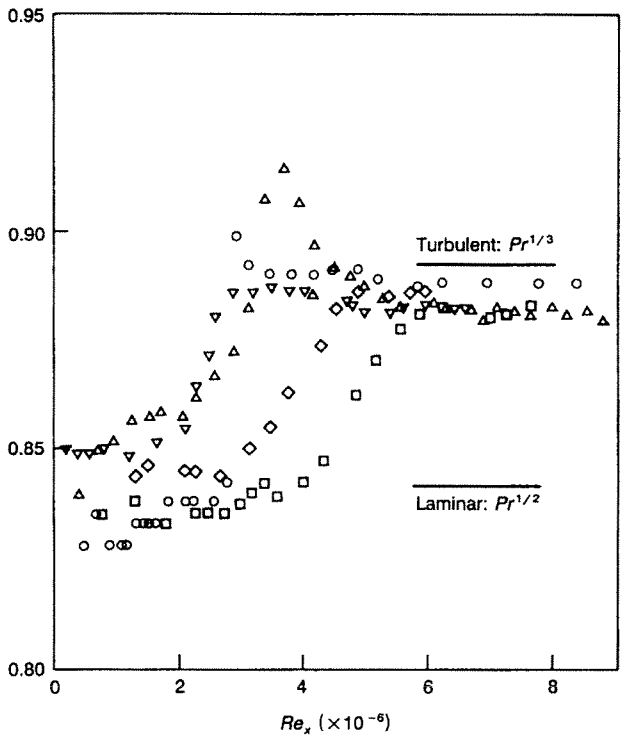

Figure 4.1: Recovery factor on cones in air (Data from Mack [1954] at Mach numbers from 1.2 to 6.0 plotted by White [1991])

The skin friction coefficient is obtained by nondimensionalizing the wall shear stress as follows:

$$C_f(x) = \frac{\tau_w(x)}{\frac{1}{2}\rho_e U_e^2}. \tag{4.4}$$

In the case of an incompressible two-dimensional boundary layer in a zero pressure gradient, one can numerically solve for the classic "Blasius solution" for a flat plate and obtain the corresponding incompressible skin friction coefficient

$$C_{f_{inc}}(x) = \frac{0.664}{\sqrt{Re_x}}, \tag{4.5}$$

where Re_x is the Reynolds number based on the distance x from the leading edge of flat plate. If compressibility effects are included, a correction factor must be introduced resulting in a now approximate expression for the skin friction coefficient given by

$$C_{f_{comp}}(x) \approx \frac{0.664}{\sqrt{Re_x}}\sqrt{C_w}, \tag{4.6}$$

where $C_w = \rho_w \mu_w / \rho_e \mu_e$ is the Chapman-Rubesin parameter evaluated at the wall. This expression,

although quite good for adiabatic walls, is unfortunately not very accurate for hot or cold walls (White [1991]). This is remedied by introducing the reference temperature T^* given empirically by Eckert [1955] as

$$\frac{T^*}{T_e} \approx 0.5 + 0.039\,M_e^2 + 0.5\frac{T_w}{T_e} \tag{4.7}$$

and, using $C^* = \rho^*\mu^*/\rho_e\mu_e$, to get

$$C_{f_{comp}}(x) \approx \frac{0.664}{\sqrt{Re_x}}\sqrt{C^*}. \tag{4.8}$$

This expression is more reasonably accurate, regardless of the wall conditions. It should be noted that Eckert's expression for T^* was obtained empirically and is the most widespread. There have been other correlations that are equally accurate. Dorrance [1962], however, showed that the reference temperature can be derived from similarity considerations resulting in a more general expression

$$\frac{T^*}{T_e} = \frac{1}{2} + \frac{\gamma-1}{2}\frac{\sqrt{Pr}}{6}M_e^2 + \frac{1}{2}\frac{T_w}{T_e}. \tag{4.9}$$

Finally, one must account for the axisymmetric nature of the flow. This is done by applying the Lees-Illingworth transformation (similar to the transformation outlined in Section 3.2.2) which results in

$$C_{f,cone} = \sqrt{3}\,C_{f,plate}, \tag{4.10}$$

and gives the desired St - Re relationship as

$$St \approx \frac{\sqrt{3}}{2}C_f Pr^{-2/3} \approx \frac{0.664\sqrt{3}}{2}\frac{\sqrt{C^*}}{Pr^{2/3}\sqrt{Re}}. \tag{4.11}$$

4.2 Turbulent models

The same approach followed to obtain the laminar St - Re relationship can be followed for the turbulent case. Starting with Equation (4.3), one therefore seeks a way to express the skin friction coefficient in terms of the Reynolds number. Obviously, for turbulent flows, this cannot be done exactly. However, a very good approximation for incompressible turbulent skin friction on a flat plate is given by the following expression:

$$C_{f_{inc}} \approx \frac{0.455}{ln^2(0.06\,Re_x)}. \tag{4.12}$$

Its derivation is discussed in White [1991] and the problem now reduces to one of finding the best way to introduce a compressibility correction factor, just as the Chapman-Rubesin parameter was

introduced in the laminar equations above. However, this can only be done if the structure of the compressible turbulent boundary layer of interest does not differ by much, qualitatively, from that of the incompressible one. According to a hypothesis put forward by Morkovin [1962], this holds only if density fluctuations are small. This translates into requiring the fluctuating Mach number M' to remain small as well, which is true for most boundary layers up to around Mach numbers of 5 (Figure 4.2). If M' were to exceed unity, local shocklets could significantly alter the boundary layer's structure.

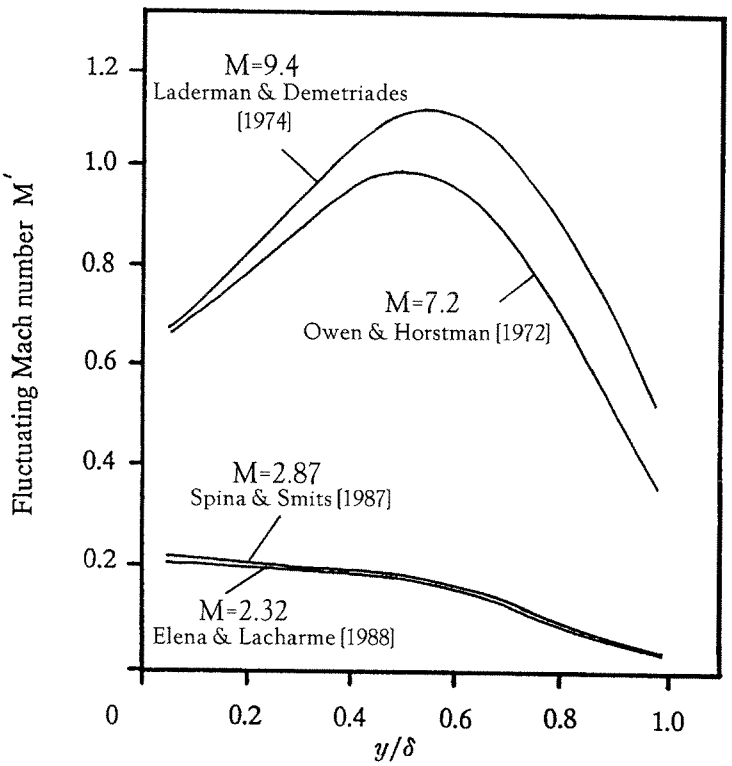

Figure 4.2: Fluctuating Mach numbers distributions (Spina *et al.* [1994])

Assuming Morkovin's hypothesis holds, one then introduces two correction factors giving

$$C_{f_{comp}} = \frac{1}{F_c} C_{f_{inc}}(Re_x F_{Re}) \approx \frac{1}{F_c} \frac{0.455}{ln^2(0.06\, Re_x F_{Re})}, \tag{4.13}$$

where F_{Re} is a factor "stretching" the Reynolds number within the incompressible equation (4.12) and F_c a factor correcting the resulting skin friction. Two formulations for F_{Re} and F_c are presented below. The first one is by van Driest [1956] and is by far the most popular, the second is by White and Christoph [1972] and offers slightly better results for cold walls. It should be noted, however,

that neither one of these formulations for the skin friction is as accurate as the corresponding ones for incompressible flows and considerable work is still going on to gain a better understanding of compressible turbulent boundary layers (Dussauge *et al.* [1995]).

In both the van Driest and the White and Christoph models, F_c is given by the following expression:

$$F_c = \frac{T_{aw}/T_e - 1}{(\sin^{-1} A + \sin^{-1} B)^2}, \tag{4.14}$$

where T_e is the boundary layer edge temperature and T_{aw} is the adiabatic wall temperature defined as

$$\frac{T_{aw}}{T_e} = 1 + r_{turb}\frac{\gamma - 1}{2}M_e^2. \tag{4.15}$$

A and B are given by

$$\begin{aligned} A &= \frac{2a^2 - b}{\sqrt{b^2 + 4a^2}}, \\ B &= \frac{b}{\sqrt{b^2 + 4a^2}}, \end{aligned} \tag{4.16}$$

as functions of the parameters a and b defined as

$$\begin{aligned} a &= \sqrt{\frac{\gamma - 1}{2}M_e^2\frac{T_e}{T_w}}, \\ b &= \frac{T_{aw}}{T_w} - 1. \end{aligned} \tag{4.17}$$

The difference in the two models lies in the formulation of the Reynolds number stretching factor F_{Re}. In van Driest's model, often referred in the literature as "van Driest II", it is given simply by

$$F_{Re} = \frac{1}{F_c}\frac{\mu_e}{\mu_w}, \tag{4.18}$$

whereas according to White and Christoph's model, the preferred form is

$$F_{Re} = \frac{1}{\sqrt{F_c}}\frac{\mu_e}{\mu_w}\sqrt{\frac{T_e}{T_w}}. \tag{4.19}$$

To complete the problem one must again account for the fact that the flow is in actuality axisymmetric and that these equations were derived for two dimensional flat plate flows. In laminar flow this resulted in the heat transfer being higher by an exact factor of $\sqrt{3}$. However, the corresponding transformations for turbulent conical flow are only approximate and yield a factor of roughly 1.10 (van Driest [1952]).

Chapter 5 Enthalpy Effects on Transition

Within the performance envelope of the T5 hypervelocity shock tunnel, Reynolds numbers from a few million to as much as twenty million can be attained over the model surface. This makes the facility well suited to study boundary layer transition and, in particular, enthalpy effects on boundary layer transition. Densely spaced thermocouples can accurately capture the region over which the heat transfer smoothly changes from its initial laminar level to the higher turbulent state.

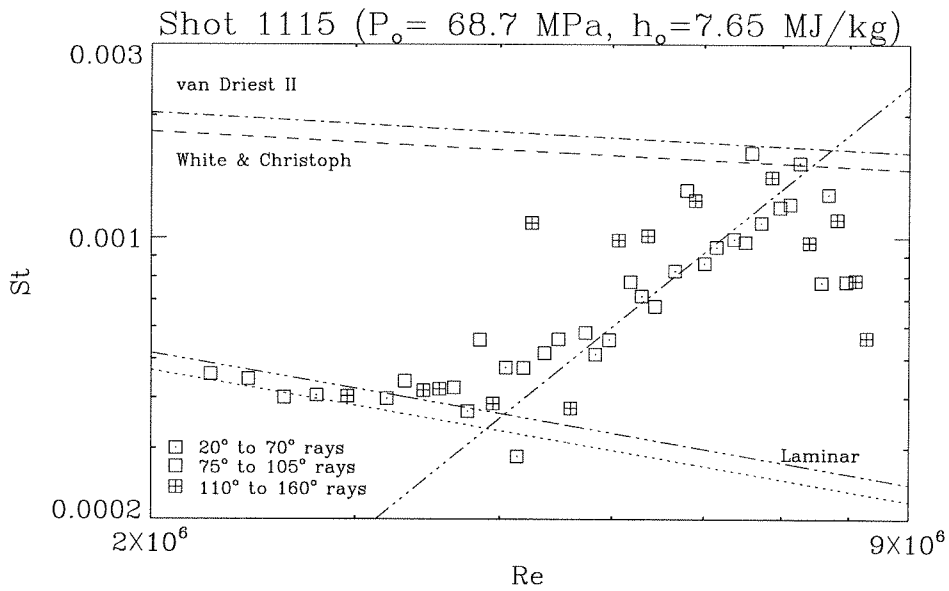

Figure 5.1: Typical heat transfer traces and fits for a transitional boundary layer in air. The dotted line represents the theoretical laminar limit with frozen chemistry. The dashed and the dash-dot line represent two different turbulence models, also with frozen chemistry. The two other lines are fits of laminar and transitional experimental data. Note the slight offset of the laminar fit from the theoretical line probably due to the nonequilibrium processes inside the boundary layer. Measurements on the cone are separated into three azimuthally separated regions to bring out possible flow asymmetries over different sections of the cone. The drop-off at the end is due to a wave emanating from the nozzle end.

A typical heat transfer distribution for a shot with a transitional boundary layer is illustrated in Figure 5.1. A line following the theoretical $Re^{-\frac{1}{2}}$ behavior is fitted through the points corresponding to thermocouples in the laminar part of the boundary layer. Similarly, a positive-slope line is fitted through the points covering the transition zone, from the last laminar point to the first turbulent

point. Both fits are shown in Figure 5.1 and the point of intersection is defined as being the transition Reynolds number, Re_{tr}. Also shown in Figure 5.1 are theoretical predictions of both the laminar and turbulent heat flux with frozen chemistry. These lines serve as an approximate gage for deciding which ones of the experimental data points should be included in the laminar and transitional fits.

Experimental transition data must be complemented with stability analysis in order to convincingly support any conclusions that might be inferred from the observations. A boundary layer can take more than one road to get from its initially laminar state to a final fully turbulent state. A number of different wave-like instabilities are known to cause transition: the Tollmien-Schlichting mode at the lower frequencies and wavelengths around six times the boundary layer thickness δ and the Mack modes at much higher frequencies with wavelengths around 2δ. A stability experiment which tracks the growth and amplification of these instabilities would be required to complete the understanding of the transition phenomena. Of course, as an extreme case, transition can be bypassed altogether with the boundary layer going directly from laminar to turbulent.

Transition by itself is intricately tied to the facility in which it was obtained. Each tunnel generates a very specific "noise" spectrum which can affect the growth of the boundary layer instabilities. Ideally disturbances should be kept to a minimum to recreate flight conditions as accurately as possible and this is best achieved in a "quiet" tunnel albeit never perfectly. At present, no information has been obtained about the noise content of the freestream in the T5 shock tunnel where the following transition results were obtained. Theoretical results indicate that in a perfect gas the most unstable mode at the T5 freestream Mach number around 5 is the Mack mode. Flow visualization, however, suggests otherwise as was observed in resonantly enhanced shadowgraphs by Germain [1994] where waves corresponding to the Tollmien-Schlichting frequency can be seen. This evidence, however, is quite weak and recent computations (Seipp [1997]) suggest that the second mode is the most unstable at these conditions.

All transition data shown in the following sections of this chapter are tabulated in Appendices C.1 through C.7 at the end. These tables include reservoir pressures and enthalpies for each shot, as well as key flow parameters used to normalize the transition locations into the appropriate Reynolds numbers.

5.1 Previous experiments in T5

Previous transition experiments in T5 were actually part of a larger exploratory study including laminar and turbulent boundary layers (Germain [1994]). Results were obtained for a variety of

enthalpies and pressures ranging from the perfect gas regime to conditions where various dissociation and recombination real-gas effects occur. The test gases used consisted mostly of air and nitrogen but a few shots were carried out with carbon dioxide and helium as well.

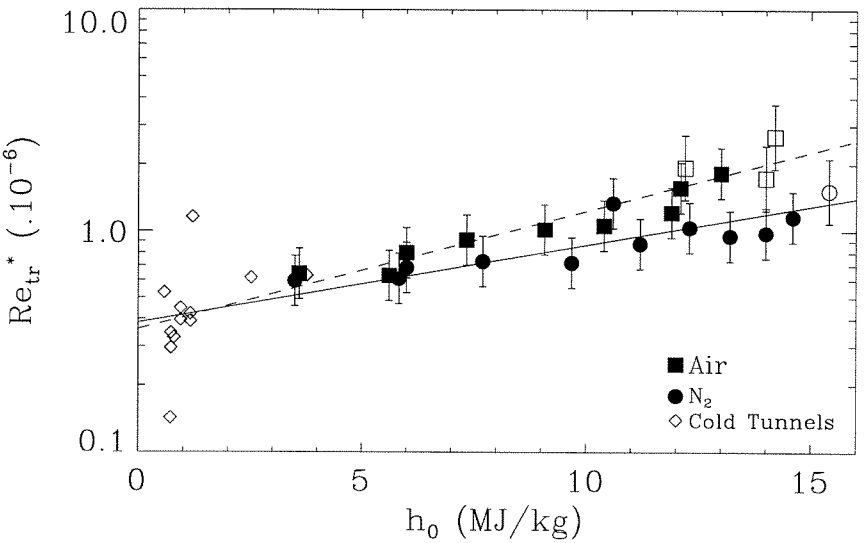

Figure 5.2: Transition Reynolds number evaluated at reference conditions (Germain and Hornung [1997]). Open Symbols correspond to runs where the flow was almost fully laminar with a hint of transition. Error bars are approximate errors made when evaluating Re^*_{tr}. Lines are least square fits of the air and nitrogen data. Cold tunnel data are from DiCristina [1970] and Demetriades [1977].

It was found that the transition data were correlated by plotting the transition Reynolds number evaluated at the reference condition

$$Re^*_{tr} = \frac{\rho^* u_e x_{tr}}{\mu^*}, \tag{5.1}$$

rather than the transition Reynolds number evaluated at the edge condition

$$Re_{tr} = \frac{\rho_e u_e x_{tr}}{\mu_e}. \tag{5.2}$$

This is illustrated in Figure 5.2 above. For the sake of comparison, and to illustrate the range of enthalpies covered by the T5 experiments, older boundary layer transition data from "cold" hypersonic tunnels are shown on the plot as well. The reservoir enthalpy is seen to have a stabilizing effect: the higher the enthalpy h_0, the higher the transition Reynolds number Re^*_{tr}. It is not known if this effect persists at higher enthalpies where the model is too short for transition to be observed. Key enthalpies of reaction involved in these flows must be kept in mind, such as O_2 dissociation at

15.6 MJ/kg and N_2 dissociation at 33.7 MJ/kg. Neither gas is fully dissociated at the upper limit, around 15 MJ/kg, where transition is observable in T5 and perhaps the stabilizing effect tapers off at such conditions.

Another observation of note is the fact that the measurement points for air fall on a steeper line than the points for nitrogen. In fact, isolated tests with carbon dioxide - a low dissociation energy gas - and with helium - an inert gas - hint to a more rapid stabilization with decreasing dissociation energy. This is shown in Figure 5.3 below.

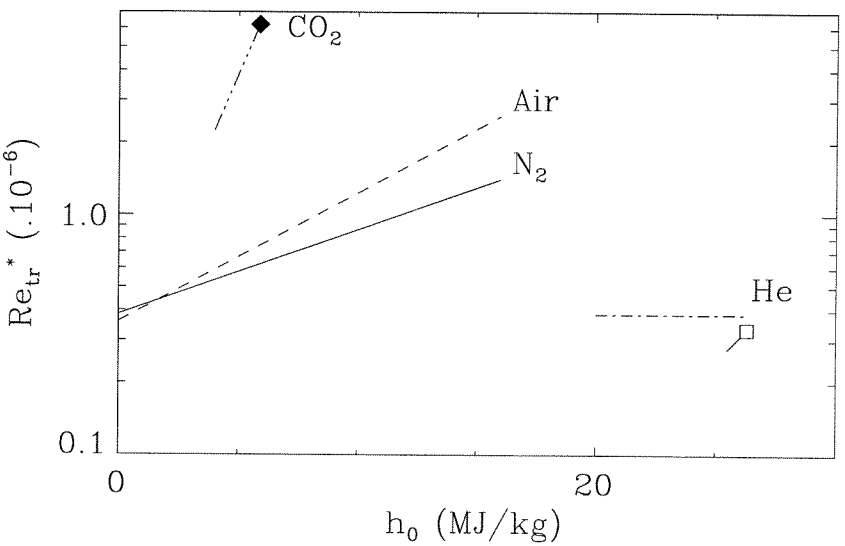

Figure 5.3: Transition Reynolds number evaluated at reference conditions for all gases (Germain [1994])

What characteristic specific energy of the gas determines the h_0 dependence, however, remains to be answered. Further tests should therefore include points at higher enthalpies and, more realistically within current capabilities, runs with gases of different dissociation energies. This would confirm whether the stabilizing effect is indeed more pronounced in gases that are more easily dissociable than air or nitrogen. Carbon dioxide is one example, as illustrated above in Figure 5.3, since it has a low dissociation energy. At the other extreme, operating the tunnel with an inert gas such as helium is not quite suitable for accurate measurements over a large range of conditions. The nozzle expanding the flow over the model would have to operate severely off-design.

5.2 Carbon dioxide flows

The boundary layer transition results plotted in Figures 5.2 and 5.3 indicate both a stabilizing trend with reservoir enthalpy and a decrease in the stabilizing rate with increasing dissociation energy of the test gas. Extending the runs to include transition measurements over as wide a range of carbon dioxide flows as possible would therefore further test these observations and was the primary goal of the new series of experiments in T5 described hereafter.

Carbon dioxide exhibits two properties key to confirming some of the observations made by Germain [1994]. The first of these is that CO_2 dissociates at very low enthalpies compared to both air and certainly nitrogen, giving CO and O. Any stabilizing effect due to dissociation would therefore appear much earlier and at a higher rate with respect to increasing enthalpy. The second property is that the CO obtained will not dissociate further within the enthalpy range studied. It is therefore possible to obtain large levels of CO_2 dissociation before CO begins to dissociate. One might then expect the stabilizing effect to saturate as h_0 is increased.

A total of 35 new shots were performed with carbon dioxide. Reservoir pressures were varied from 40 MPa to 95 MPa and reservoir enthalpies from 3 MJ/kg to 10 MJ/kg. Whereas the air and nitrogen data obtained in previous tests were carried out to study the boundary layer in its different states, the carbon dioxide shots had for primary goal to seek out conditions where transition would occur. Nevertheless, in some cases, fully laminar or turbulent flows were obtained. Results of the laminar heat flux observations are discussed later in Chapter 7. It should be noted that although similar tunnel parameters (initial shock tube pressure, driver gas pressure, and secondary reservoir pressure) were used for both the air/nitrogen tests and the carbon dioxide tests, the range of enthalpies covered in the latter case was lower because the dissociative real-gas effects of interest occur at lower enthalpy in CO_2.

The measured transition Reynolds numbers Re_{tr}, evaluated by normalizing the transition location by the boundary layer edge properties, are plotted versus the reservoir enthalpy h_0 in Figure 5.4 below. Alongside the new carbon dioxide data are plotted the older results for air and nitrogen. As a side note, it should be mentioned that several new air shots were carried out parallel to the carbon dioxide experiments but are omitted for the sake of clarity, the trend they follow being already quite well illustrated by the older data. The transition measurements corresponding to these new air runs are, however, plotted in the following chapter where only air is considered and all data are listed in Appendices C.1 through C.7 at the end.

As expected, there are no distinctive features separating the different gases in Figure 5.4. In particular, there does not seem to be any visible trend with reservoir enthalpy. The carbon dioxide Reynolds numbers do appear to be slightly higher for the most part but there is nevertheless an overlap with some of the air and nitrogen data. The fact that all the carbon dioxide points are clustered below 10 MJ/kg is simply due to the fact that transition is not measurable above that enthalpy level, the cone being too short to allow the flow to proceed beyond its initial laminar state.

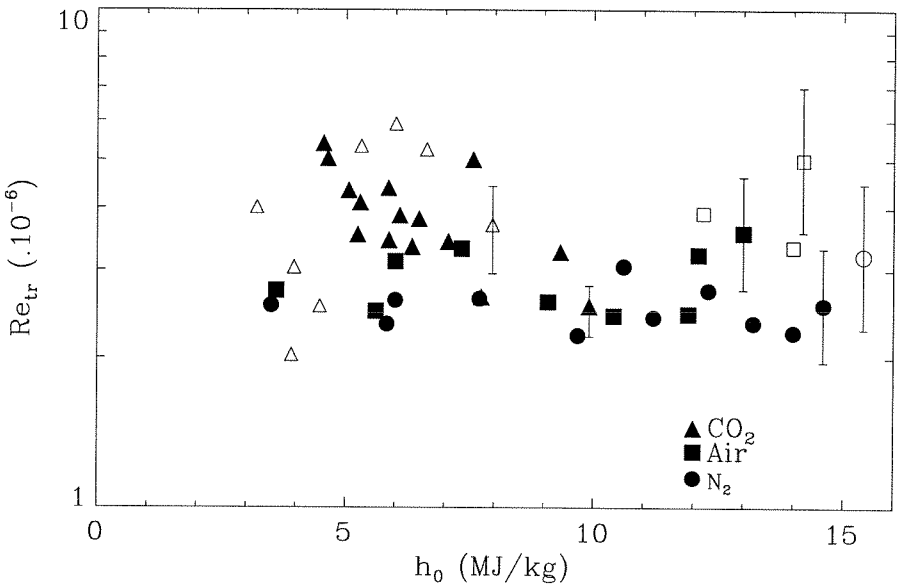

Figure 5.4: Transition Reynolds number correlation with stagnation enthalpy. Open symbols indicate flows that were almost fully laminar with a hint of transition. Error bars are approximate measures of the error in Re_{tr}

Again, however, use of the reference temperature concept helps bring out the relevant features. Normalizing the transition location with the reference density and viscosity, but still keeping the edge velocity, one can look at the same data with respect to the reservoir enthalpy from what appears to be a more suitable angle. The resulting plot of the reference transition Reynolds Number Re^*_{tr} versus h_0 is shown in Figure 5.5 below. Cold tunnel results are once again included to put into perspective the enthalpy range at which the new ones were acquired.

The same observations made earlier for air and nitrogen seem to hold for carbon dioxide as well. The boundary layer follows the same stabilizing trend with increasing reservoir enthalpy. The rate of stabilization, however, is much higher. This may be attributed to the fact that real-gas effects

appear at much lower enthalpies in carbon dioxide, the CO_2 molecules dissociating much more easily into CO and O than the O_2 into 2 O or especially the N_2 into 2 N. In fact, the data appear to settle around a "plateau" very quickly. This would correspond to what was referred to earlier as "complete" dissociation of CO_2. At this point, little further dissociation is possible, the next dissociative reaction ($CO \rightarrow C + O$) requiring more energy than is available at sufficiently high pressure to cause transition on the cone. For air and nitrogen, a similar level of dissociation is unfortunately beyond current capabilities, the cone being too short to reach the necessary Reynolds numbers to observe transition at the desired enthalpies.

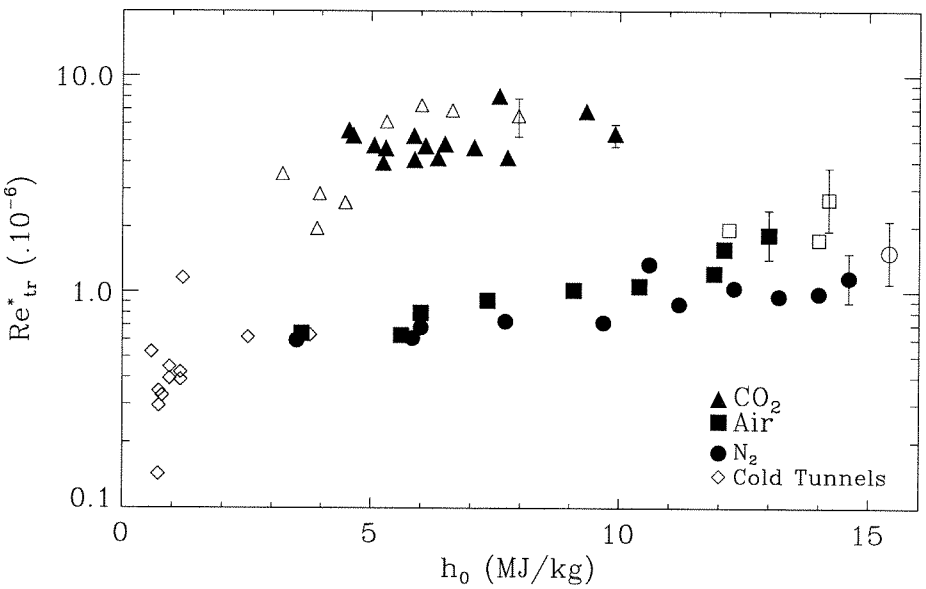

Figure 5.5: Reference transition Reynolds number correlation with stagnation enthalpy. Open symbols indicate flows that were almost fully laminar with a hint of transition. Error bars are approximate measures of the error in Re^*_{tr}

These results, contrary to the weak flow visualization evidence pointing to a first mode instability as the cause of transition, are consistent with transition through a second mode instability. These Mack modes are acoustic in nature and should be stabilized by the chemistry within the boundary layer. Sound waves are known to be absorbed by chemical activity (Clarke and McChesney [1964]) and, as will be shown later in Chapter 7, nonequilibrium chemistry effects in the boundary layer are more pronounced as the enthalpy is increased. This also supports the idea that it is conditions inside the boundary layer that affect the transition process rather than conditions at the edge.

5.3 Reservoir enthalpy normalization

The results, as plotted in Figure 5.5, illustrate one way to normalize the transition location into a Reynolds number while bringing out differences between the different test gases. The next issue that arises is how to now normalize the reservoir enthalpy which is still dimensional. The use of velocity, viscosity and density is straightforward enough to get a Reynolds number out of a length such as x_{tr}, the only real difficulty being to determine at what conditions to evaluate the fluid properties to best represent the flow. Finding an equivalent set of flow characteristics to reduce the reservoir enthalpy, however, is not as obvious.

One immediately thinks of using a characteristic enthalpy of reaction. For nitrogen, this would be the energy needed to dissociate the nitrogen molecule into its atomic components, $\mathcal{D} = 33\,\mathrm{MJ/kg}$. For other gases, however, this becomes more complicated since there could be more than one reaction to choose from. In air, for example, in addition to the dissociation of nitrogen, one must account for the more easily dissociable oxygen molecules. Furthermore, a host of recombination reactions, involving the newly formed atomic nitrogen and oxygen, are also known to take place.

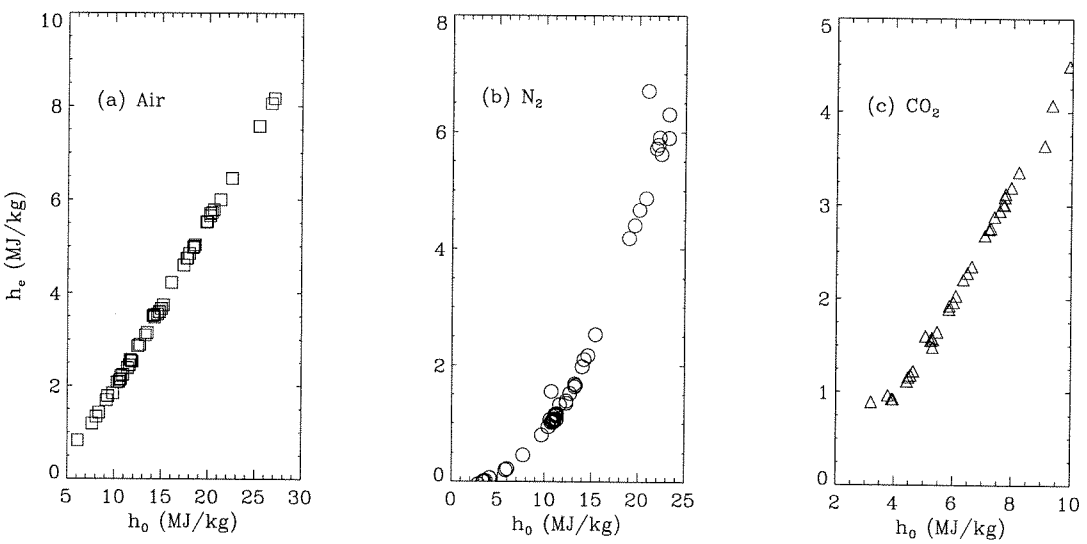

Figure 5.6: Boundary layer edge enthalpy variation with reservoir enthalpy for experiments in (a) air, (b) nitrogen and (c) carbon dioxide.

Other possibilities include the various enthalpies characterizing the flow itself, at the boundary layer level. This could include the reference enthalpy h^*, for reasons similar to those outlined above when evaluating Re^*_{tr}, or the edge enthalpy h_e. Figures 5.6(a)-(c) show the edge enthalpy as a func-

tion of reservoir enthalpy in air, nitrogen and carbon dioxide respectively. Each point corresponds to a specific shot and, as indicated earlier, not all shots yielded transitional boundary layers, especially at higher enthalpies where the flow is mostly laminar and at very low enthalpies where only turbulent traces were observed. The edge enthalpy is evaluated using the frozen freestream chemical composition and assuming this composition remains frozen across the weak shock down to the edge of the boundary layer.

The resulting plot of Re^*_{tr} versus h_e/h_0 is shown in Figure 5.7 and is now fully non-dimensional. While all measurements appear to follow the same curve, it is unfortunate that none of the carbon dioxide data overlap the air and nitrogen data to reinforce this trend. Evaluating the reference enthalpy for each shot and plotting Re^*_{tr} versus h^*/h_0 did not result in any similar noticeable trend. Why h_e then seems to be the preferable energy, as far as the reservoir enthalpy normalization is concerned, remains to be answered.

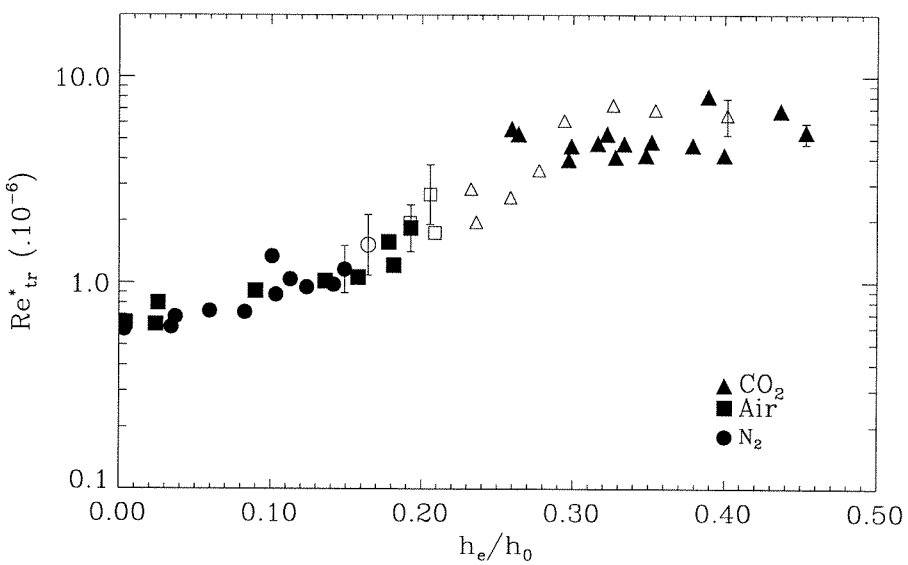

Figure 5.7: Transition Reynolds number evaluated at reference conditions plotted versus normalized reservoir enthalpy.

5.4 Maximum temperature approach

As discussed in White [1991], the reference temperature concept grew out of the desire to find closed form expressions for the heat transfer in laminar boundary layers. Although not corresponding to a "real" physical point within the boundary layer and originally having been derived empirically, it

can be calculated from similarity under certain assumptions. One might therefore wonder whether any alternative states characteristic of the flow could be found to normalize not only the transition location but also the reservoir enthalpy.

One such state is the maximum temperature point within the boundary layer. As illustrated later in Chapter 7, although the freestream is quite hot to start with, even higher temperatures are reached within the boundary layer. The temperature peaks relatively far from the edge before rapidly dropping at the wall. The transition data presented in the previous section were therefore replotted using the maximum temperature point as the normalizing state for both the transition location and the reservoir enthalpy enthalpy. The result is shown in Figure 5.8. The maximum temperature conditions used to redefine the new transition Reynolds number

$$Re_{tr_{T_{max}}} = \frac{\rho_{T_{max}} u_e x_{tr}}{\mu_{T_{max}}} \tag{5.3}$$

are all listed in Appendices C.4 through C.7 at the end. The points shown in Figure 5.8, for the different gases and different enthalpies all seem to follow a same trend, similarly to what was found in Figure 5.7 in the previous section. In fact, there is even a slight overlap between the air/nitrogen data and the carbon dioxide results but unfortunately still not enough to propose any definite conclusions. The three air points clustered in the lower left corner slightly aside from the rest of the results correspond to lower density shots. It is not understood why they lie so distinctively apart.

It should be pointed out that the maximum temperature conditions can only be obtained through a complete solution of the boundary layer profiles. This is one notch higher in terms of difficulty when compared to using the reference conditions. In fact, the results shown in Figure 5.8 were obtained assuming frozen chemistry throughout the boundary layer which, as explained later in Chapter 7, might not be very realistic. A complete nonequilibrium solution is therefore necessary for the sake of accuracy. While the actual maximum temperature might not change much, the gas composition certainly will because of the dissociation and recombination reactions within the boundary layer.

Because of the uncertainty in the reactions occuring in the carbon dioxide boundary layers, only the frozen chemistry computations were shown above. However, sufficient confidence existed in the nonequilibrium calculations for air. Those results indicate an $Re_{tr_{T_{max}}}$ trend with h_0 that is identical to the one observed in Figure 5.8.

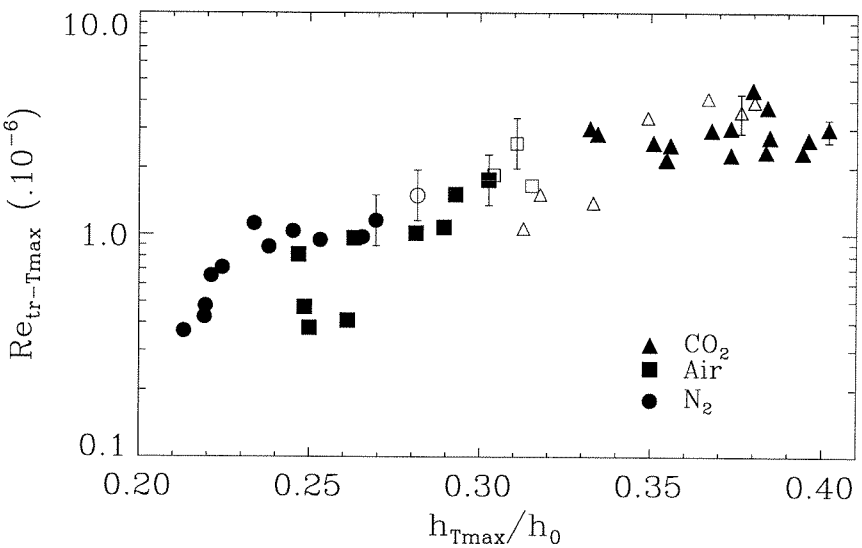

Figure 5.8: Transition Reynolds number evaluated at reference conditions plotted versus normalized reservoir enthalpy.

Chapter 6 Comparison with Free Flight Experiments

Few experimental and numerical data exist that can be directly compared with the results obtained in T5. Granted one cannot compare data from different facilities unless it is certain that the transition mechanisms are the same, it would nevertheless be of great interest to look at other transition data for similar geometries over a similar range of pressure and enthalpy conditions. In particular, it was shown in the previous chapter that normalizing the transition location by boundary layer-specific fluid properties brings out stabilizing trends with enthalpy that are otherwise not apparent. One might then ask whether this can be extended to other tunnels, to other flow regimes and to other environments, free flight being a case where an actual design is the target application.

Extrapolating transition data from conventional wind tunnels to free flight is not always straightforward, as illustrated in Figure 1.4 of the introduction. The measured transition Reynolds numbers are quite often an order of magnitude lower than expected for the same unit Reynolds number. This figure is replotted below in Figure 6.1 along with the corresponding ranges of the T5 transition data

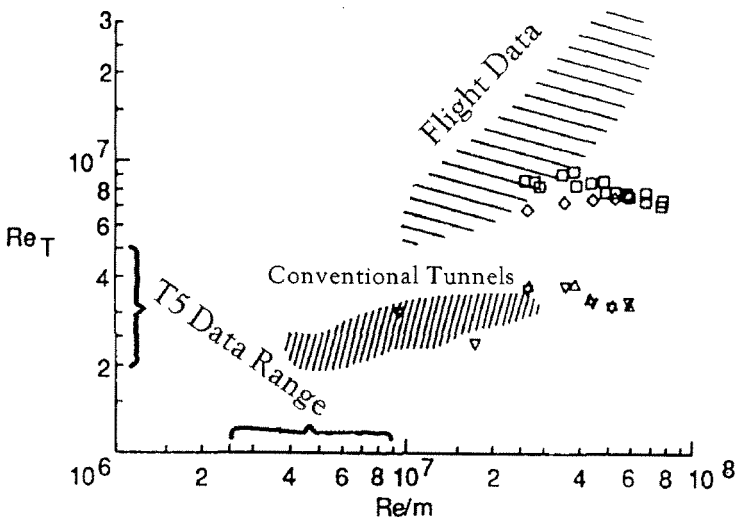

Figure 6.1: Transition Reynolds numbers in conventional tunnels and free flight (Chen *et al.* [1989]). The range of the T5 transition measurements is shown to be within the range of other conventional tunnel data. The upper and lower sets of points respectively correspond to data from the Langley quiet tunnel with a boundary layer bleed valve opened and closed.

discussed in the previous section. As expected, the data all fall well below the envelope of the available flight results. Quiet tunnels give much better agreement since the freestream noise is brought down to a level where it does not interfere with the natural transition process and is therefore closer to the disturbance level encountered in the atmosphere.

The transition Reynolds numbers computed above, however, were evaluated at the edge conditions. For hypervelocity boundary layers, the edge temperature is not representative of the processes in the boundary layer and evaluating the data at the reference conditions might result in a better collapse. For such a comparison, flight data at high enthalpies comparable to those reached in T5 are necessary and the same geometry should be investigated.

6.1 Reentry F test

The reentry F flight experiment, carried out in the late 60s by NASA Langley and declassified several years later (Wright and Zoby [1977]), provides a set of transition data over a range of conditions well suited for a direct comparison with the T5 results. The experiment was conducted to study transitional and turbulent heating at high Mach numbers and enthalpies thereby complementing the existing but limited data from previous experiments.

What makes the reentry F flight experiment of value to the T5 data is that, not only were the total enthalpies achieved within the range of the T5 measurements presented earlier (between 17 MJ/kg and 18 MJ/kg), but the model geometry was exactly the same, i.e., a 5° half-angle cone. Also noteworthy was the fact that the transition detection technique was also identical: thermocouples and the computed heat transfer rate were used to gage the state of the boundary layer. This last point is quite important since different techniques can give different transition locations.

A sketch of the reentry F model is shown in Figure 6.2 below. The 5° half-angle cone was approximately four meters long. The main body was machined out of beryllium and the 21 cm nose tip, with an initial radius r_n around a tenth of an inch, was made out of graphite. The instrumentation consisted of 21 thermocouples, 12 of which were aligned along the same ray as illustrated in Figure 6.2, as well as 2 temperature gages and 13 pressure transducers. The additional instrumentation was used to determine the local flow conditions necessary for the data reduction and analysis.

During the descent, boundary layer transition data were taken over approximately 6 seconds from an altitude of about 30.48 km to 18.29 km. The vehicle's flight Mach number, velocity and altitude history is shown in Figure 6.3, taken from Wright and Zoby [1977]. The Mach number is assumed

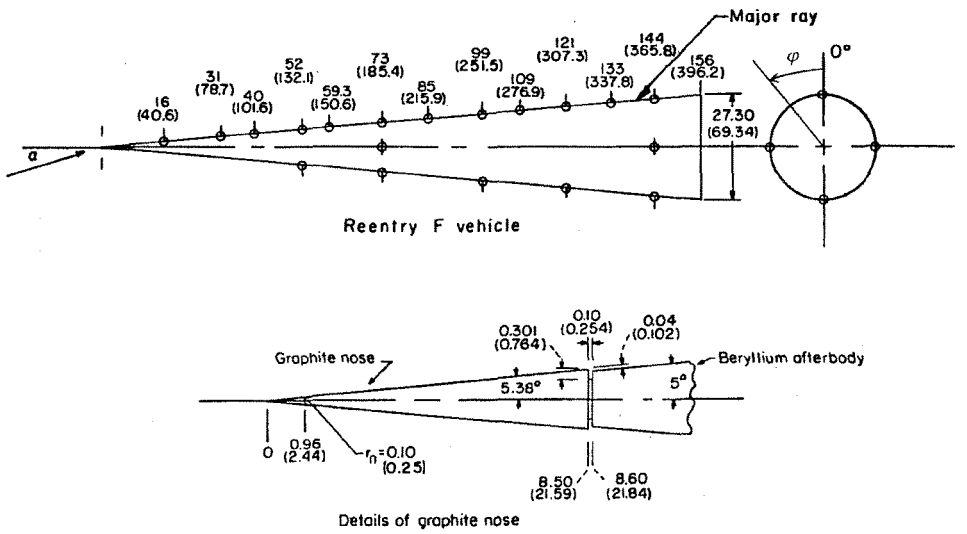

Figure 6.2: Pre-flight F test model geometry (Johnson *et al.* [1972]). Dimensions are in inches and centimeters.

to be constant, around $M_\infty = 20$, during the measurement period. The corresponding freestream Reynolds number varied between $6.56 \times 10^6\,\mathrm{m}^{-1}$ and $52.5 \times 10^6\,\mathrm{m}^{-1}$, the corresponding stagnation enthalpy between 18.3 MJ/kg and 16.9 MJ/kg.

It should be noted that blunting of the nose tip takes place during the descent but there is no certainty, *a posteriori*, how severe the exact change in the tip radius was. This presents a problem since it is necessary to know the flowfield, at least the inviscid one, around the reentry cone to determine the boundary layer edge properties necessary for reducing the data. It might also be necessary to know these conditions to proceed further with a full boundary layer solution. As will be discussed below, different models for the tip radius history had to be computed to bound the blunting and obtain estimates of the edge properties.

6.2 Comparison with experiment

A few of the points that make the reentry F data worth comparing to the tunnel data should be mentioned. It was already stated above that the model geometry is the same. Both the tunnel model and the flight model are 5° half-angle cones. The tip radius of the 1-meter long tunnel model starts out at 0.00025 in and stabilizes at 0.004 in after several shots. For the 4-meter long flight model, the radius starts out around 0.1 in and increases during the descent because of ablation. The degree of ablation itself is unknown. The enthalpy range of the flight data is between 18.3 MJ/kg

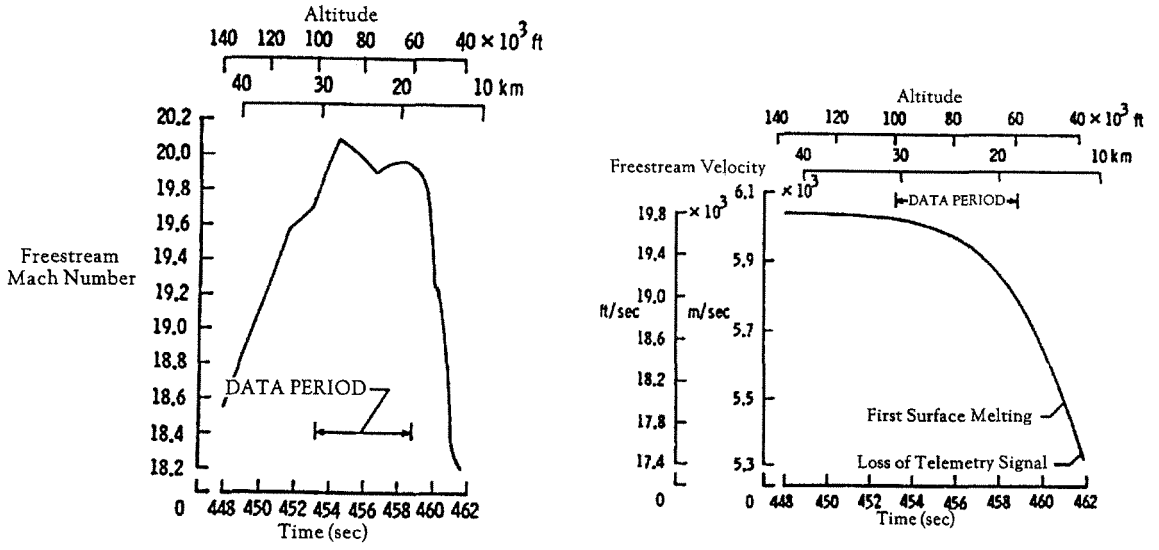

Figure 6.3: Flight Mach number and velocity history (Wright and Zoby [1977])

and 16.9 MJ/kg which is above the largest reservoir enthalpy at which transition was measured in T5 (around 15 MJ/kg for air on Figure 5.5). However, these figures are not too far apart and one should be able to extrapolate the experimental observations to the flight range. The transition detection technique, i.e., surface heat transfer computed from coaxial thermocouples, is also the same for both the T5 tests and the reentry F test.

Some of the notable differences between the two experiments include the fact that the wall to stagnation temperature ratio varies over a much larger range for the tunnel data than over the limited measurement period of the reentry test ($T_w/T_0 \approx 0.1$). The freestream dissociation level is also different in both cases. In free flight, α_∞ is close to zero depending on the altitude. Most of the dissociation is then produced not after the weak shock but within the boundary layer. In the case of the shock tunnel the air is highly dissociated by the incident and subsequent reflected shocks. Some recombination occurs with the nozzle as the flow is accelerated into the test section. The reactions, however, freeze before the recombination is complete leaving the freestream composition quite different from the free flight case. Of course, further dissociation occurs again within the boundary layer as is illustrated later by the computations in Chapter 7.

Further differences between the two sets of data to be compared are the bluntness history and the flow quality. The tunnel data consists of discrete points, each run corresponding to a set enthalpy. The flight data, however, was recorded continuously over a 6 second period during which the conditions were continuously changing. The tip geometry is therefore fixed for the tunnel runs and

measured before as well as after the shot. The model is always assumed to be "sharp". The flight tip, however, was not monitored during the descent and blunting was known to be possibly quite severe. In fact, an "anomaly" was observed in the heat transfer measurements because of differential temperatures that resulted in probable bending of the cone (Wright and Zoby [1977]). Boundary layer edge conditions were therefore computed for the reentry F test assuming three different ablation models. The results shown below correspond to the worst and best case scenarios. Comparison with the tunnel data are only made over the range of conditions where the two models agree, i.e., where the tip remains nominally sharp.

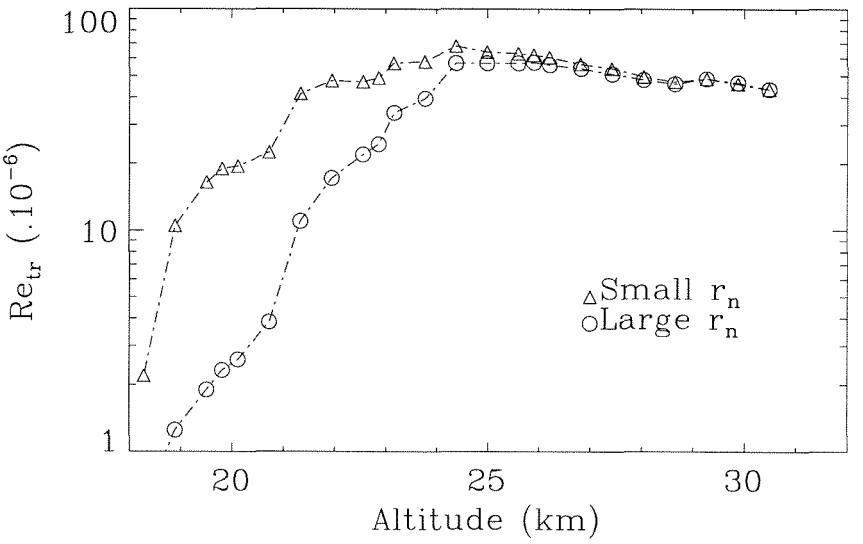

Figure 6.4: Altitude variation of transition Reynolds number during reentry F test. Triangles correspond to the case where the tip remains "sharp" during the data period, circles to the case where more severe blunting occurs.

The issue of freestream noise is also one to keep in mind. As has been mentioned several times already, the noise spectrum of the T5 freestream is unknown. Disturbance levels are expected to be high but the spectrum content is also unknown. It is therefore not certain through which one of the instability modes boundary layer transitions though weak visual evidence does point to the first mode (Germain [1994]). This is not necessarily the most unstable mode since external noise can preferentially amplify other modes, should the conditions be right. Nor is spectrum information available for the reentry flight data, but it is quite likely that the disturbance levels are far smaller. The transition process in this latter case is therefore more likely to be induced by disturbances at the most unstable frequency. Theoretical predictions, with no or limited chemistry models, point

to the second mode. However, one should remember the complexity of the actual hypervelocity nonequilibrium chemistry, as alluded to later in Chapter 7, which could actually have a stabilizing effect on the second mode and favor other modes instead.

Figure 6.4 shows the altitude variation of the reentry F transition Reynolds number. The transition location is deduced from the heat transfer measurements and normalized by the corresponding boundary layer edge conditions. Results from the two different models for the ablation are plotted. Both curves agree quite well from the beginning of the data period at 30.5 km to approximately 24 km. It is assumed that it is over this range that the data is most suitable for comparison to the tunnel data. Plotted below, in Figure 6.5, is the corresponding enthalpy over the range where the tip is assumed to be the sharpest. Again, the data used for these plots were taken from Wright and Zoby [1977] where a detailed list of the conditions at each data point can be found.

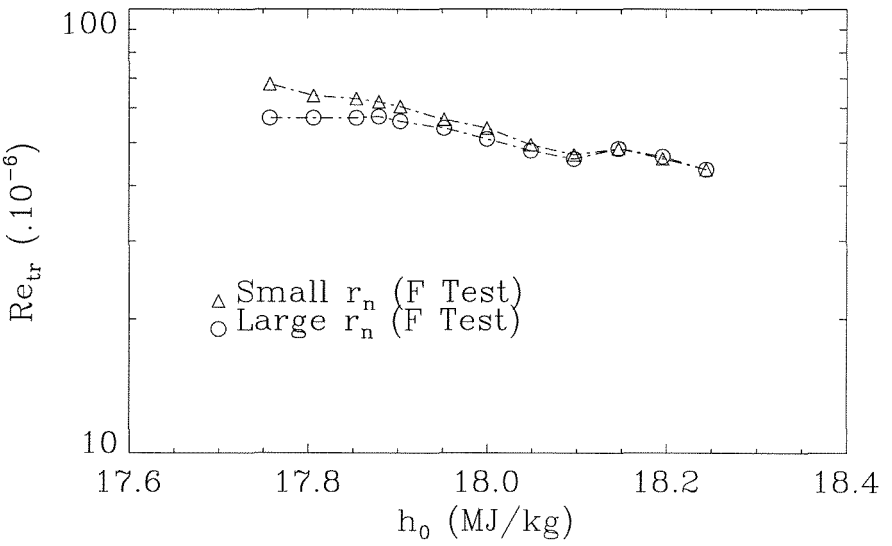

Figure 6.5: Stagnation enthalpy variation of reentry F test transition Reynolds number. Points shown correspond to the part of reentry where the tip stays "sharp", regardless of the ablation model chosen.

Figure 6.6 shows the reentry F test transition Reynolds numbers Re_{tr} plotted with all the available T5 air data with respect to stagnation enthalpy h_0. As expected, the free flight results fall more than an order of magnitude above the shock tunnel data and fit approximately within the ranges shown in Figure 6.1 earlier. Of note, however, is the trend in the flight data: a steady decreasing one with increasing stagnation enthalpy. This is different from the tunnel data observations made

earlier where the normalization of the transition location with the boundary layer edge conditions did not seem to reveal anything noteworthy. This was illustrated, for example, in Figure 5.4 albeit with fewer data points and with measurements from other gases.

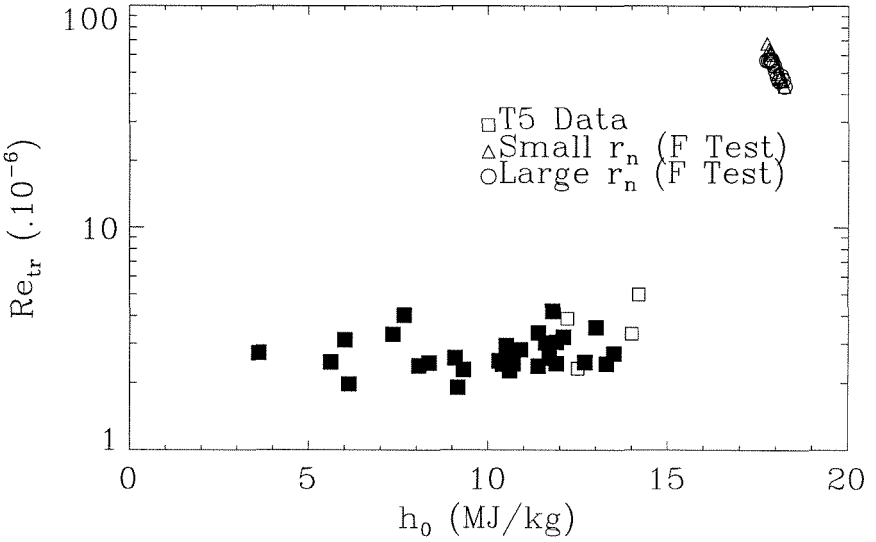

Figure 6.6: Comparison of free flight transition Reynolds numbers and all T5 air data

When plotting the reference transition Reynolds numbers Re^*_{tr}, the order of magnitude distinction now disappears and the data collapse to within a much narrower range over the enthalpies considered, as shown in Figure 6.7 below. The stabilizing trend in the tunnel transition Reynolds numbers with increasing enthalpy, described earlier in Chapter 5, is also visible. The tunnel data show the characteristic increase in Re^*_{tr} with increasing enthalpy while the flight figures decrease, as was already observed in Figure 6.6 above. This would lead one to believe that, at least as far as enthalpy effects are concerned, one is again well justified in using reference conditions to define the transition Reynolds numbers. The most probable cause for the differences observed between the flight and tunnel results is the uncertainty in the bluntness of the tip which can yield very different boundary layer edge conditions and hence, very different transition Reynolds numbers no matter what conditions are used for the normalization. Freestream noise should also be kept in mind since different transition modes are certainly influenced differently by the chemistry, the Mack mode being stabilized and the Tollmien-Schlichting mode perhaps destabilized.

The difference between typical high enthalpy flight and tunnel boundary layers is illustrated in

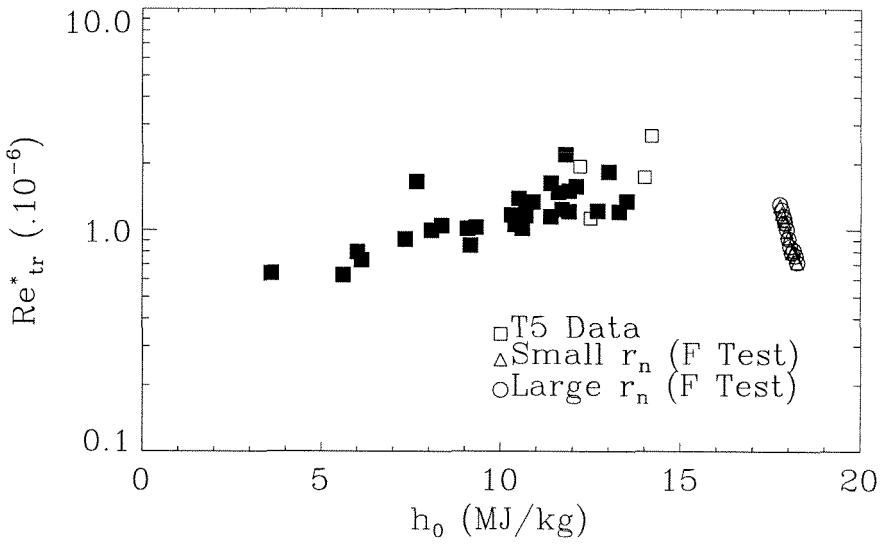

Figure 6.7: Comparison of free flight reference transition Reynolds numbers and all T5 air data

Figure 6.8. The figure also illustrates why the use of reference, or maximum temperature, conditions better characterize the flow than the edge conditions. Both temperature profiles correspond to flows with $h_0 \approx 14$ MJ/kg. In the flight case, the surrounding atmosphere is "cold," undissociated and it remains so, even after it has been processed by the weak conical shock around the flight model. In the shock tunnel, however, the freestream temperature is several times as high, at a much lower Mach number, and partially dissociated. Evaluating Reynolds numbers at the edge conditions, with temperatures almost 4 times higher in the tunnel would then obviously yield very different results. The maximum temperature conditions, only about 10% apart for this particular example, are therefore a much better choice. The corresponding reference temperature levels calculated from Equation (4.7) are also illustrated in Figure 6.8.

As a final note, although not shown, the F test data correlate well with the tunnel data in Figure 5.7 where Re^*_{tr} is plotted versus the normalized reservoir enthalpy. The flight points lie at the far left of the plot at values of h_e/h_0 close to zero and of Re^*_{tr} around a million. The reason for the low h_e/h_0, compared to tunnel boundary layers with the same stagnation enthalpy, is simply that the edge is colder resulting in a much lower h_e.

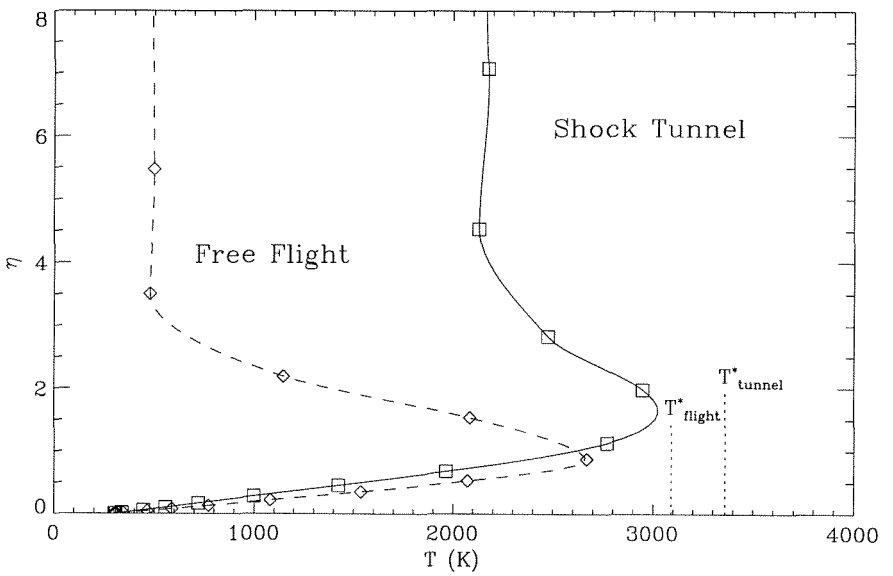

Figure 6.8: Typical tunnel and flight boundary layer temperature profiles in boundary layer coordinates ($h_0 \approx 14$ MJ/kg).

Chapter 7 Enthalpy Effects on Laminar Heat Transfer

Previous boundary layer experiments in T5 by Germain [1994] were aimed at exploring the laminar, transitional and turbulent regimes in air and nitrogen flows. Stagnation pressures and temperatures were varied to study conditions ranging from perfect gas to real gas. Test gases explored were air and nitrogen; however, because the transition Reynolds number was found to correlate with enthalpy differently for each gas, a few runs were carried out with two more different gases, namely carbon dioxide and helium. The present set of experiments was therefore mostly directed towards seeking to extend the carbon dioxide measurements and complete the air data by looking exclusively for conditions were transition would occur.

The enthalpy ranges where transition could be observed on the cone model in air were well known from the older experiments. Tailoring the test conditions in air or nitrogen to the boundary layer states of interest was therefore relatively straightforward. Changing the initial shock tube pressure, and the corresponding compression tube makeup, one can easily select the desired enthalpy level *a priori* for a given diaphragm and pressure level. However, since very little was known about the transition behavior of carbon dioxide, getting fully laminar, and occasionally fully turbulent, boundary layers was inevitable.

Understanding laminar boundary layers, although seemingly simple and uneventful, is actually quite important since it is of direct consequence to transition mechanisms. Furthermore, under hypervelocity conditions, the chemistry inside the boundary layer and at the wall can be quite complex especially when the gas is readily dissociated. It was therefore decided that the present study should also include an investigation of the laminar experimental data in conjunction with numerical simulations of the chemically reacting boundary layer. In addition to the laminar boundary layers obtained in carbon dioxide over a wide range of conditions, several laminar cases were also studied in air. These new runs in air were obtained to complement the older data and extended into regions of higher pressures and enthalpies than had been previously achieved.

Tables B.1 through B.3 summarize the conditions for the three series of shots performed for this study. The first series (shots 671 to 690) consisted of 19 air shots and 1 carbon dioxide shot. The second series (shots 873 to 888) consisted of 16 shots carried out exclusively with air. The boundary

layers observed were for the most part laminar although a few showed signs of transition. The third series (shots 1113 to 1164) consisted of 17 air shots and 35 carbon dioxide shots. In this latter series, an effort was made to cover conditions that included laminar, transitional and turbulent boundary layers. Shots 885 to 888 used a conical nozzle, as opposed to a contoured nozzle, thereby imposing a pressure gradient over the surface of the model. These shots are not included in the discussions hereafter. All air runs considered, the stagnation enthalpies h_0 ranged from 6 MJ/kg to 30 MJ/kg and the stagnation pressures P_0 from 30 MPa to 85 MPa. For the carbon dioxide runs, the stagnation enthalpies h_0 ranged from 3 MJ/kg to 10 MJ/kg and the stagnation pressures P_0 from 40 MPa to 95 MPa.

7.1 Laminar air boundary layers

7.1.1 Typical heat transfer traces

Over the range of stagnation pressures P_0 covered in these experiments, from 30 MPa to 85 MPa, boundary layers were found to be fully laminar over the entire surface of the cone at stagnation enthalpies h_0 greater than 14 MJ/kg. A few exceptions at lower enthalpies also exhibited fully laminar flows.

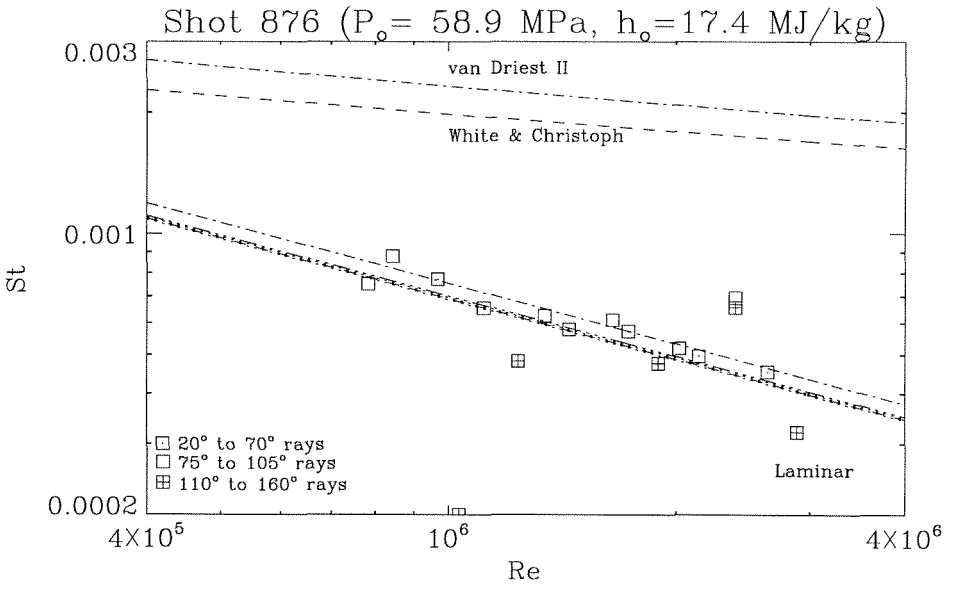

Figure 7.1: Typical heat transfer traces for a fully laminar air boundary layer. The square symbols (□) represent the experimental data. The various lines represent either theoretically or computationally predicted heat transfer levels for the laminar and turbulent regimes.

A typical example of a fully laminar boundary layer is shown in Figure 7.1 above. The experimental data, represented by the square symbols, are divided into three azimuthally separated regions to bring out possible flow asymmetries over different sections of the cone. The contoured nozzle used for these experiments does not exhibit a perfectly symmetric exit profile (Rousset [1995]) causing, in some cases, one side of the cone to begin to transition at a slightly different spot than another side. The two lines well above the data represent the predicted turbulent heat transfer levels for the two different models described in Section 4.2. These levels would have been reached had the boundary layer turned fully turbulent. Although very close to one another, there are actually four lines going through the experimental points each with the characteristic $Re^{-\frac{1}{2}}$ behavior expected, as illustrated by Equation 4.11, for laminar heat transfer in a zero pressure gradient boundary layer. The dashed-dot line slightly above the other three represents a BLIMPK simulation with nonequilibrium chemistry and a catalytic wall. The other lines correspond to a BLIMPK nonequilibrium simulation with a noncatalytic wall, a BLIMPK simulation with frozen chemistry and the theoretical prediction described in Section 4.1.

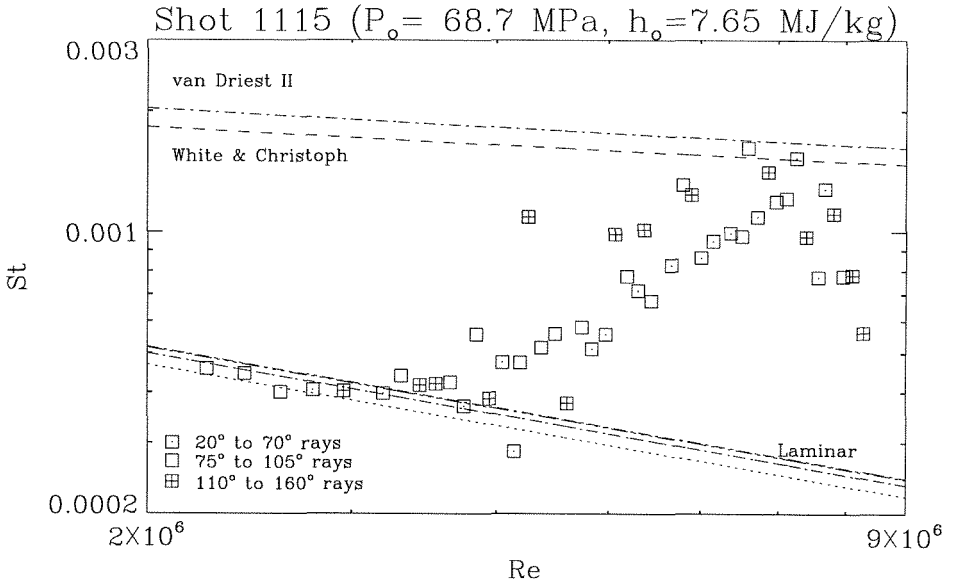

Figure 7.2: Typical heat transfer traces for a laminar/transitional boundary layer.

Some runs, although not laminar over the entire length of the model, do transition late enough that the behavior of the laminar part of the boundary layer can still be captured. This is illustrated above in Figure 7.2 which shows a typical heat transfer distribution for a boundary layer that is almost becoming turbulent towards the end of the cone. The laminar region is clearly separable and

well captured by the theoretical and numerical predictions. As the heat transfer increases through the transition zone, the points get closer to the theoretical turbulent lines. The sudden drop-off at the end is a repeatable effect at certain flow conditions due to a wave emanating from the nozzle end and impinging on the model (Germain [1994]).

7.1.2 Enthalpy effects

In order to compare the laminar heat transfer for boundary layers under different flow conditions, it is necessary to select a parameter representative of these conditions. As was illustrated in the two preceding Figures 7.1 and 7.2, and looking at Equation 4.11, the laminar heat transfer rate normalized into the Stanton number is directly proportional to $Re^{-\frac{1}{2}}$:

$$St = \frac{\mathcal{A}}{\sqrt{Re}}, \tag{7.1}$$

where the dimensionless constant of proportionality $\mathcal{A}$, for a chemically frozen laminar boundary layer, is given by

$$\mathcal{A} \approx \frac{0.664\sqrt{3}}{2} \frac{\sqrt{C^*}}{Pr^{2/3}}. \tag{7.2}$$

While the power of the Reynolds number determines the slope of the laminar line, as shown in Figures 7.1 and 7.2 for example, it is the value of $\mathcal{A}$ in Equation 7.2 that determines the vertical intercept and hence the overall heat transfer rate level. This value, assuming the Prandtl number Pr is relatively constant, is strictly a function of C^*, a function itself of the enthalpy. Departures of $\mathcal{A}$ from its frozen value are then a measure of the chemical activity.

Looking at the behavior with enthalpy of the constant defined in Equation 7.2, one can then elucidate the behavior of the heat transfer rate as described by the theory and compare it to what is observed in actuality. To obtain the constant corresponding to the experimental results, it is necessary to fit a line with the correct $Re^{-\frac{1}{2}}$ slope through the points. A least-squares fit of the form $\log St = a \log Re + b$ is straightforward and the additive constant b is nothing but the logarithm of the desired constant, a being forced at $-\frac{1}{2}$. Least squares fits need not be obtained for the numerical data since the distribution automatically follows an $Re^{-\frac{1}{2}}$ law and the constant can simply be obtained by picking out any combination of Re and St that falls on the predicted curves. It should be noted at this point that the power of the Reynolds number is only a function of the external pressure gradient imposed on the boundary layer. In the case of zero pressure gradient flow it can be shown to be exactly $-\frac{1}{2}$ but if a positive or negative gradient were to be applied the slope would change accordingly (White [1991]).

Figure 7.3 is an example of how the experimental data fit compares to all the predictions for a given shot. The differences between all the lines are reason alone to take a closer look at the structure of this type of boundary layer. Obviously, the chemistry model plays a significant role in the heat transfer rate and it appears that none of the models satisfactorily reproduce the experimental behavior, at least as far as this run is concerned. Including, however, a roughly estimated 25% uncertainty at high enthalpy in the experimental heat transfer, it does seem that the computation with nonequilibrium chemistry and a catalytic wall comes closest to the data points. At lower enthalpies, the differences are far less pronounced as one could imagine if a fit were to be passed through the laminar points in Figures 7.1 and 7.2 shown earlier. One should keep in mind that the nonequilibrium calculations with a catalytic wall are expected to yield higher heat transfer rates than the noncatalytic cases. This is due to the surface recombination reactions which release heat as opposed to possible dissociation reactions in the gas phase which absorb heat. The effect of dissociation in the gas phase, however, is often offset or at least attenuated by some recombination reactions as well.

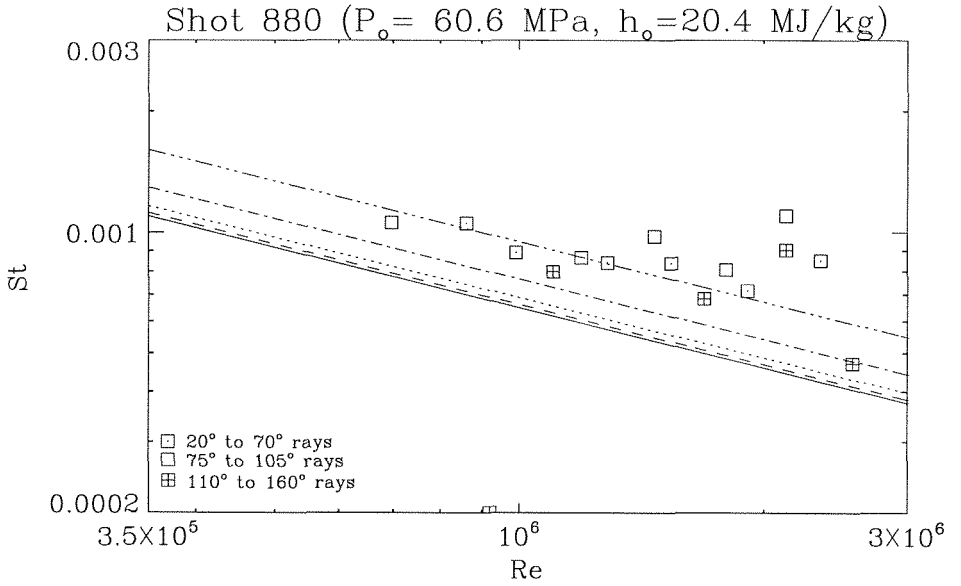

Figure 7.3: Comparison of experimental data fit with theoretical and numerical predictions. Lines, from bottom top top, represent BLIMPK frozen (full), BLIMPK nonequilibrium/noncatalytic (dash), theoretical (dot) and BLIMPK nonequilibrium/catalytic predictions (dash-dot). The uppermost line (dash-dot-dot) is a least squares fit of the experimental data

Freestream conditions for all the runs performed in T5 were used to compute the corresponding boundary layer edge conditions, as outlined in Section 2.3, and then the laminar boundary layer heat transfer using BLIMPK with the different chemistry options available: frozen and nonequilibrium

with or without catalytic wall reactions. The dimensionless constant corresponding to Equation 7.1 was then plotted as a function of enthalpy and the result is shown in Figure 7.4. The nonequi-

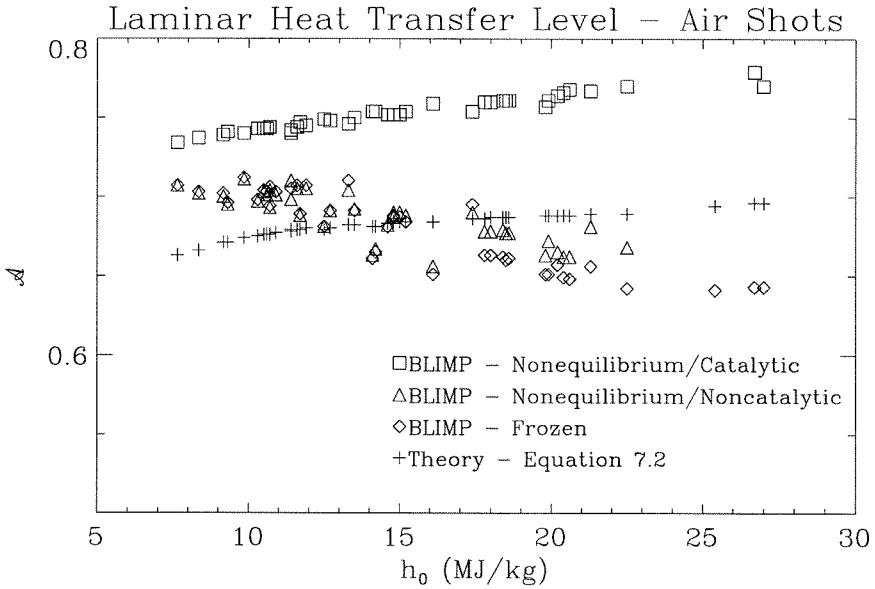

Figure 7.4: Computed and theoretical laminar heat transfer levels (Air shots)

librium/catalytic and the theoretical points exhibit the expected increase in heat transfer with increasing enthalpy. As was pointed out above, the calculations with the catalytic wall are consistently above all of the other computations because of the surface recombination reactions. The BLIMPK noncatalytic and frozen calculations do not, however, follow similar trends. In fact, after starting off for lower enthalpies at seemingly appropriate values of the heat transfer rate, the levels computed drop off around $h_0 = 15\,\mathrm{MJ/kg}$ as the enthalpy is increased further. This is probably due to the fact that the species mole fractions do not correspond to the composition that would exist in actuality were the appropriate reactions allowed to take place. This is particularly true when compared to the catalytic wall where most if not all of the atomic species recombine and diffuse. The theoretical prediction, obtained from Equation 7.2 with a constant Prandtl number, is perhaps more reliable than the frozen computation since the reference temperature formulation weighs actual flow conditions across the boundary layer. The experimentally derived values of $\mathcal{A}$ would appear scattered around the computations and are better illustrated in the following figure.

Figure 7.5 illustrates these increasing differences between the nonequilibrium catalytic computations and the frozen computations as the enthalpy is increased. The dashed line is a least squares fit of the $\mathcal{A}_{catalytic} - \mathcal{A}_{frozen}$ results. The corresponding experimental points are also shown. The

vertical error is typically ± 0.1 and the uncertainty stems from the scatter of the laminar data. It should be noted that deviations from catalytic computations do appear large but are in fact quite reasonable especially when compared to the carbon dioxide results to be shown later in this chapter.

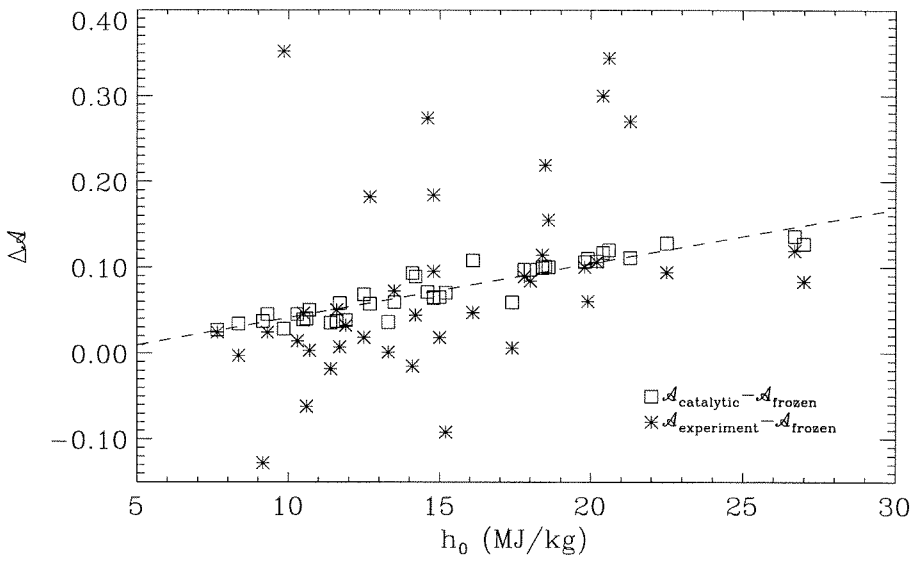

Figure 7.5: Heat transfer deviations from frozen laminar heat transfer levels (Air shots)

7.1.3 Boundary layer profiles and chemistry

Using BLIMPK, it is possible to compute the profiles of quantities such as velocity, temperature, density and species concentration across the boundary layer, from the wall to the edge. This provides a look at the inner structure of the layer and in particular at the role of the different chemistry models on this structure. To illustrate these differences, two shots were chosen at quite different ends of the spectrum of conditions achievable in T5. The first shot, a fully laminar boundary layer, corresponds to a high enthalpy case with temperatures sufficiently high to cause freestream dissociation of the oxygen. Wall reactions are also expected to play an important role since the high concentration of atomic species would probably promote recombination. At the second computed condition, the flow goes from laminar to turbulent and corresponds to a much lower enthalpy.

Velocity, temperature and density profiles for the first case, shot 671, are shown in Figures 7.6(a)-(c) below. The stagnation pressure P_0 was 78.6 MPa and the stagnation enthalpy h_0 was 21.3 MJ/kg for this shot. The calculations are made at three stations along the surface of the cone corresponding to distances x from the nose tip of 1 ft, 2 ft and 3 ft. The velocity profiles are typi-

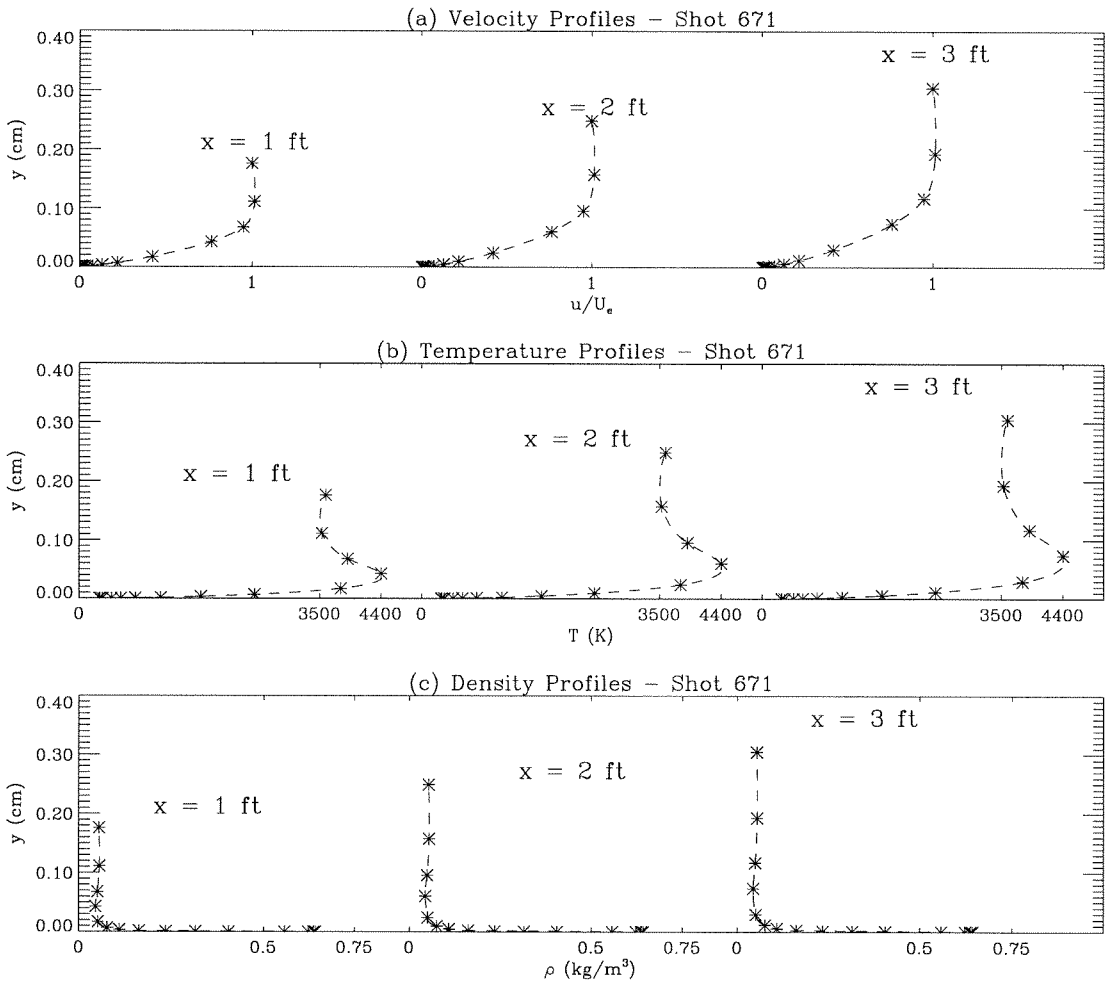

Figure 7.6: (a) Velocity, (b) temperature and (c) density profiles for shot 671

cal of a laminar boundary layer and the thickness $\delta_{.99}$ reaches a couple of millimeters. This latter figure is quite important since the second instability mode of the boundary layer has a wavelength of roughly two times the thickness which in this case could be on the order of a Megahertz. Also of interest is the temperature profile. It is characteristic of a compressible boundary layer and exhibits a maximum temperature about a quarter of the way up from the wall. It also illustrates very well the range of temperatures across the boundary layer starting out at the "cold" wall to the maximum temperature point within tenths of a millimeter and finally to the equally hot edge. The chemistry must therefore be modeled as accurately as possible if one accounts for the fact that at temperatures reaching several thousands of degrees, air is strongly dissociated and a host of reactions, ranging from further gas-phase dissociation to surface recombination, can take place. As a short aside, it should be mentioned that, for a given enthalpy, a corresponding "real" free flight boundary layer

would see an almost identical maximum temperature although the edge temperature would be much cooler because of the surrounding atmosphere. This point was illustrated in earlier chapters when the issue of which temperature best represents the boundary layer was addressed.

Species concentrations at the $x = 1\,\text{ft}$ station are shown below in Figures 7.7(a) and (b) for nonequilibrium chemistry calculations with a catalytic and a noncatalytic wall respectively. Although there are quite noticeable differences between the two chemistry models as far as the species concentration plots are concerned this is not the case for the velocity, temperature and density plots shown above. In fact, Figures 7.6(a)-(c) all correspond to frozen chemistry calculations. Qualitatively, there would have been no striking difference between these figures had a nonequilibrium/catalytic or noncatalytic calculation been plotted alongside them. Only a slight difference in maximum temperature would be noticeable for the catalytic wall case, at these conditions.

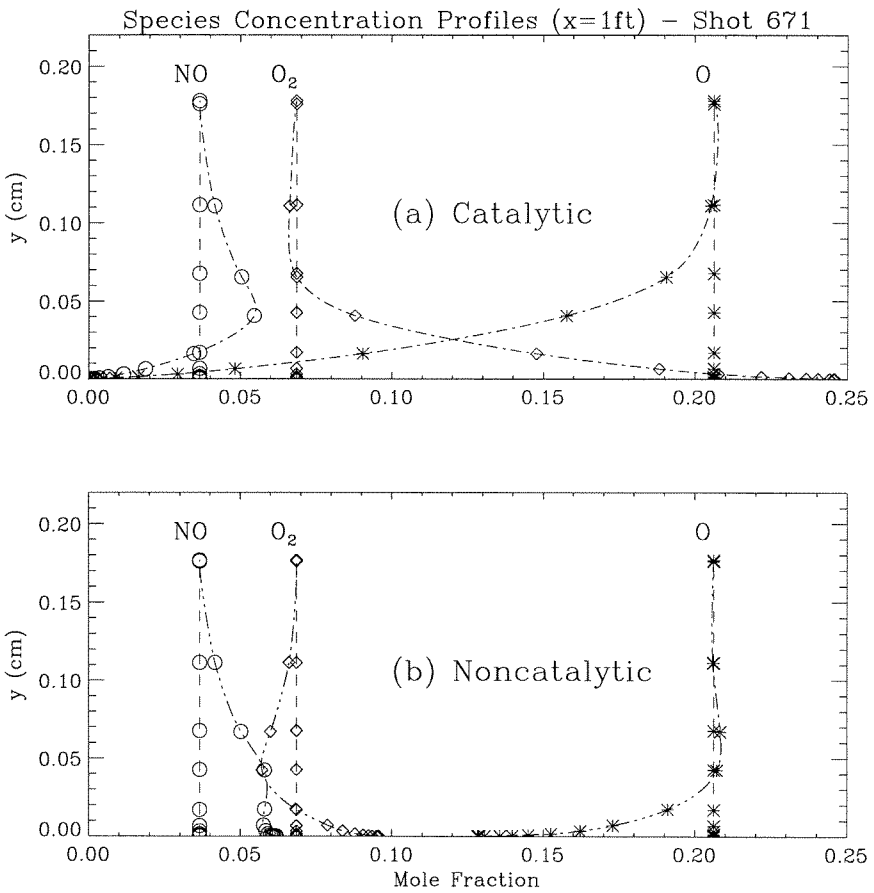

Figure 7.7: Nonequilibrium concentrations with (a) catalytic and (b) noncatalytic walls for shot 671. The vertical line for each species corresponds to the frozen edge compositions.

In Figures 7.7(a) and (b), the straight vertical lines drawn for each species from the edge to the wall correspond to the frozen levels. As was pointed out earlier, for this high enthalpy shot, molecular oxygen O_2 is highly dissociated at the edge, atomic oxygen O being the predominant species. At the catalytic wall, as expected, all of the O recombines to give O_2. Some NO is formed because of the plentiful supply of O and some dissociation of N_2 (not shown in the figures) at the higher temperatures but quickly decreases close to the wall as the N recombines as much as the O. The gas is entirely made up of molecular oxygen and nitrogen at the wall. In the noncatalytic case for shot 671, there is no possibility of recombination at the wall so that the O_2 dissociates even further from the edge down as the temperature goes up. However, once it approaches the cold wall, the little O that was formed recombines. There is also a slight increase in NO. The recombination at the noncatalytic wall, however, is far from complete as compared to the efficient catalytic one.

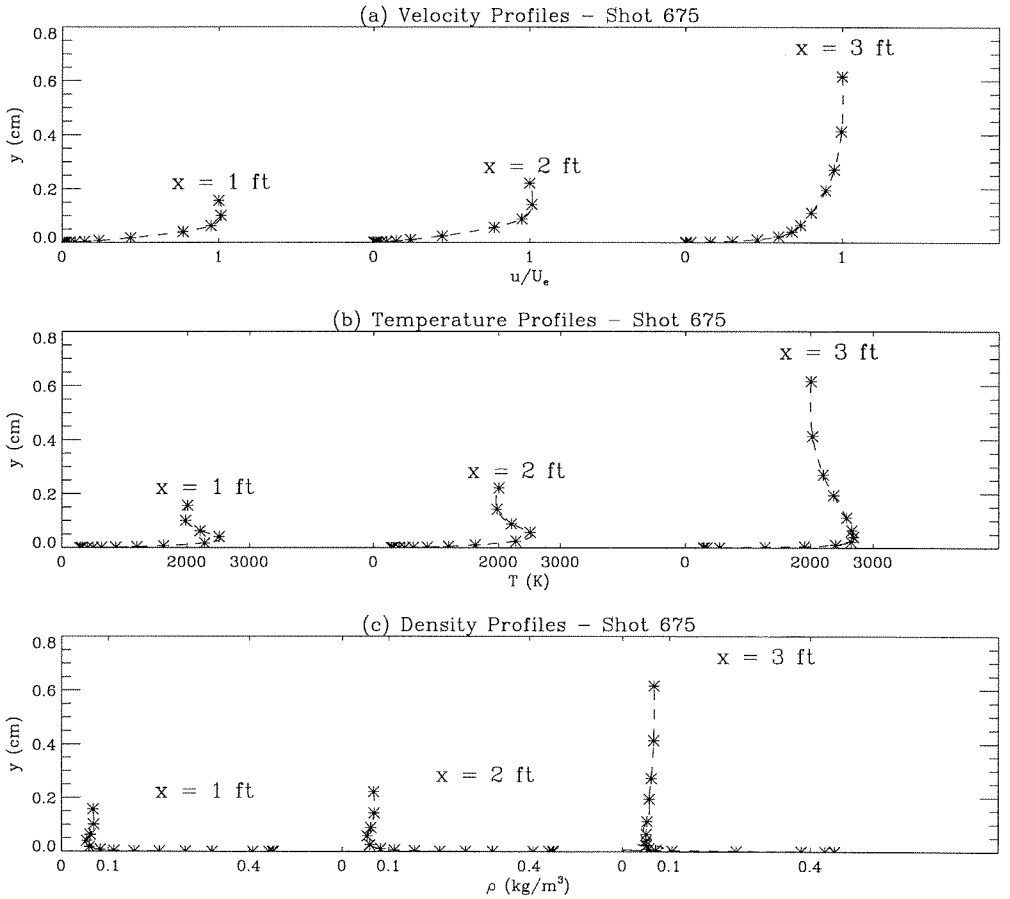

Figure 7.8: (a) Velocity, (b) temperature and (c) density profiles for shot 675

The next example, shot 675, illustrates what happens at lower enthalpies when the temperatures are lower and the boundary layer does not stay fully laminar over the entire model. Velocity,

temperature and density profiles for this second case are shown in Figures 7.8(a)-(c). The stagnation pressure P_0 was 58.5 MPa and the stagnation enthalpy h_0 was 10.5 MJ/kg for this shot. At the first two stations, $x = 1$ ft and $x = 2$ ft, the boundary layer is laminar and all three profiles look like those in Figures 7.6(a)-(c). However, in order to conform with the experimentally observed transition further down, the third station was switched within the computations to become turbulent. This manifests itself as a thicker boundary layer and "fuller" profiles. Also noticeable is the fact that the maximum temperature point, although the same in magnitude as in the laminar cases, is much closer to the wall.

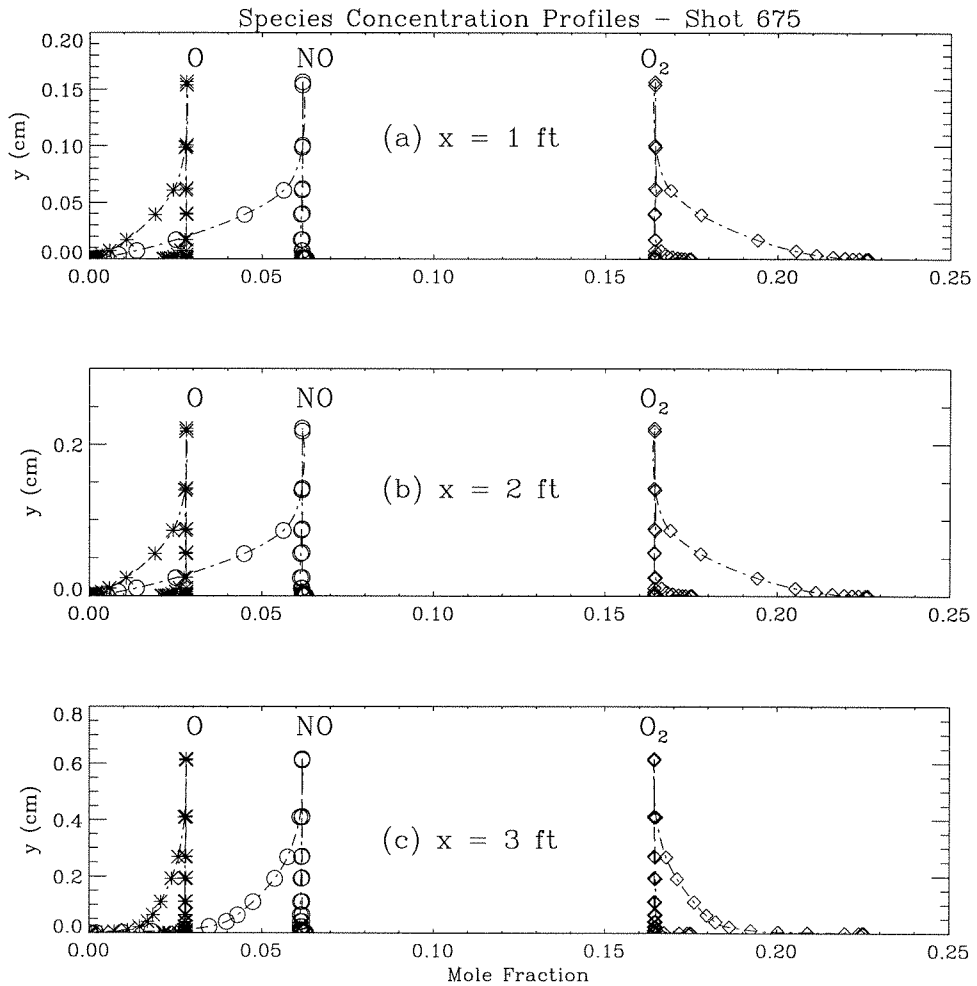

Figure 7.9: Nonequilibrium catalytic and noncatalytic concentration profiles at $x =$ (a) 1 ft, (b) 2 ft and (c) x=3 ft for shot 675. The vertical line for each species corresponds to the frozen edge compositions. The noncatalytic results are barely distinguishable from the frozen levels except close to the wall. The dash-dot curve is the catalytic result.

The species concentration profiles corresponding to the three computed x stations are plotted in Figures 7.9(a)-(c). Contrary to the high enthalpy shot shown earlier, in this case, the freestream is far less dissociated. Instead of having largely atomic oxygen O at the edge, its molecular counterpart O_2 now dominates. The temperatures within the boundary layer are not as high either thereby thwarting any chance for further dissociation within. The frozen composition and the nonequilibrium profile with the noncatalytic wall are practically indistinguishable except close to the wall where the low temperature causes some recombination to O_2. As far as the catalytic wall calculations are concerned, as in the previous case, all of the species formed through the dissociative processes now recombine leaving solely molecular oxygen O_2 and nitrogen N_2 (not shown) at the wall. Although, because of the scale, the concentration curves seem to approach the wall tangentially, they actually end in the wall at right angles, the concentration rate of change with respect to y being zero.

7.2 Laminar carbon dioxide boundary layers

7.2.1 Typical heat transfer traces

Since many of the carbon dioxide runs performed yielded laminar boundary layers over part if not all of the model, it was decided to study enthalpy effects following the same approach that was used for the air shots described in the previous section. The stagnation pressures P_0 for these shots went from 40 MPa to 95 MPa, roughly the same range as for the air runs. Fully laminar boundary layers were observed for stagnation enthalpies h_0 greater than 7 MJ/kg. Down to 5 MJ/kg, the boundary layers would become mostly transitional but still exhibiting a sufficiently long laminar region to infer laminar heat transfer levels. A typical example of a laminar carbon dioxide boundary layer is shown in Figure 7.10. No striking feature distinguishes it from its air counterpart and it follows the same characteristic $Re^{-\frac{1}{2}}$ behavior.

Figure 7.10 does however show that the numerical simulations do not capture the correct experimental heat transfer. In fact, all three computations - frozen, nonequilibrium/catalytic and nonequilibrium/noncatalytic chemistry - fall well below the measurements. The theoretical heat transfer level, given by the dotted line, is a bit closer but falls below nevertheless. This difference is not observed at all pressure and enthalpy levels as will be pointed out in the next section. Most probable reasons for these differences are an incomplete understanding of the correct chemistry in the gas-phase and at the wall. Carbon dioxide dissociates at lower temperatures than air and the associated chemical reactions (Appendix D.2) are not as well understood and have not been as extensively studied as those in air.

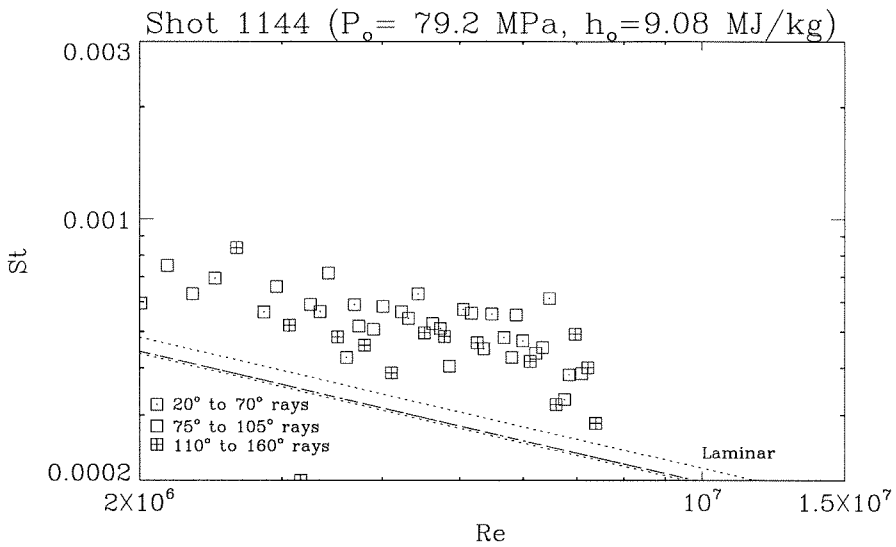

Figure 7.10: Typical heat transfer traces for a laminar carbon dioxide boundary layer. The square symbols (□) represent the experimental data. The various lines represent either theoretically or computationally predicted heat transfer levels for the laminar regime.

7.2.2 Enthalpy effects

Again, following the approach that was used for the air flows, it was decided to characterize the laminar heat transfer level by the same dimensionless constant $\mathcal{A}$ given in Equation 7.1. This is the constant of proportionality between the Stanton number St and $Re^{-\frac{1}{2}}$ which contains all the information about the flow conditions and chemistry. While this constant can be evaluated explicitly in the theoretical case, assuming the chemistry is frozen, it must be obtained again by fitting the appropriate line through the experimental data. As far as the BLIMPK computations are concerned, the results automatically follow the standard $Re^{-\frac{1}{2}}$ behavior and evaluating the constant at any streamwise station is straightforward. For the sake of comparison and of identifying the more suitable chemistry model, each experimentally obtained run was simulated with both frozen and nonequilibrium chemistry. In the latter case, catalytic and noncatalytic walls were considered.

Over the enthalpy range considered, 6 MJ/kg $< h_0 <$ 10 MJ/kg, the computations and theoretical results do not differ by more than 15% as was the case in air and as was illustrated in Figure 7.4. The trends with enthalpy are also quite similar as far as the theoretical predictions are concerned. The computations, however, follow somewhat different trends than in air. Specifically, the catalytic BLIMPK results, although predictably higher than the frozen and noncatalytic results, do not exhibit the same increase in heat transfer with increasing enthalpy. Most important, however, is how the experimental results compare with the computations and theory.

The dimensionless constant $\mathcal{A}$ is plotted in Figure 7.11 below for the carbon dioxide runs. Contrary to the seemingly good agreement between the air experiments and the various models, as was illustrated earlier in Figures 7.4 and 5.5, the carbon dioxide results deviate considerably between 7 MJ/kg and 9 MJ/kg. There seems to be a pronounced hump within this range which turns out to be real and repeatable. The exact location and the height of this hump, however, could depend on the pressure level as is demonstrated in the following figures.

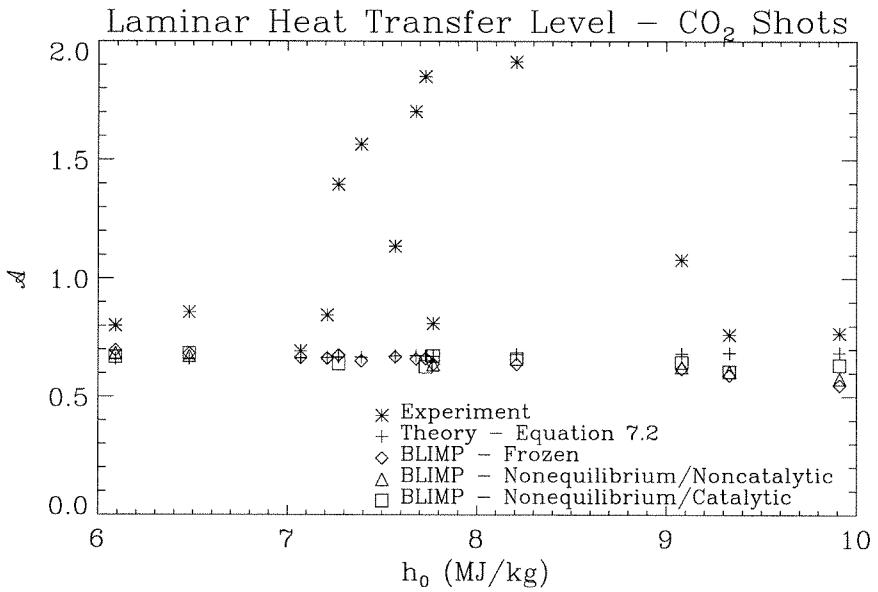

Figure 7.11: Computed, theoretical and experimental laminar heat transfer levels (CO_2 shots)

In Figure 7.12(a), only the experimental points from Figure 7.11 corresponding to 65 MPa $<$ P_0 $<$80 MPa are shown. The hump appears to peak around 8 MJ/kg and its width extends $\pm$ 1 MJ on either side. Over this range, the value of $\mathcal{A}$ reaches levels that are more than twice those computed with and without chemistry. In Figure 7.12(b), only the points for 40 MPa $<$ P_0 $<$55 MPa are shown. A hump is also evident although it is much narrower and centered around 7.5 MJ/kg. The values of $\mathcal{A}$ over the hump's extent are also up to twice the computed values.

No satisfactory interpretation of these observations can be given, the increase in heat transfer being too large to be explained solely by inaccurate modeling of the wall reactions. The phenomenon is nevertheless repeatable and seemingly germane to carbon dioxide. If the laminar heat transfer increase manifested by the hump does correspond in part to wall reactions, as suggested by the

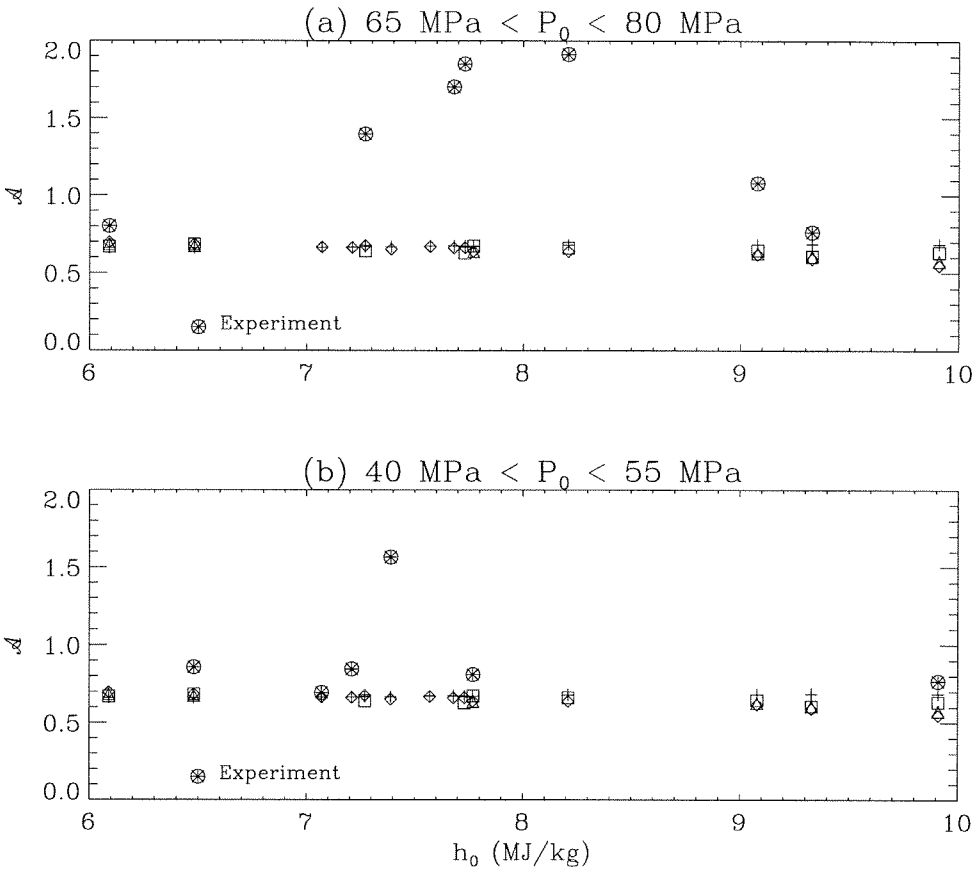

Figure 7.12: Experimental laminar heat transfer at different pressure levels (CO_2 shots) - (a) 65 MPa$< P_0 <$80 MPa, (b) 40 MPa$< P_0 <$55 MPa

smaller increases observed in the catalytic air computations (Figure 7.5), there is then an ever broader enthalpy range for such recombination reactions to occur as pressure increases. Certainly, the ranges of pressures and enthalpies explored are quite limited; however, one should keep in mind that it is sufficient to cover the important dissociative phenomena. In air, one has to worry about both oxygen and nitrogen dissociation as well as a host of other reactions within the range of enthalpies studied in the shock tunnel. It is relatively easier to achieve a state of "complete" dissociation at the enthalpies covered when it comes to carbon dioxide. The resulting product - carbon monoxide - remains undissociated in the enthalpy range studied.

7.2.3 Boundary layer profiles and chemistry

As with air, some insight into the chemistry might be gained by looking at the detailed inner structure of the boundary layers using the BLIMPK computations. Heat transfer levels are difficult to reproduce but one might nevertheless be able to compare qualitatively some of the features of

the carbon dioxide flows to their air counterparts. It should be pointed out that most differences between the experiments and the simulations are believed to come from the catalycity of the wall as well as from uncertainties in the gas-phase reactions and rates. This is supported by the fact that the air results clearly demonstrated at large enthalpies, that the heat transfer can be substantially larger with the inclusion of catalycity.

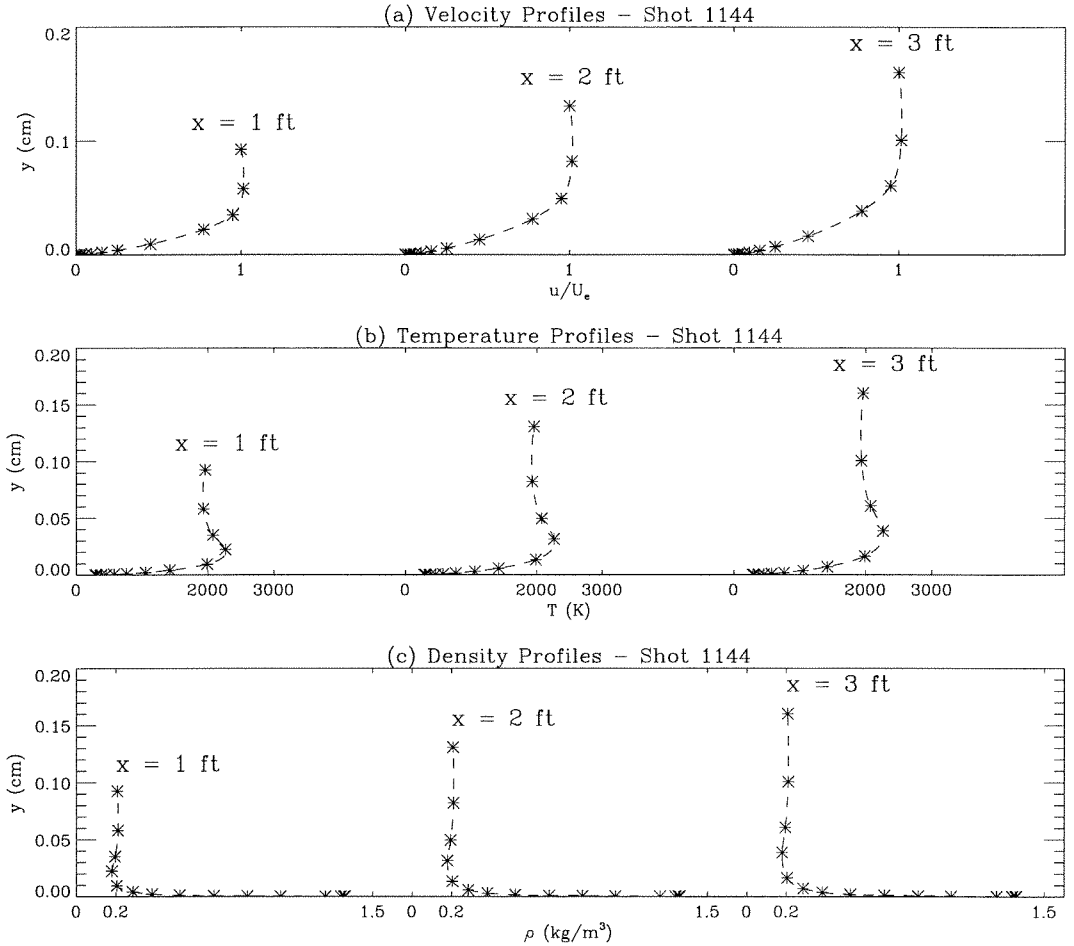

Figure 7.13: (a) Velocity, (b) temperature and (c) density profiles for shot 1144

Only one example is chosen for carbon dioxide, as opposed to the two chosen for air, since there are fewer reactions - CO_2 dissociation and the parallel O_2 formation - to track. The computations correspond to the shot shown earlier in Figure 7.10 with stagnation pressure $P_0 = 79.2$ MPa and stagnation enthalpy $h_0 = 9.1$ MJ/kg. The boundary layer is laminar over the entire model surface and velocity, temperature as well as density profiles at three streamwise stations are shown in Figures 7.13(a)-(c).

Nothing clearly sets these profiles apart from those obtained using air as a test gas. The velocity, temperature and density profiles are all characteristic of laminar compressible flows. A barely noticeable feature is that the maximum temperature point is less pronounced than in air. The profiles in Figure 7.13(a)-(c) were all obtained assuming frozen chemical compositions. The results with nonequilibrium chemistry, whether catalytic or noncatalytic, are virtually identical. A plot of the actual species concentrations across the boundary layer is shown in Figure 7.14.

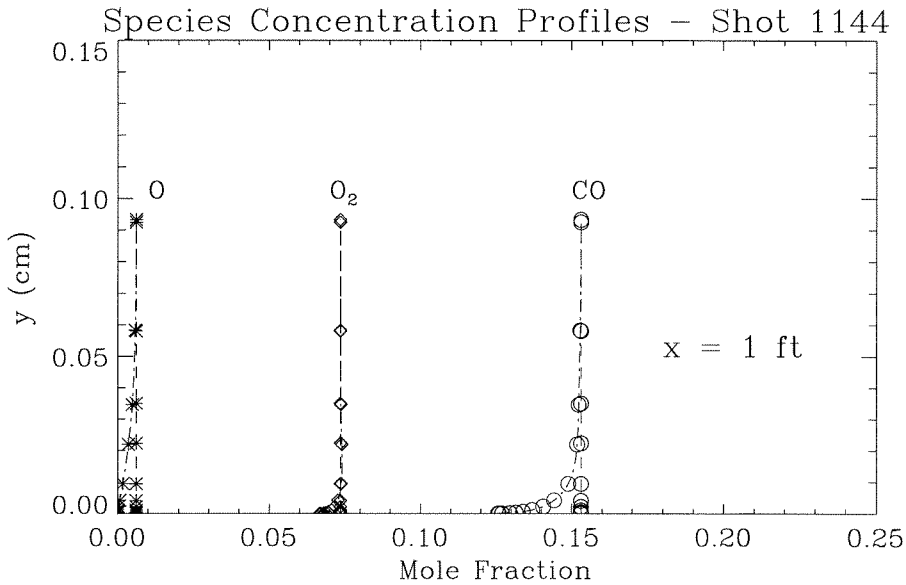

Figure 7.14: Nonequilibrium catalytic and noncatalytic concentration profiles at $x = 1$ ft for shot 1144. The vertical line for each species corresponds to the frozen edge compositions. The noncatalytic results are barely distinguishable from the catalytic levels.

Contrary to what the experiments indicate, the computations do not reveal very active chemical reactions in the boundary layer gas-phase or even at the wall. The nonequilibrium concentrations only differ from the frozen levels close to the wall where the temperature drops down rapidly and the catalytic results are indistinguishable from the noncatalytic ones. This is most probably due to the fact that even at the highest enthalpy investigated the temperatures within the boundary layer are quite low compared to those reached in the high enthalpy air shots. Furthermore, one should point out again that the reactions, both in the gas-phase and at the wall, are not as well understood in carbon dioxide as in air. It is therefore conceivable that key reactions may have been omitted that would otherwise account for some of the experimental observations.

7.3 Other gases

Other gases have been tested but are not discussed in the present study. In particular, nitrogen and helium shots had been performed by Germain [1994] as part of his exploratory boundary layer studies. Nitrogen shots are particularly useful since dissociation occurs at much higher enthalpies. Some ionization is also known to occur at extreme temperatures in the stagnation chamber. Helium on the other hand does not react at all and is more difficult to ionize. Combining these results with the air and carbon dioxide runs gives a wide range of flow conditions and possible dissociation scenarios which are certainly interesting as far as the heat transfer behavior with enthalpy is concerned. However, more important, is the role these conditions then play on the instability mechanisms in the laminar boundary layer and the resulting transition away from laminar behavior to turbulence.

Chapter 8 Conclusions

Experiments were conducted in the T5 shock tunnel at GALCIT to study enthalpy and chemistry effects on laminar and transitional hypervelocity boundary layers. CO_2 was the test gas used for most of the runs to further examine the trends previously observed by Germain [1994]. The model tested was a 5° half-angle cone measuring about a meter in length and was instrumented with 51 chromel-constantan coaxial thermocouples. Surface heat transfer rates were computed to deduce the state of the boundary layer and, when applicable, the transition location. The air transition results were compared with free flight data available at almost precisely the same conditions as the tunnel experiments. Finally, boundary layer profiles with various chemistry models were also computed and the heat transfer rate compared to the experimental measurements.

8.1 Enthalpy effects on transition

The transition results obtained strongly reinforce the observations by Germain[1994] that the stabilizing trend of the enthalpy increases as the characteristic dissociation energy of the gas decreases. This is brought out by the stronger rise of the reference transition Reynolds number Re^*_{tr} with reservoir enthalpy h_0 for CO_2 and the plateau Re^*_{tr} reaches in the range between complete CO_2 dissociation and before the beginning of CO dissociation. This stabilizing trend is consistent with second mode instabilities, acoustic waves being increasingly absorbed by the chemistry in the boundary layer as the enthalpy increases. Two attempts to correlate the transition data for all the gases - air, N_2 and CO_2 - are also quite successful.

8.2 Comparison with free flight data

The comparison of the tunnel transition data with free flight data illustrates clearly the need to compare such data on the basis of Reynolds numbers with gas properties evaluated at conditions more representative of the internal state of the boundary layer rather than in the freestream. The transition Reynolds numbers based on the boundary layer edge conditions are well over an order of magnitude higher in flight than in the T5 tunnel experiments. The transition Reynolds numbers based on reference conditions, however, are almost the same. The freestream temperatures and density are very different but their values inside the boundary layer are certainly much closer. All of these results suggest that the observation of Germain [1994] that the boundary layer transitions via the Tollmien-Schlichting mode, might need to be reconsidered.

8.3 Enthalpy effects on laminar heat transfer

Computations of boundary layer profiles in air indicate that there is a weak increase in the heat transfer rate due to chemical nonequilibrium. The difference is more pronounced as the enthalpy increases but remains under 30% over the range of conditions studied. Although the experimental results exhibit a relatively large scatter, they are nevertheless in broad agreement with the computed results using accepted gas phase and wall reaction rate data.

Effects of nonequilibrium chemistry on the laminar boundary layer heat flux are observed to be much larger in the CO_2 cases. An increase by a factor close to 2 occurs between reservoir enthalpies of 7 MJ/kg and 9 MJ/kg at values of P_0 between 65 MPa and 90 MPa. At lower pressures, P_0 between 40 MPa and 55 MPa, the enthalpy range over which the heat transfer increases is confined to a narrower range between 7 MJ/kg and 8 MJ/kg. This increase is not exhibited by the computations possibly because the model for the chemistry is incorrect.

8.4 Recommendations for future work

Laminar heat transfer, chemistry and transition

• While air chemistry is relatively well understood, the carbon dioxide computations were not as conclusive. In both cases, a better grasp of the wall catalycity is needed since nonequilibrium affects many of the fluid properties which in turn affect the transition process. The needed improvements can be achieved through computations as well as more tunnel experiments. Different chemistry wall reaction models, could be investigated using available nonequilibrium viscous codes. Parametric studies with variable rates and reactions should be able to isolate important effects on boundary layer development and the surface heat transfer levels. Experimentally, measurements of species or transport properties within the boundary are necessary. This should be done non-intrusively using, for example, techniques such as Laser-Induced Thermal Acoustics (Cummings [1995]).

• Along the same line, the heat transfer rise observed in the laminar carbon dioxide boundary layers needs to explained. Nonequilibrium computations in air indicate that full recombination at the wall increases, albeit weakly, the surface heat transfer rate. Since the carbon dioxide computations did not yield a similar result, it is possible that unaccounted gas-phase reactions, or surface reactions, and inaccurate rates could be the cause.

• Although the Re^*_{tr} versus h_e/h_0 data all seem to collapse on the same curve, none of the data for the different gases overlap. The nitrogen and air data are close together and trace out one

part of the curve and the carbon dioxide data then appear to smoothly prolong the curve. Air or nitrogen data at much lower enthalpies, as well as carbon dioxide at higher enthalpies, would confirm the trend. One should however note that at the lower h_0 values for, the boundary layer is turbulent over most of the thermocouples. At the opposite h_0 end for carbon dioxide, the boundary layer remains exclusively laminar making it impossible in either case to define a transition region.

• Expanding on the apparent stabilizing role of dissociation on transition, one should look at the equally important effect of ionization might have. High enthalpy nitrogen shots could be one way to obtain electrons although an equally suitable approach would be to use argon. Preliminary measurements, have already been made in T5 for argon shots over a wide range of enthalpies as high as 35 MJ/kg. An additional effect however, possibly competing with the ionization, appears at higher temperatures: while for most gases viscosity will increase with temperature there is a peak value, highly pressure dependent, for argon around 10,000 K. This is illustrated in Figure 8.1 below for equilibrium argon where one can also see the level of ionization at different temperatures.

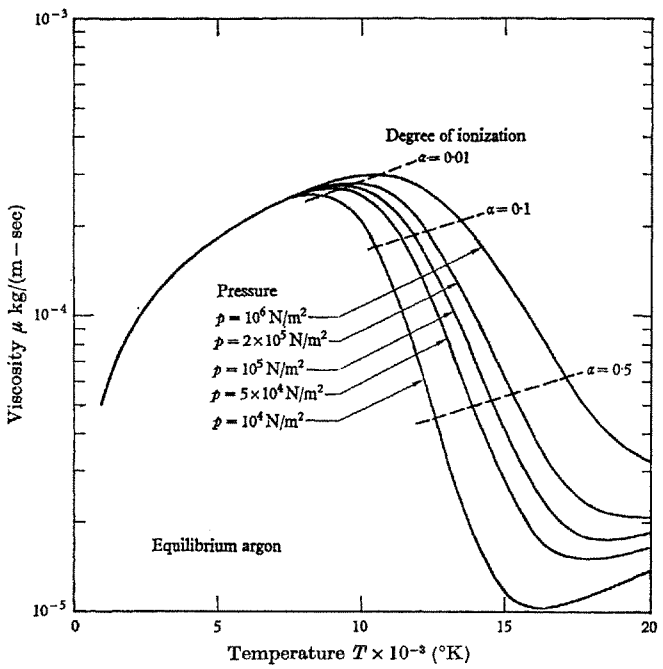

Figure 8.1: Equilibrium argon viscosity (Knöös [1968])

Stability of hypervelocity boundary layers

• Characterization of the freestream noise, both in spectra and disturbance level, is needed. The freestream, however, is not only a "hostile" environment when it comes to flow conditions such as

high temperature and particulates but also difficult for auxiliary instruments to access when test models are already present in the test section. One approach could be to instrument the nozzle wall with subsurface acoustic sensors capable of picking up the pressure fluctuations from the flow (Peckham and Winnicki [1979]).

• The sensors proposed above for the freestream noise characterization were actually developed to study hypersonic boundary layer transition (Demetriades [1978]). Designing sensors susceptible to frequencies on the order of a Megahertz and calibrating them for the expected pressure fluctuations associated with the acoustic second mode would be ideal to nonintrusively monitor the transition process. Only a few sensors, mounted under the skin of the model at strategic streamwise position, would be needed to track any wavelike feature within in the boundary layer.

• Exciting the boundary layer at presumed unstable frequencies would yield equally valuable information. This can be done using glow discharges similar to those developed by Kosinov *et al.* [1990] and currently being used in the Purdue quiet tunnel transition experiments by Schneider *et al.* [1994]. The instrument would have to be adapted to generate sufficiently high frequencies in order to reach the unstable second modes.

• Many linear stability analyses of hypersonic boundary layers have been done assuming the chemistry is frozen or, at most, in equilibrium. Recently the effect of thermochemical nonequilibrium on the stability has been addressed (Hudson *et al.* [1996]). It has been well known from the computations and few cold tunnel experiments that the higher frequency second mode is the most unstable at high Mach numbers. This does not, however, explain why the process observed by Germain [1994] in T5 seems to be of the Tollmien-Schlichting type. In fact, the result that the boundary layer is stabilized as the reservoir enthalpy is increased more likely to be consistent with second mode instabilities. Linear stability calculations of the present set of T5 experiments must therefore be carried out to elucidate these observations. Recent results of such calculations are shown in Figure 8.2 below. These calculations were performed with a thermochemical nonequilibrium linear stability code and an e^N transition criteria (Seipp [1997], Johnson [1997]). The agreement with the experiments is quite good as far as the increasing Re^*_{tr} trend with enthalpy is concerned. The computed Re^*_{tr} levels are higher than the experimental results but choosing a lower value of N could reduce the gap. The results also indicate that it is indeed the second mode that is responsible for transition in these boundary layers and that it is quite strongly stabilized by the nonequilibrium chemistry within the boundary layer.

• One final recommendation can be made, on a more theoretical and analytical level, concerning

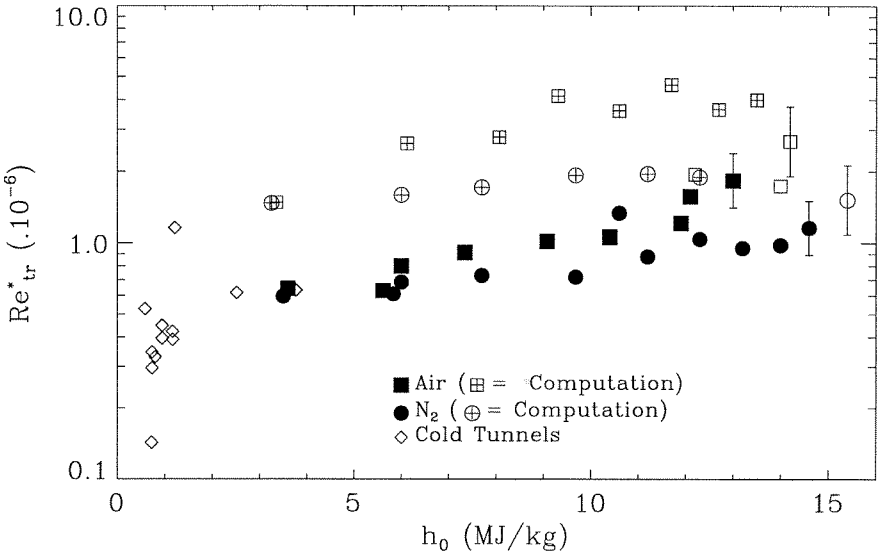

Figure 8.2: Experimental and e^N reference transition Reynolds numbers.

the above-mentioned stabilizing of the second mode. Since the mode is acoustic in nature, one could investigate how nonequilibrium chemistry affects these waves within the boundary layer. Of particular interest would be a study of the attenuation and absorption processes already known to occur as a result of the nonequilibrium dissociation and recombination reactions (Clarke and McChesney [1964], Becker [1966]).

Bibliography

ADAM, P. H., BLIMPK Simulations of Hypervelocity Boundary Layers, GALCIT Report FM 96-6, Graduate Aeronautical Laboratories, California Institute of Technology, Pasadena, California, August 1996

ANDERSON, J. D., Hypersonic and High Temperature Gas Dynamics, McGraw-Hill, New York, 1989

ANDERSON, J. D., Modern Compressible Flow, 2nd ed., McGraw-Hill, New York, 1990

BARTLETT, E. P. AND KENDALL, R. M., "An Analysis of the Coupled Chemically Reacting Boundary Layer and Charring Ablator, Part III," Nonsimilar Solution of the Multicomponent Laminar Boundary Layer by an Integral Matrix Method, Aerotherm Final Report 66-7, Part III, Aerotherm Corporation, March 1967 (also NASA CR-1062)

BECKER, E., Gasdynamik, B. G. Teubner Verlagsgesellschaft, Stuttgart, 1966

BERTIN, J. J., Hypersonic Aerothermodynamics, AIAA Education Series, Washington, DC, 1994

BLENSTRUP, G., BERSHADER, D. AND LANGHOFF, P., "Recent Results of Resonant Refractivity Studies for Improved Flow Visualization," Proceedings of the 12th International Symposium on Shock Tubes and Waves, Jerusalem, Israel, 1979

BLOTTNER, F. G., "Chemical Nonequilibrium Boundary Layer," *AIAA Journal*, vol. 2, no. 2, February 1964

BLOTTNER, F. G., "Nonequilibrium Laminar Boundary-Layer Flow of Ionized Air," *AIAA Journal*, vol. 2, no. 11, November 1964

BOUDREAU, A. H. AND SMITH III, V. K., Methodology of Hypersonic Testing, von Karman Institute Lecture Series 1993-03, February 1993

CANDLER, G. V., "The Computation of Weakly Ionized Hypersonic Flows in Thermochemical Nonequilibrium," Ph.D. Thesis, Stanford University, Stanford, California, 1988

CHEN, F.-J., MALIK, M. R. AND BECKWITH, I. E., "Boundary-Layer Transition on a Cone and a Flat Plate at Mach 3.5," *AIAA Journal*, vol. 27, June 1989, pp. 687-693

CHEN, Y.-K., HENLINE, W. D., STEWART, D. A. AND CANDLER, G. V., "Navier-Stokes Solutions with Surface Catalysis for Martian Atmospheric Entry," *AIAA Journal of Spacecraft and Rockets*, vol. 30, no. 1, January-February 1993

CLARKE, J. F. AND MCCHESNEY, M., The Dynamics of Real Gases, Butterworths, London, 1964

CRAWFORD, R., "Aerodynamic and Aerothermal Facilities II: Continuous Flow High Enthalpy Facilities," Methodology of Hypersonic Testing, von Karman Institute Lecture Series 1993-03, February 1993

CUMMINGS, E. B., "Laser-Induced Thermal Acoustics," Ph.D. Thesis, Graduate Aeronautical Laboratories, California Institute of Technology, Pasadena, California, 1995

DEFENSE SCIENCE BOARD, Report of the Defense Science Board Task Force on National Aero-Space Plane (NASP) Program, November 1992

DEMETRIADES, A., "An Experiment on the Stability of Hypersonic Laminar Boundary Layers," *Journal of Fluid Mechanics*, vol. 7, 1960

DEMETRIADES, A., "Laminar Boundary Layer Stability Measurements at Mach 7 Including Wall Temperature Effects," AFOSR-TR-77-1311, Air Force Office of Scientific Research, Washington, D.C., 1977

DEMETRIADES, A., Hypersonic Boundary Layer Transition as Detected with a Submerged Acoustic Sensor (Ground Test Report), Aeronutronic Division, Ford Aerospace & Communications Corp, Report No. U-6471, October 1978

DICRISTINA, V., "Three-Dimensional Laminar Boundary-Layer Transition on a Sharp 8° Cone at Mach 10," *AIAA Journal*, Vol. 8, May 1970, pp. 852-856

DORRANCE, W. H., Viscous Hypersonic Flow, McGraw-Hill, New York, 1962

DUSSAUGE, J.-P., FERNHOLZ, H., FINLEY, P. J., SMITH, R. W., SMITS, A. J. AND SPINA, E. F., Turbulent Boundary Layers in Subsonic and Supersonic Flow, AGARDograph No. 335, January 1995

EAST, R. A., STALKER, R. J. AND BAIRD, J. P., "Measurements of Heat Transfer to a Flat Plate in a Dissociated High-Enthalpy Laminar Air Flow," *Journal of Fluid Mechanics*, vol. 97, part 4, 1980

ECKERT, E. R. G., "Engineering Relations for Friction and Heat Transfer to Surfaces in High Velocity Flow," *Journal of the Aerospace Sciences*, vol. 22, 1955

ELENA, M. AND LACHARME, J.-P., "Experimental Study of a Supersonic Turbulent Boundary Layer Using a Laser Doppler Anemometer," *Journal de la Méchanique Théorique et Appliquée*, vol. 7, 1988

EVANS, R. M., JANAF Boundary Layer Integral Matrix Procedure, Aerotherm Final Report 75-152, Acurex Corporation, July 1975 (also NASA CR-143947)

FERRI, A., "Hypersonic Flight Testing," *International Science & Technology*, April 1964

GAI, S. L. AND JOE, W. S., "Laminar Heat Transfer to Blunt Cones in High-Enthalpy Hypervelocity Flows," *AIAA Journal of Thermophysics and Heat Transfer*, vol. 6, no. 3, July-September 1992

GERMAIN, P., "The Boundary Layer on a Sharp Cone in High-Enthalpy Flow," Ph.D. Thesis, Graduate Aeronautical Laboratories, California Institute of Technology, Pasadena, California, 1994

GERMAIN, P. D. AND HORNUNG, H. G., "Transition on a Slender Cone in Hypervelocity Flow," *Experiments in Fluids*, vol. 22, 1997

HE, Y. AND MORGAN, R. G., "Transition of Compressible High Enthalpy Boundary Layer Flow Over a Flat Plate," *Aeronautical Journal*, February 1994

HEPPENHEIMER, T. A., "Keepers of the Flame," *Air & Space*, December 1989/January 1990

HORNUNG, H. G., "Experimental Real-Gas Hypersonics," 28th Lanchester Memorial Lecture, *Aeronautical Journal*, December 1988

HORNUNG, H. G., Hypersonic Aerodynamics Class Notes, Graduate Aeronautical Laboratories, California Institute of Technology, Spring 1996

HORNUNG, H. G. AND BÉLANGER, J., "Role and Techniques of Ground Testing for Simulation of Flows up to Orbital Speed," AIAA Paper 90-1377, 16th Aerodynamic Ground Testing Conference, Seattle, Washington, June 1990

HUDSON, M. L., CHOKANI, N. AND CANDLER, G. V., "Linear Stability of Hypersonic Flow in Thermochemical Nonequilibrium," AIAA Paper 96-0671, 34th Aerospace Sciences Meeting & Exhibit, Reno, Nevada, January 1996

JOHNSON, C. B., STAINBACK, P. C., WICKER, K. C. AND BONEY, L. R., Boundary-Layer Edge Conditions and Transition Reynolds Number Data for a Flight Test at Mach 20 (Reentry F), NASA TM X-2584, July 1972

JOHNSON, H., Private communication, University of Minnesota, April 1997

KACHANOV, Y. S., "Physical Mechanisms of Laminar-Boundary-Layer Transition," *Annual Review of Fluid Mechanics*, vol. 26, 1994

KANDEBO, S. W., "Brown Calls for NASP Demonstrator," *Aviation Week & Space Technology*, July 5, 1993

KENDALL, J. M., "Supersonic Boundary Layer Stability Experiments," Boundary Layer Transition Study Group Meeting, Air Force Report no. BSD-TR-67-213, vol. II, August 1967

KNÖÖS, S., "Boundary-Layer Structure in a Shock-Generated Plasma Flow, Part 1. Analysis for equilibrium ionization," *Journal of Plasma Physics*, vol. 2, part 2, 1968

KOPPENWALLNER, G., "Hypersonic Aerothermodynamics," Fundamentals of Hypersonics: Aerodynamics and Heat Transfer, von Karman Institute Lecture Series 1984-01, February 1984

KOSINOV, A. D., MASLOV, A. A. AND SHEVELKOV, S. G., "Experiments on the Stability of Supersonic Laminar Boundary Layers," *Journal of Fluid Mechanics*, vol. 219, 1990

LACHOWICZ, J. T., CHOKANI, N. AND WILKINSON, S. P., "Boundary-Layer Stability Measurements in a Hypersonic Quiet Tunnel," *AIAA Journal*, vol. 34, no. 12, December 1996

LADERMAN, A. J. AND DEMETRIADES, A., "Mean and Fluctuating Flow Measurements in the Hypersonic Boundary Layer over a Cooled Wall," *Journal of Fluid Mechanics*, vol. 63, 1974

LAGERSTROM, P. A., Laminar Flow Theory, Princeton University Press, Princeton, NJ, 1964

LAUFER, J. AND VREBALOVICH, T., "Stability and Transition of a Supersonic Laminar Boundary Layer on an Insulated Flat Plate," *Journal of Fluid Mechanics*, vol. 9, 1960

LEES, L., "Laminar Heat Transfer Over Blunt-Nosed Bodies at Hypersonic Flight Speeds," *Jet Propulsion*, vol. 26, no. 4, April 1956

LIEPMANN, H. W. AND NOSENCHUCK, D. M., "Active Control of Laminar-Turbulent Transition," *Journal of Fluid Mechanics*, vol. 118, 1982

LORDI, J. A., MATES, R. E. AND MOSELLE, J. R., Computer Program for Solution of Nonequilibrium Expansions of Reacting Gas Mixtures, NASA CR-472, 1966

LYSENKO, V. I., "High-Speed Boundary-Layer Stability and Transition," *International Journal of Mechanical Sciences*, vol. 35, no. 11, 1993

MACK, L. M., An Experimental Investigation of the Temperature Recovery Factor, JPL Report 20-80, Jet Propulsion Laboratory, California Institute of Technology, Pasadena, California, 1954

MACK, L. M., Boundary-Layer Stability Theory, JPL Report 900-277 Rev. A, Jet Propulsion Laboratory, California Institute of Technology, Pasadena, California, November 1969

MACK, L. M., "Boundary-Layer Linear Stability Theory", Special Course on Stability and Transition of Laminar Flow, AGARD Report No. 709, March 1984

MALIK, M. R. AND ANDERSON, E. C., "Real Gas Effects on Hypersonic Boundary-Layer Stability," *Physics of Fluids A*, vol. 3, no. 5, May 1991

MALLINSON, S. G., GAI, S. L. AND MUDFORD, N. R., "The Boundary Layer on a Flat Plate in Hypervelocity Flow," *Aeronautical Journal*, April 1996

MCINTOSH, M. K., A Computer Program for the Numerical Calculation of Equilibrium and Perfect Gas Conditions in Shock Tunnels, Australian Defence Scientific Service, Technical Note CPD 169, Salisbury, South Australia, 1970

McMillin, B. K., Seitzman, J. M., Palmer, J. L. and Hanson, R. K., "Dual-Laser PLIF Imaging Techniques for Shock Tube Studies of Mixing and Combustion," Proceedings of the 19th International Symposium on Shock Waves, Marseille, France, July 1993

Miller, J. H., Tannehill, J. C., Wadawadigi, G., Edwards, T. A. and Lawrence, S. L., "Computation of Hypersonic Flows with Finite Catalytic Walls," *AIAA Journal of Thermophysics and Heat Transfer*, vol. 9, no. 3, July-September 1995

Morkovin, M. V., "Effects of Compressibility on Turbulent Flows," Méchanique de la Turbulence (A. Favre ed.), CNRS, Paris, France, 1962

Murray, A. L., Further Enhancements of the BLIMP Computer Code and User's Guide, Aerotherm Final Report 88-12/ATD, Acurex Corporation, June 1988 (also AFWAL TR-88-3010)

Owen, F. K. and Horstman, C. C., "On the Structure of Hypersonic Turbulent Boundary Layers," *Journal of Fluid Mechanics*, vol. 53, 1972

Owen, F. K., Horstman, C. C., Stainback, P. C. and Wagner, R. D., "Comparison of Wind Tunnel Transition and Freestream Disturbance Measurements," *AIAA Journal*, vol. 13, no. 3, June 1975

Park, C., Nonequilibrium Hypersonic Aerothermodynamics, Wiley Interscience, New York, 1990

Park, C., Howe, J. T., Jaffe, R. L. and Candler, G. V., "Review of Chemical-Kinetic Problems of Future NASA Missions, II: Mars Entries," *AIAA Journal of Thermophysics and Heat Transfer*, vol. 8, no. 1, January-March 1994

Pate, S. R., "Measurements and Correlations of Transition Reynolds Numbers on Sharp Slender Cones at High Speeds," *AIAA Journal*, vol. 9, no. 6, June 1971

Peckham, V. and Winnicki, R., Acoustic Transition Monitor Program Report, vol. I, BLAM Characterization and Development, Kaman Sciences Corporation, Report No. SAMSO-TR-79-9, January 1979

Reed, H. L. and Saric, W. S., "Linear Stability Theory Applied to Boundary Layers," *Annual Review of Fluid Mechanics*, vol. 28, 1996

Rein, M., SURF: A Program for Calculating Inviscid Supersonic Reacting Flows in Nozzles, GALCIT Report FM 89-1, Graduate Aeronautical Laboratories, California Institute of Technology, Pasadena, California, 1989

Reshotko, E., "Transition Reversal and Tollmien-Schlichting Instability," *Physics of Fluids*, vol. 6, no. 3, 1963

Reynolds, W. C., The Element Potential Method for Chemical Equilibrium Analysis: Implementation in the Interactive program STANJAN, Department of Mechanical Engineering Report, Stanford University, Stanford, California, 1986

ROSENHEAD, L., Laminar Boundary Layers, Clarendon Press, Oxford, 1963

ROUSSET, B., "Calibration and Study of the Contoured Nozzle of the T5 Free-Piston Hypervelocity Shock Tunnel," Engineer's Thesis, Graduate Aeronautical Laboratories, California Institute of Technology, Pasadena, California, 1995

SANDERSON, S. R., "Shock Wave Interaction in Hypervelocity Flow," Ph.D. Thesis, Graduate Aeronautical Laboratories, California Institute of Technology, Pasadena, California, 1995

SCHLICHTING, H., Boundary Layer Theory, 7nd ed., McGraw-Hill, New York, 1979

SCHNEIDER, S. P., HAVEN, C. E., MCGUIRE, J. B., COLLICOTT, S. H., LADOON, D. AND RANDALL, L. A., "High-Speed Laminar-Turbulent Transition Research in the Purdue Quiet-Flow Ludwieg Tube," AIAA Paper 94-2504, 18th Aerospace Ground Testing Conference, Colorado Springs, Colorado, June 1994

SCHNEIDER, S. P. AND HAVEN, C. E., "Quiet-Flow Ludwieg Tube for High-Speed Transition Research," *AIAA Journal*, vol. 33, no. 4, April 1995

SCHUBAUER, G. B. AND SKRAMSTAD, H. K., Laminar-Boundary-Layer Oscillations and Transition on a Flat Plate, NACA Report 909, 1948

SCHULTZ, D. L. AND JONES, T. V., Heat-transfer Measurements in Short-duration Hypersonic Facilities, AGARDograph No. 165, February 1973

SEIPP, T. G., "The Effect of Freestream Enthalpy on Hypersonic Boundary Layer Stability," Master's Thesis, Graduate School, University of Minnesota, February 1997

SKINNER, K. A., "Mass Spectrometry in Shock Tunnel Experiments of Hypersonic Combustion," Ph.D. Thesis, Department of Mechanical Engineering, University of Queensland, March 1994

SMITH, A.M.O. AND GAMBERONI, N., "Transition Pressure Gradient and Stability Theory," Douglas Aircraft Co. Report ES 26388, El Segundo, California, 1956

SMITH III, V. K., "Hypersonic Overview," Methodology of Hypersonic Testing, von Karman Institute Lecture Series 1993-03, February 1993

SPINA, E. F., SMITS, A. J. AND ROBINSON, S. K., "The Physics of Supersonic Turbulent Boundary Layers," *Annual Review of Fluid Mechanics*, vol. 26, 1994

SPINA, E. F. AND SMITS, A. J., "Organized Structures in a Compressible Turbulent Boundary Layer," *Journal of Fluid Mechanics*, vol. 182, 1987

STETSON, K. F. AND RUSHTON, G. H., "Shock Tunnel Investigation of Boundary-Layer Transition at M=5.5," *AIAA Journal*, vol. 5, no. 5, May 1967

STETSON, K. F. AND KIMMEL, R. L., "On Hypersonic Boundary-Layer Stability," AIAA Paper 92-0737, 30th Aerospace Sciences Meeting & Exhibit, Reno, Nevada, January 1992

STEWARTSON, K., The Theory of Laminar Boundary Layers in Compressible Fluids, Oxford University Press, London, 1964

STUCKERT, G. AND REED, H. L., "Linear Disturbances in Hypersonic, Chemically Reacting Shock Layers," *AIAA Journal*, vol. 32, no. 7, July 1994

SUDANI, N. AND HORNUNG, H. G., "Detection of Driver Gas Contamination in the T5 Hypervelocity Shock Tunnel," AIAA Paper 97-0561, 35th Aerospace Sciences Meeting & Exhibit, Reno, Nevada, January 1997

TAYLOR, G. I. AND MACCOLL, J. W., "The Air Pressure on a Cone Moving at High Speed," *Proceedings of the Royal Society of London*, ser. A, vol. 139, 1933

TONG, H., BUCKINGHAM, A. C. AND MORSE H. L., Nonequilibrium Chemistry Boundary Layer Integral Matrix Procedure, Aerotherm Final Report 73-67, Acurex Corporation, July 1973 (also NASA CR-134039)

VAN DRIEST, E. R., "Turbulent Boundary Layer on a Cone in Supersonic Flow at Zero Angle of Attack," *Journal of the Aerospace Sciences*, vol. 19, 1952

VAN DRIEST, E. R., "The Problem of Aerodynamic Heating," *Journal of the Aerospace Sciences*, vol. 23, 1956

VIDAL, R. J. AND GOLIAN, T. C., "Heat-Transfer Measurements with a Catalytic Flat Plate in Dissociated Oxygen," *AIAA Journal*, vol. 5, no. 9, September 1967

VINCENTI, W. G. AND KRUGER, C. H., Introduction to Physical Gas Dynamics, Wiley, New York, 1965

WEN, C.-Y. AND HORNUNG, H. G., "Non-Equilibrium Dissociating Flow over Spheres," *Journal of Fluid Mechanics*, vol. 299, 1995

WHITE, F. M., Viscous Fluid Flow, 2nd ed., McGraw-Hill, New York, 1991

WHITE, F. M. AND CHRISTOPH, G. H., "A Simple Theory for the Two-Dimensional Compressible Turbulent Boundary Layer," *Journal of Basic Engineering*, vol. 94, 1972

WRIGHT, R. L. AND ZOBY, E. V., "Flight Boundary Layer Transition Measurements on a Slender Cone at Mach 20," AIAA Paper 77-719, 10th Fluid & Plasmadynamics Conference, Albuquerque, New Mexico, June 1977

Appendix A Thermocouple Distribution

- A.1 Thermocouple Distribution for 1st Shot Series
- A.2 Thermocouple Distribution for 2nd Shot Series
- A.3 Thermocouple Distribution for 3rd Shot Series (Table and Figure)

A.1 Thermocouple Distribution for 1st Shot Series

i*	Thermocouple		x (cm)	θ (°)	R (Ω)
	No.	Type**			
0	1	M	24.1	90	61.0
1	2	M	26.0	80	58.0
2	3	M	29.8	70	57.0
3	4	M	31.8	110	57.0
4	5	M	34.3	60	36.0
5	6	M	38.1	120	47.0
6	7	M	44.5	50	36.0
7	8	M	48.3	130	36.0
8	9	M	53.3	40	40.0
9	10	M	58.4	140	39.0
10	11	M	66.0	30	31.0
11	12	M	73.7	150	36.0
12	13	M	81.3	20	28.0
13	14	M	88.9	160	29.0

* i is the thermocouple index for the arrays used in the PV-Wave data reduction/plotting routines

** M indicates a Medtherm thermocouple, S a Sanderson thermocouple

A.2 Thermocouple Distribution for 2nd Shot Series

i*	Thermocouple		x (cm)	θ (°)	R (Ω)
	No.	Type**			
0	1	M	24.1	90	59.8
1	2	M	26.0	80	xxx
2	3	M	29.8	70	56.4
3	4	M	31.8	110	56.6
4	5	M	34.3	60	36.8
5	6	M	38.1	120	84.5
6	7	S	41.3	90	66.3
7	8	M	44.5	50	36.6
8	9	M	48.3	130	37.0
9	10	S	50.8	90	58.6
10	11	M	53.3	40	38.6
11	12	M	58.4	140	34.5
12	13	S	62.2	90	57.2
13	14	M	66.0	30	31.7
14	15	S	69.8	90	xxx
15	16	M	73.7	150	35.6
16	17	S	73.7	90	51.7
17	18	M	81.3	20	28.9
18	19	M	88.9	160	30.0

* i is the thermocouple index for the arrays used in the PV-Wave data reduction/plotting routines

** M indicates a Medtherm thermocouple, S a Sanderson thermocouple

A.3 Thermocouple Distribution for 3rd Shot Series

i *	Thermocouple		x (cm)	θ (°)	R (Ω)	i	Thermocouple		x (cm)	θ (°)	R (Ω)
	No.	Type**					No.	Type**			
0	1	M	24.16	90	26.1	27	28	M	58.43	140	12.5
1	2	S	26.05	80	91.2		29	S	59.52	100	53.4
2	3	S	27.99	100	89.2	28	30	S	60.82	50	52.2
3	4	S	29.84	70	89.4	29	31	S	62.26	90	50.9
4	5	S	31.73	110	83.8	30	32	S	63.31	120	50.1
5	6	M	34.32	60	15.1	31	33	S	64.50	70	49.7
6	7	S	35.56	75	80.7	32	34	M	66.05	30	8.8
7	8	S	36.91	115	79.7		35	S	67.09	130	47.8
8	9	M	38.10	120	17.5	33	36	S	68.39	60	47.9
9	10	S	39.2	105	84.3	34	37	S	69.93	90	50.7
10	11	S	40.30	65	79.3	35	38	S	70.83	105	49.9
11	12	S	41.29	90	61.0	36	39	S	72.17	45	49.3
12	13	S	42.39	115	61.9		40	S	73.72	90	46.6
13	14	S	43.48	60	60.3	37	41	M	73.72	150	16.0
14	15	M	44.48	50	14.2	38	42	S	74.91	80	40.6
15	16	S	45.03	80	61.9	39	43	S	76.41	100	39.2
16	17	M	45.78	130	13.6	40	44	S	77.90	65	38.5
17	18	S	46.97	95	58.2	41	45	S	79.40	115	36.3
18	19	S	48.27	75	55.0	42	46	M	81.34	20	19.2
19	20	S	49.46	125	54.4	43	47	S	82.44	55	49.4
20	21	S	50.91	90	57.0	44	48	S	83.88	140	49.1
21	22	S	51.95	60	53.3	45	49	S	85.42	75	47.5
22	23	M	53.40	40	12.8	46	50	S	86.97	110	48.3
23	24	S	54.39	110	67.2	47	51	M	88.91	160	15.7
24	25	S	55.69	80	66.7		X1	S	34.37	95	83.6
25	26	S	56.93	65	65.8		X2	S	66.45	85	65.9
26	27	S	57.63	115	65.3						

* i is the thermocouple index for the arrays used in the PV-Wave data reduction/plotting routines

** M indicates a Medtherm thermocouple, S a Sanderson thermocouple

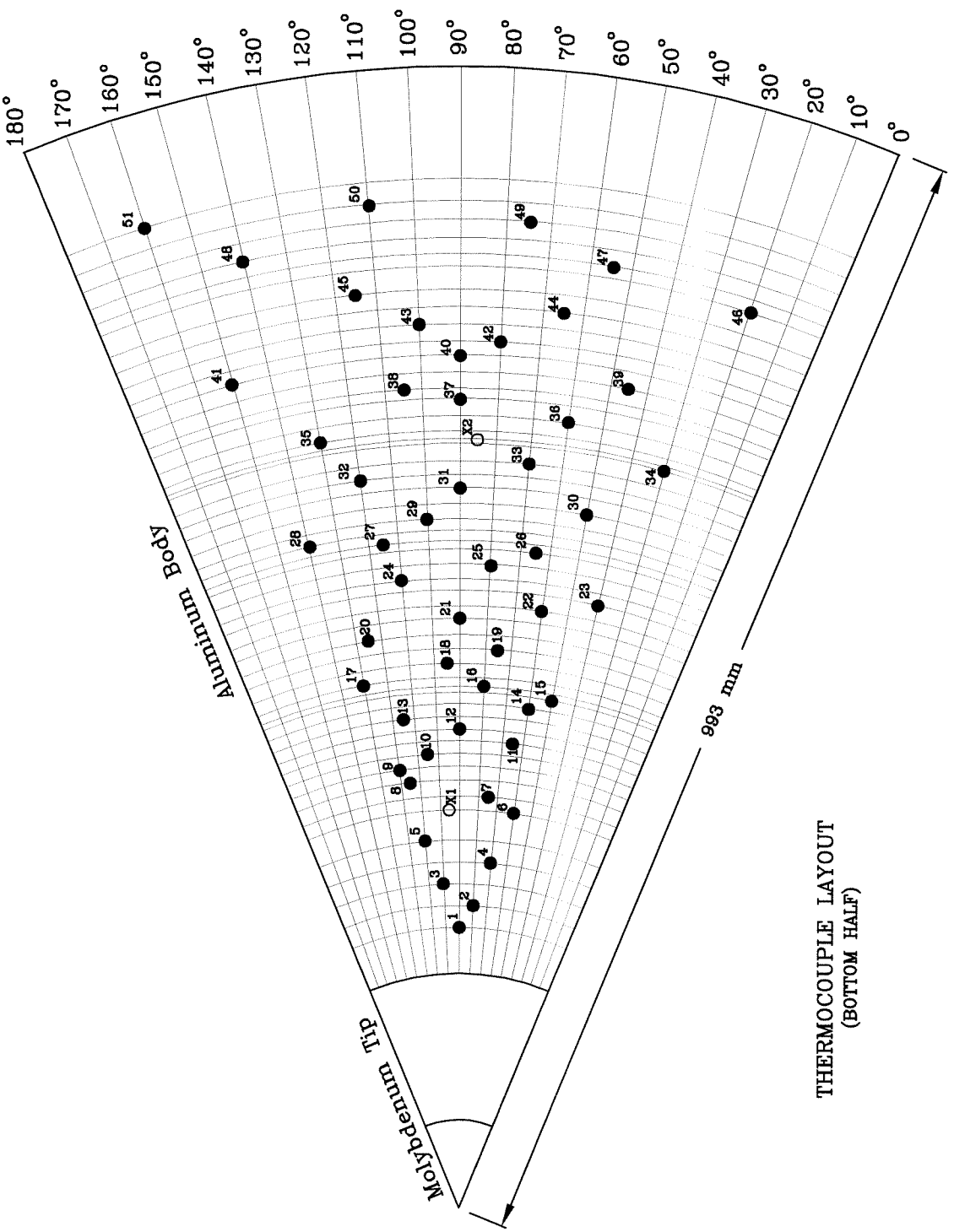

Figure A.1: Model Geometry, Material and Instrumentation Layout

Appendix B Shot Summary

B.1 Summary of Conditions for 1st Shot Series

Shot	Gas	P_0 (MPa)	h_0 (MJ/kg)	L/Tr/T	Photo
671	Air	78.6	21.3	L	Yes
672	Air	82.2	27.0	L	Yes
673	Air	84.4	26.7	L	Yes
674	Air	76.0	25.4	L	Yes
675	Air	58.5	10.5	L/Tr	Yes
676	Air	56.7	10.6	xxx	Yes
677	Air	60.5	18.0	L	Yes
678	Air	60.8	18.5	L/Tr	Yes
679	Air	61.0	22.5	L	Yes
680	Air	63.5	18.4	L	Yes
681	Air	62.6	18.6	L	Yes
682	Air	59.6	17.8	L/Tr	Yes
683	Air	65.5	10.7	L/Tr	Yes
684	Air	60.9	11.4	L/Tr	Yes
685	Air	56.9	10.6	L/Tr	Yes
686	Air	55.4	12.7	L/Tr	Yes
687	Air	57.3	13.3	L/Tr	Yes
688	Air	62.3	13.5	L/Tr	Yes
689	Air	59.0	10.9	L/Tr	Yes
690	CO_2	52.0	7.07	L/Tr	Yes

B.2 Summary of Conditions for 2nd Shot Series

Shot	Gas	P_0 (MPa)	h_0 (MJ/kg)	L/Tr/T	Photo
873	Air	xxx	xxx	xxx	xxx
874	Air	68.2	14.8	L	No
875	Air	70.3	15.0	L	No
876	Air	58.9	17.4	L	Yes
877	Air	59.1	19.8	L	Yes
878	Air	59.9	19.9	L	Yes
879	Air	79.1	11.9	L/Tr	Yes
880	Air	60.6	20.4	L	Yes
881	Air	59.4	20.6	L	Yes
882	Air	68.1	15.2	L	Yes
883	Air	69.4	14.8	L	Yes
884	Air	61.8	20.2	L	Yes
885	Air	60.9	20.2	L	Yes
886	Air	61.5	17.7	L	Yes
887	Air	66.8	14.3	L	Yes
888	Air	79.1	11.8	L/Tr	Yes

B.3 Summary of Conditions for 3rd Shot Series

Shot	Gas	P_0 (MPa)	h_0 (MJ/kg)	L/Tr/T	dsp 4012 ch 4	dsp 2612 ch 1	dsp 2612 ch 2	Photo	CCD
1113	Air	77.2	11.6	L/Tr	Diode	-	-	No	No
1114	Air	83.2	9.85	L	Diode	-	Diode	No	No
1115	Air	68.7	7.65	L/Tr	Diode	-	Diode	Yes	No
1116	CO_2	86.2	7.96	Tr/T	Diode	-	Diode	Yes	No
1117	CO_2	92.9	7.57	L/Tr	Diode	-	Diode	Yes	No
1118	CO_2	85.8	5.31	Tr/T	Diode	-	Diode	Yes	No
1119	CO_2	71.6	9.33	L/Tr	Diode	-	Diode	Yes	No
1120	CO_2	72.0	3.91	T	Diode	-	Diode	Yes	No
1121	CO_2	40.8	9.91	L	Diode	-	Diode	Yes	No
1122	CO_2	47.1	7.77	L	Diode	-	Diode	No	No
1123	CO_2	55.2	6.48	L/Tr	Diode	-	Diode	No	No
1124	CO_2	61.5	6.09	Tr	Diode	-	Diode	Yes	No
1125	CO_2	61.2	4.64	Tr/T	Diode	-	Diode	Yes	No
1126	CO_2	62.2	4.55	Tr/T	Diode	-	Diode	Yes	No
1127	CO_2	53.3	7.21	L	Diode	-	Diode	No	No
1128	CO_2	xx.x	xx.x	xxx	xxx	xxx	xxx	Yes	No
1129	CO_2	48.1	3.21	Tr/T	-	-	-	Yes	No
1130	CO_2	49.1	5.29	L/Tr	-	-	-	No	No
1131	CO_2	49.9	6.34	L/Tr	-	-	-	Yes	No
1132	CO_2	52.3	7.74	L/Tr	-	-	-	No	No
1133	CO_2	48.2	5.24	Tr/T	-	-	-	No	No
1134	CO_2	48.3	4.48	Tr/T	-	-	-	Yes	No
1135	CO_2	48.1	3.78	T	-	-	-	Yes	No
1136	CO_2	60.4	5.86	L/Tr	-	-	-	Yes	No
1137	CO_2	82.1	7.27	L	-	-	-	Yes	No
1138	CO_2	79.5	8.21	L	-	-	-	Yes	No
1139	CO_2	81.4	7.73	L	-	-	-	No	No
1140	CO_2	82.0	7.68	L	-	-	-	No	No

Summary of Conditions for 3rd Shot Series (cont.)

Shot	Gas	P_0 (MPa)	h_0 (MJ/kg)	L/Tr/T	dsp 4012 ch 4	dsp 2612 ch 1	dsp 2612 ch 2	Photo	CCD
1141	CO_2	83.3	5.46	Tr/T	Diode*	-	-	No	No
1142	CO_2	77.4	5.30	T	Diode*	-	-	No	No
1143	CO_2	83.0	6.01	Tr	Diode*	-	-	No	No
1144	CO_2	79.2	9.08	L	Diode*	-	-	No	No
1145	CO_2	83.5	4.43	T	-	-	-	No	No
1146	CO_2	81.9	6.63	L/Tr	Diode	-	-	No	No
1147	CO_2	44.9	7.39	L	Diode	-	-	No	No
1148	CO_2	44.2	5.87	L/Tr	Diode	-	-	No	No
1149	CO_2	44.5	5.06	L/Tr	Diode	-	-	No	No
1150	CO_2	43.8	3.96	Tr/T	Diode	-	-	No	No
1151	Air	45.0	10.3	L/Tr	Diode	-	-	No	No
1152	Air	43.3	9.16	Tr	Diode	-	-	No	No
1153	Air	40.7	12.5	L	-	-	-	No	No
1154	Air	37.5	14.2	L	-	-	-	No	No
1155	Air	44.3	8.35	L/Tr	-	-	-	No	No
1156	Air	48.0	8.07	Tr/T	-	-	-	No	No
1157	Air	47.2	6.12	Tr/T	-	-	-	No	No
1158	Air	36.6	16.1	L	-	-	-	No	No
1159	Air	42.5	11.7	L/Tr	-	X1	X2	No	Yes
1160	Air	41.9	10.7	L/Tr	-	X1	X2	No	Yes
1161	Air	33.8	14.1	L	Trigger	X1	X2	No	Yes
1162	Air	34.4	9.31	L/Tr	Pulse	Trigger	-	No	Yes
1163	Air	68.1	11.4	L/Tr	-	X1	X2	No	Yes
1164	Air	56.2	14.6	L	-	X1	X2	No	Yes

* Photodiode for soot detection/driver gas contamination experiment

Appendix C Transition Parameters

C.1 Transition Parameters for 1st Shot Series

Shot	Gas	P_0 (MPa)	h_0 (MJ/kg)	Re/L (x10^6 m^{-1})	Re_{tr} (x10^6)	Re^*_{tr} (x10^6)	Comments
671	Air	78.6	21.3	3.51			Laminar
672	Air	82.2	27.0	2.79			Laminar
673	Air	84.4	26.7	2.91			Laminar
674	Air	76.0	25.4	2.82			Laminar
675	Air	58.5	10.5	5.50	2.94	1.39	
676	Air	56.7	10.6	xxx	x.xx	x.xx	
677	Air	60.5	18.0	3.22			Laminar
678	Air	60.8	18.5	3.17			Lam/Tr
679	Air	61.0	22.5	2.66			Laminar
680	Air	63.5	18.4	3.30			Laminar
681	Air	62.6	18.6	3.23			Laminar
682	Air	59.6	17.8	3.21			Laminar
683	Air	65.5	10.7	5.97	2.44	1.16	
684	Air	60.9	11.4	5.19	2.38	1.15	
685	Air	56.9	10.6	5.29	2.27	1.02	
686	Air	55.4	12.7	4.18	2.48	1.22	
687	Air	57.3	13.3	4.12	2.44	1.21	
688	Air	62.3	13.5	4.37	2.71	1.35	
689	Air	59.0	10.9	5.27	2.82	1.34	
690	CO_2	52.0	7.07	7.05	3.42	4.66	

C.2 Transition Parameters for 2nd Shot Series

Shot	Gas	P_0 (MPa)	h_0 (MJ/kg)	Re/L (x10^6 m^{-1})	Re_{tr} (x10^6)	Re^*_{tr} (x10^6)	Comments
873	Air	xxx	xxx	xxx			
874	Air	68.2	14.8	4.33			Laminar
875	Air	70.3	15.0	4.38			Laminar
876	Air	58.9	17.4	3.25			Laminar
877	Air	59.1	19.8	2.90			Laminar
878	Air	59.9	19.9	2.93			Laminar
879	Air	79.1	11.9	6.28	3.05	1.50	
880	Air	60.6	20.4	2.89			Laminar
881	Air	59.4	20.6	2.82			Laminar
882	Air	68.1	15.2	4.20			Laminar
883	Air	69.4	14.8	4.38			Laminar
884	Air	61.8	20.2	2.97			Laminar
885	Air	60.9	20.2	3.04			Laminar
886	Air	61.5	17.7	3.45			Laminar
887	Air	66.8	14.3	4.56			Laminar
888	Air	79.1	11.8	6.63	4.20	2.20	

C.3 Transition Parameters for 3rd Shot Series

Shot	Gas	P_0 (MPa)	h_0 (MJ/kg)	Re/L (x10^6 m^{-1})	Re_{tr} (x10^6)	Re^*_{tr} (x10^6)	Comments
1113	Air	77.2	11.6	6.31	3.03	1.48	
1114	Air	83.2	9.85	8.31			Laminar
1115	Air	68.7	7.65	9.31	4.04	1.66	
1116	CO_2	86.2	7.96	9.85	3.69	6.53	*
1117	CO_2	92.9	7.57	11.0	5.01	8.06	
1118	CO_2	85.8	5.31	16.4	5.33	6.13	*
1119	CO_2	71.6	9.33	7.13	3.26	6.85	
1120	CO_2	72.0	3.91	19.9	2.03	1.96	*
1121	CO_2	40.8	9.91	4.04	2.54	5.40	
1122	CO_2	47.1	7.77	5.76			Laminar
1123	CO_2	55.2	6.48	8.35	3.80	4.84	
1124	CO_2	61.5	6.09	10.0	3.86	4.74	
1125	CO_2	61.2	4.64	14.1	5.04	5.29	
1126	CO_2	62.2	4.55	14.7	5.40	5.59	
1127	CO_2	53.3	7.21	7.04			Laminar
1128	CO_2	xx.x	xx.x	xxx	xxx	xxx	
1129	CO_2	48.1	3.21	13.8	4.01	3.52	*
1130	CO_2	49.1	5.29	9.66	4.10	4.63	
1131	CO_2	49.9	6.34	7.81	3.34	4.17	
1132	CO_2	52.3	7.74	6.37	2.65	4.18	
1133	CO_2	48.2	5.24	9.61	3.53	3.96	
1134	CO_2	48.3	4.48	11.7	2.54	2.59	*
1135	CO_2	48.1	3.78	13.2			Turbulent
1136	CO_2	60.4	5.86	10.4	4.39	5.28	
1137	CO_2	82.1	7.27	10.4			Laminar
1138	CO_2	79.5	8.21	8.85			Laminar

* These values of Re_{tr} are for boundary layers that are almost fully laminar but show signs of transition.

Transition Parameters for 3rd Shot Series (cont.)

Shot	Gas	P_0 (MPa)	h_0 (MJ/kg)	Re/L (x10^6 m^{-1})	Re_{tr} (x10^6)	Re^*_{tr} (x10^6)	Comments
1139	CO_2	81.4	7.73	9.74			Laminar
1140	CO_2	82.0	7.68	9.77			Laminar
1141	CO_2	83.3	5.46	15.4			Turbulent
1142	CO_2	77.4	5.30	14.2			Turbulent
1143	CO_2	83.0	6.01	13.5	5.91	7.31	*
1144	CO_2	79.2	9.08	8.31			Laminar
1145	CO_2	83.5	4.43	20.2			Turbulent
1146	CO_2	81.9	6.63	11.7	5.25	6.92	*
1147	CO_2	44.9	7.39	5.84			Laminar
1148	CO_2	44.2	5.87	7.68	3.44	4.09	
1149	CO_2	44.5	5.06	9.30	4.34	4.76	
1150	CO_2	43.8	3.96	12.4	3.04	2.85	*
1151	Air	45.0	10.3	4.37	2.51	1.17	
1152	Air	43.3	9.16	4.84	1.91	0.854	
1153	Air	40.7	12.5	3.23	2.33	1.13	*
1154	Air	37.5	14.2	2.63			Laminar
1155	Air	44.3	8.35	5.43	2.46	1.05	
1156	Air	48.0	8.07	6.11	2.39	1.00	
1157	Air	47.2	6.12	8.69	1.98	0.735	
1158	Air	36.6	16.1	2.30			Laminar
1159	Air	42.5	11.7	3.60	2.59	1.24	
1160	Air	41.9	10.7	3.92	2.57	1.21	
1161	Air	33.8	14.1	2.42			Laminar
1162	Air	34.4	9.31	3.81	2.30	1.03	
1163	Air	68.1	11.4	5.72	3.36	1.63	
1164	Air	56.2	14.6	3.69			Laminar

* These values of Re_{tr} are for boundary layers that are almost fully laminar but show signs of transition.

C.4 Transition Parameters at T_{max} - Air Shots

Shot	T_e (K)	T^* (K)	T_{max} (K)	ρ_e (kg/m^3)	μ_ex10^5 (Ns/m^2)	ρ_{T_m} (kg/m^3)	μ_{T_m}x10^5 (Ns/m^2)	h_{T_m} (MJ/kg)	$Re_{tr_{T_m}}$ (x10^6)
675	1740	2712	2511	.07856	6.011	.05380	7.036	3.085	1.720
683	1794	2778	2570	.08599	6.137	.05935	7.125	3.157	1.451
684	1908	2925	2732	.07574	6.400	.05285	7.220	3.325	1.472
685	1758	2734	2531	.07568	6.052	.05198	7.067	3.132	1.335
686	2124	3213	2946	.06221	6.892	.04441	7.666	3.984	1.592
687	2220	3341	3155	.06177	7.110	.04377	7.951	4.057	1.546
688	2271	3405	3108	.06600	7.224	.04777	7.888	4.266	1.796
689	1824	2818	2605	.07618	6.207	.05279	7.176	3.257	1.690
879	2038	3088	2840	.09361	6.701	.06648	7.517	3.591	1.931
888	2100	3066	2884	.10250	6.842	.07385	7.578	3.591	2.732
1113	1986	3022	2782	.09340	6.582	.06599	7.435	3.493	1.895
1115	1177	2001	1864	.11930	4.629	.07433	5.983	2.055	1.947
1151	1686	2642	2446	.06170	5.881	.04205	6.937	3.062	1.450
1152	1472	2371	2199	.06610	5.368	.04369	6.550	2.628	1.035
1153	2013	3081	2837	.04710	6.639	.03307	7.514	3.945	1.445
1155	1305	2167	2015	.07140	4.954	.04569	6.243	2.323	1.249
1156	1255	2104	1954	.07970	4.828	.05046	6.140	2.219	1.190
1157	881	1602	1489	.10320	3.839	.06016	5.280	1.567	0.839
1159	1904	2931	2705	.05210	6.389	.03629	7.323	3.614	1.574
1160	1742	2718	2518	.05570	6.012	.03811	7.046	3.222	1.500
1162	1484	2387	2216	.05200	5.395	.03439	6.577	2.719	1.248
1163	1935	2958	2725	.08400	6.464	.05899	7.351	3.434	2.075

C.5 Transition Parameters at T_{max} - CO_2 Shots

Shot	T_e (K)	T^* (K)	T_{max} (K)	ρ_e (kg/m^3)	μ_ex10^5 (Ns/m^2)	ρ_{T_m} (kg/m^3)	μ_{T_m}x10^5 (Ns/m^2)	h_{T_m} (MJ/kg)	$Re_{tr_{T_m}}$ (x10^6)
690	1930	1617	2102	.1340	5.537	.1222	6.445	2.800	2.679
1116	2254	1625	2184	.1997	6.230	.2047	6.594	2.996	3.574
1117	2165	1650	2192	.2202	6.030	.2161	6.608	2.875	4.487
1118	1441	1332	1735	.2769	4.397	.2280	5.736	1.854	3.364
1119	2463	1611	2176	.1468	6.730	.1652	6.579	3.583	3.753
1120	1042	1071	1364	.2933	3.417	.2217	4.928	1.223	1.064
1121	2402	1559	2096	.0812	6.673	.0924	6.435	3.982	2.997
1123	1760	1535	1990	.1527	5.149	.1341	6.235	2.493	2.756
1124	1653	1468	1907	.1786	5.530	.1536	6.079	2.274	3.020
1125	1221	1189	1550	.2220	3.870	.1732	5.347	1.552	2.846
1126	1196	1174	1529	.2290	3.810	.1775	5.302	1.512	3.008
1129	1002	1077	1287	.2010	3.316	.1547	4.749	1.137	2.155
1130	1399	1307	1703	.1607	4.306	.1309	5.670	1.882	2.536
1131	1706	1505	1951	.1409	5.029	.1224	6.162	2.432	2.368
1132	2112	1626	2155	.1256	5.946	.1224	6.541	3.052	2.348
1133	1385	1296	1690	.1591	4.271	.1292	5.644	1.859	2.169
1134	1167	1154	1504	.1807	3.736	.1389	5.246	1.493	1.390
1136	1582	1424	1852	.1812	4.735	.1536	5.970	2.155	2.952
1143	1656	1468	1909	.2420	4.900	.2084	6.080	2.204	4.102
1146	1854	1583	2055	.2201	5.349	.1970	6.359	2.521	3.953
1148	1557	1411	1834	.1334	4.685	.1124	5.934	2.192	2.288
1149	1327	1260	1642	.1513	4.133	.1213	5.544	1.775	2.594
1150	1015	1053	1367	.1813	3.350	.1331	4.937	1.258	1.514

C.6 Transition Parameters at T_{max} - Germain Air Shots

Shot	T_e (K)	T^* (K)	T_{max} (K)	ρ_e (kg/m^3)	μ_ex10^5 (Ns/m^2)	ρ_{T_m} (kg/m^3)	μ_{T_m}x10^5 (Ns/m^2)	h_{T_m} (MJ/kg)	$Re_{tr_{T_m}}$ (x10^6)
362	450	1110	1419	.0565	2.483	.0177	5.137	1.491	0.472
537	2019	3110	3147	.0558	6.224	.0354	7.940	4.413	1.656
541	700	1650	1662	.0873	3.335	.0362	5.614	1.811	0.815
543	313	820	952	.0468	1.905	.0151	4.079	0.940	0.411
547	431	1070	1345	.0498	2.409	.0158	4.983	1.402	0.380
549	1120	2090	2089	.0698	4.446	.0372	6.368	2.388	0.964
553	1749	2780	2795	.0576	5.746	.0355	7.453	3.709	1.853
554	1640	2680	2780	.0594	5.542	.0350	7.432	3.444	1.076
560	1370	2380	2376	.0669	4.998	.0381	6.830	2.924	1.013
562	1737	2800	2804	.0894	5.724	.0549	7.466	3.542	1.516
564	1933	3010	3019	.0835	6.076	.0528	7.767	3.933	1.761
566	2136	3215	3262	.0780	6.420	.0506	8.092	4.413	2.573

C.7 Transition Parameters at T_{max} - Germain N_2 Shots

Shot	T_e (K)	T^* (K)	T_{max} (K)	ρ_e (kg/m^3)	μ_ex10^5 (Ns/m^2)	ρ_{T_m} (kg/m^3)	μ_{T_m}x10^5 (Ns/m^2)	h_{T_m} (MJ/kg)	$Re_{tr_{T_m}}$ (x10^6)
353	1240	2470	2334	.0656	4.713	.0346	6.764	2.477	1.121
361	510	1240	1435	.0482	2.704	.0169	5.170	1.317	0.479
532	1300	2550	2464	.0560	4.849	.0294	6.965	2.666	0.881
535	2090	3430	3434	.0458	6.344	.0281	8.316	4.336	1.498
536	1810	3150	3114	.0529	5.865	.0309	7.894	3.716	0.976
540	730	1710	1745	.0781	3.437	.0326	5.767	7.377	0.654
542	310	810	961	.0441	1.877	.0139	4.098	0.746	0.368
546	490	1200	1404	.0417	2.653	.0146	5.106	1.278	0.426
548	1030	2180	2113	.0628	4.232	.0305	6.408	2.172	0.712
561	1460	2780	2704	.0796	5.180	.0427	7.322	3.015	1.036
563	1630	2980	2922	.0757	5.523	.0421	7.632	3.341	0.946
565	1960	3310	3275	.0674	6.126	.0405	8.110	3.933	1.157

Appendix D Gas Phase and Surface Reactions

The rate constants in these tables have been taken from the following papers:

- Tong *et al.* [1973]
- Chen *et al.* [1993]
- Park *et al.* [1994]

D.1 Air Reactions

Gas Phase Reactions, $k_f = C_f T^{\eta_f} \exp(-\theta_f/T)$ $cm^3mole^{-1}s^{-1}$ or $cm^6mole^{-2}s^{-1}$

REACTION	BLIMP Kinetics			Park Kinetics			McKenzie Kinetics		
	C_f	η_f	θ_f	C_f	η_f	θ_f	C_f	η_f	θ_f
$O_2 + N \rightarrow$ 2 O + N	3.61e18	-1.0	59,400	1.0e22	-1.5	59,750	9.05e18	-1.0	59,370
$O_2 + O \rightarrow$ 2 O + O	90.25e18	-1.0	59,400	1.0e22	-1.5	59,750	9.05e18	-1.0	59,370
$O_2 + NO \rightarrow$ 2 O + NO	3.61e18	-1.0	59,400	2.0e21	-1.5	59,750	9.05e18	-1.0	59,370
$O_2 + O_2 \rightarrow$ 2 O + O_2	32.5e18	-1.0	59,400	2.0e21	-1.5	59,750	9.05e18	-1.0	59,370
$O_2 + N_2 \rightarrow$ 2 O + N_2	7.22e18	-1.0	59,400	2.0e21	-1.5	59,750	9.05e18	-1.0	59,370
$N_2 + O \rightarrow$ 2 N + O	1.92e17	-0.5	113,100	3.0e22	-1.6	113,200	2.46e19	-1.0	113,200
$N_2 + NO \rightarrow$ 2 N + NO	1.92e17	-0.5	113,100	7.0e21	-1.6	113,200	2.46e19	-1.0	113,200
$N_2 + O_2 \rightarrow$ 2 N + O_2	1.92e17	-0.5	113,100	7.0e21	-1.6	113,200	2.46e19	-1.0	113,200
$N_2 + N_2 \rightarrow$ 2 N + N_2	4.80e17	-0.5	113,100	7.0e21	-1.6	113,200	2.46e19	-1.0	113,200
$N_2 + N \rightarrow$ 2 N + N	4.15e22	-1.5	113,100	3.0e22	-1.6	113,200	2.46e19	-1.0	113,200
$NO + N \rightarrow$ N + O + N	79.4e20	-1.5	76,500	1.1e17	0.0	75,500	4.09e18	-1.0	75,330
$NO + O \rightarrow$ N + O + O	79.4e20	-1.5	76,500	1.1e17	0.0	75,500	4.09e18	-1.0	75,330
$NO + NO \rightarrow$ N + O + NO	79.4e20	-1.5	76,500	1.1e17	0.0	75,500	4.09e18	-1.0	75,330
$NO + O_2 \rightarrow$ N + O + O_2	3.97e20	-1.5	76,500	5.0e15	0.0	75,500	4.09e18	-1.0	75,330
$NO + N_2 \rightarrow$ N + O + N_2	3.97e20	-1.5	76,500	5.0e15	0.0	75,500	4.09e18	-1.0	75,330
$NO + O \rightarrow$ O_2 + N	3.18e9	1.0	19,700	8.4e12	0.0	19,450	2.98e11	0.5	19,460
$N_2 + O \rightarrow$ NO + N	6.75e13	0.0	37,500	6.4e17	-1.0	38,370	7.35e11	0.5	37,940

Air Reactions (cont.)

Surface Reactions

REACTION	Fully Catalytic Wall	Noncatalytic Wall
$O \rightarrow \frac{1}{2} O_2$	1e6	1e-6
$N \rightarrow \frac{1}{2} N_2$	1e6	1e-6
$NO \rightarrow \frac{1}{2} O_2 + \frac{1}{2} N_2$	1e6	1e-6

D.2 CO_2 Reactions

Gas Phase Reactions, $k_f = C_f T^{\eta_f} \exp(-\theta_f/T)$ $cm^3mole^{-1}s^{-1}$ or $cm^6mole^{-2}s^{-1}$

REACTION	BLIMP Kinetics			Park Kinetics			McKenzie Kinetics		
	C_f	η_f	θ_f	C_f	η_f	θ_f	C_f	η_f	θ_f
$O_2 + O \rightarrow 2\,O + O$	N/A	N/A	N/A	1.0e22	-1.5	59,750	9.05e18	-1.0	59,370
$O_2 + C \rightarrow 2\,O + C$				1.0e22	-1.5	59,750	9.05e18	-1.0	59,370
$O_2 + O_2 \rightarrow 2\,O + O_2$				2.0e21	-1.5	59,750	9.05e18	-1.0	59,370
$O_2 + CO \rightarrow 2\,O + CO$				2.0e21	-1.5	59,750	9.05e18	-1.0	59,370
$O_2 + CO_2 \rightarrow 2\,O + CO_2$				2.0e21	-1.5	59,750	9.05e18	-1.0	59,370
$CO_2 + O \rightarrow CO + O + O$	N/A	N/A	N/A	3.70e14	0.0	52,500	1.20e11	0.5	34,340
$CO_2 + C \rightarrow CO + O + C$				3.70e14	0.0	52,500	1.20e11	0.5	34,340
$CO_2 + O_2 \rightarrow CO + O + O_2$				3.70e14	0.0	52,500	1.20e11	0.5	34,340
$CO_2 + CO \rightarrow CO + O + CO$				3.70e14	0.0	52,500	1.20e11	0.5	34,340
$CO_2 + CO_2 \rightarrow CO + O + CO_2$				3.70e14	0.0	52,500	1.20e11	0.5	34,340
$CO + O \rightarrow C + O + O$	N/A	N/A	N/A	3.40e20	-1.0	129,000	4.48e19	-1.0	128,900
$CO + C \rightarrow C + O + C$				3.40e20	-1.0	129,000	4.48e19	-1.0	128,900
$CO + O_2 \rightarrow C + O + O_2$				2.30e19	-1.0	129,000	4.48e19	-1.0	128,900
$CO + CO \rightarrow C + O + CO$				4.48e19	-1.0	129,000	4.48e19	-1.0	128,900
$CO + CO_2 \rightarrow C + O + CO_2$				2.30e19	-1.0	129,000	4.48e19	-1.0	128,900
$CO_2 + O \rightarrow CO + O_2$	N/A	N/A	N/A	1.70e13	0.0	26,500	2.54e11	0.5	27,690
$CO + O \rightarrow C + O_2$	N/A	N/A	N/A	3.90e13	-0.18	69,200	2.73e12	0.5	69,540
$CO + CO \rightarrow CO_2 + C$	N/A	N/A	N/A	2.33e9	0.5	65,710	2.33e9	0.5	65,710

CO_2 Reactions (cont.)

Surface Reactions

REACTION	Fully Catalytic Wall	Noncatalytic Wall
$C + O \rightarrow CO$	1e6	1e-6
$CO + O \rightarrow CO_2$	1e6	1e-6
$O \rightarrow \frac{1}{2} O_2$	1e6	1e-6